Modelling the Hydrodynamic Drag Force of Flexible Riparian Woodland

Peter Whittaker

Hydro-environmental Research Centre

Cardiff University

A thesis submitted for the degree of

Doctor of Philosophy

March 2014

"We must never cease from exploration. And the end of all our exploration will be to arrive where we began and to know the place for the first time."

T. S. Eliot

Acknowledgements

I would like to thank Dr. C. Wilson and Prof. R.A. Falconer for their counselling and guidance as my supervisors. Additionally, this thesis would not have been possible without the generous funding from Forest Research and the assistance of H. Thomas in conducting field work. I am also grateful to my colleagues in the HRC for provoking stimulating discussion and providing many sanity preserving distractions. Finally, I would like to thank my family and Vaiva for all their support, encouragement and interest throughout my studies.

Declaration

This work has not been submitted in substance for any other degree or award at this or any other university or place of learning, nor is being submitted concurrently in candidature for any degree or other award.

Signed ..... Date .....

Statement 1

This thesis is being submitted in partial fulfilment of the requirements for the degree of PhD.

Signed ..... Date .....

Statement 2

This thesis is the result of my own independent work / investigation, except where otherwise stated. Other sources are acknowledged by explicit references. The views expressed are my own.

Signed ..... Date .....

Statement 3

I hereby give consent for my thesis, if accepted, to be available for photocopying and for inter-library loan, and for the title and summary to be made available to outside organisations.

Signed ..... Date .....

Statement 4

I hereby give consent for my thesis, if accepted, to be available for photocopying and for inter-library loans after expiry of a bar on access previously approved by the Academic Standards & Quality Committee.

Signed ..... Date .....

Abstract

In this thesis, two practical models for predicting the drag force exerted on flexible riparian vegetation under hydrodynamic loading have been developed. The models were formulated based on the results of a unique experimental data set that consisted of high resolution force-velocity and physical property measurements for twenty-one full-scale riparian trees, in both foliated and defoliated conditions. One of the models has then been used to numerically simulate the impact of riparian woodland on the flooding characteristics of a mid-catchment river site.

Analysis of photographs and video footage of the trees from the experimental study during drag force testing allowed the frontal projected area to be determined, both in still air and as a function of flow velocity. The observed reductions in projected area and drag coefficient with velocity were normalized using the projected area in still air to provide an empirical relationship between the 'rigid' drag coefficient and area Reynolds number. The resulting drag force predictions were found to be accurate when properly calibrated against the vegetation under consideration.

A second, more physically based model to predict the reconfiguration of flexible vegetation has been developed based on dimensional analysis of the relevant parameters, including flexural rigidity. The model utilizes a novel vegetative Cauchy number to determine the extent of the reconfiguration and has been shown to be more accurate than two existing drag force models. The model has also been validated against independent drag force data, demonstrating that it is applicable to vegetation of differing scale, morphology and flexibility.

Serial and parallel optimizations of an existing two-dimensional hydrodynamic modelling code have enabled detailed numerical simulations of extreme flood events to be undertaken for a mid-catchment river site in Somerset, UK. The results indicated that riparian vegetation has a minimal impact on the downstream flooding characteristics, at least for the small site investigated herein. Significant reductions in key flow properties, namely velocity and bed shear stress, were however observed within the vegetated areas.

Contents

List of Figures

List of Tables

List of Symbols

A_L	Total one-sided leaf area
A_L^{100}	One-sided area for 100 leaves
A_p	Projected area
A_{p0}	Projected area in still air
A_S	Total one-sided stem and branch area
C	Chezy roughness coefficient
C_d	Drag coefficient
C_d^*	Rigid drag coefficient
C_{d0}^*	Initial rigid drag coefficient
$C_{d\chi}$	Species-specific drag coefficient
Ca	Cauchy number
d_0	Basal stem diameter
d_{25}	First-quartile stem diameter
d_{50}	Mid-stem diameter
d_{75}	Third-quartile stem diameter
E	Modulus of elasticity
EI	Flexural rigidity

EI_{25}	First-quartile stem flexural rigidity
EI_{50}	Mid-stem flexural rigidity
f	Darcy-Weisbach friction factor
f'	Bed roughness factor
f''	Form factor
F	Total drag force
F_{defol}	Drag force due to stem and branches
F_{fol}	Drag force due to foliage
F_P	Pressure drag
F_S	Skin friction drag
g	Acceleration due to gravity
h	Bed elevation
H	Vegetation height
I	Second moment of area
k_s	Bed roughness height
M_d	Total dry mass
M_w	Total wet mass
$M_{L,d}$	Dry leaf mass
$M_{L,d}^{100}$	Dry mass of 100 leaves
$M_{L,w}$	Wet leaf mass
$M_{S,d}$	Dry stem and branch mass
$M_{S,w}$	Wet stem and branch mass

n	Manning friction coefficient
N	Number of trees per m^2
N_p	Number of computational processors
q	Discharge per unit width
Q	Flow rate
$\mathcal{R}$	Reconfiguration number
R^2	Coefficient of determination
R_h	Hydraulic radius
Re	Reynolds number
S	Slenderness ratio
U	Mean flow velocity
U_χ	Scaling velocity
V	Total volume
V_L	Leaf volume
V_S	Stem and branch volume
β	Momentum correction factor
$\epsilon_\%$	Average percentage error
ϕ	Latitude
η	Water surface elevation
μ	Dynamic viscosity
ν	Kinematic viscosity
ν_t	Kinematic eddy viscosity

ω	Angular frequency of Earth's rotation
ψ	Vogel exponent
ρ	Density
τ_b	Bed shear stress
χ	Power equivalent to the Vogel exponent
ζ	Water depth

Chapter 1

Introduction

1.1 Context and Perspective

Throughout history, people have settled along coasts and floodplains, attracted by the fertile soils, abundant water supplies and ease of transport. Today, a large percentage of the world's major towns and cities lie within these flood-prone areas and it is estimated that one sixth of the global population — over one billion people — live in the potential path of a 100-year flood (UNU-EHS 2004). With climate change forecast to increase the frequency of extreme weather events (Wetherald and Manabe 2002, IPCC 2007), this number is set to double by 2050.

In the UK alone, at least 6 million properties are currently at risk of flooding and the average annual cost of damage from flood water is estimated at more than £1 billion (EA 2009). The UK Climate Impacts Programme (UKCIP 2009) identified the following effects of climate change with respect to flood risk: winters will become wetter and summers may become drier; heavy winter rain and snow will become more frequent; relative sea level will continue to rise around most of the UK shoreline; and extreme sea levels will be experienced more frequently.

Combined, these factors will work to increase the frequency and severity of flooding within the UK (Reynard *et al.* 2004). Indeed, current flood defence planning allows for a 20% rise in peak river flows over the next 40 years (MAFF 2001) and a 1 m rise in mean sea level over the next 100 years (Defra 2006).

As a result, it is estimated that investment in flood defence assets will have to double by 2035 in order to maintain existing levels of protection (EA 2009). The continuation of research and innovation with respect to managing floods is thus required if the UK is to meet the challenges posed by climate change.

1.1.1 Flood Management

Floods are a part of nature and it is neither feasible nor economically affordable to prevent all damage from flooding. Policy makers have therefore shifted away from a reliance on engineered flood defences and have instead adopted a risk-based approach for flood management (ICE 2001). The IPCC (2012) report defines such risk management as:

> "Processes for designing, implementing, and evaluating strategies, policies, and measures to improve the understanding of disaster risk, foster disaster risk reduction and transfer, and promote continuous improvement in disaster preparedness, response, and recovery practices, with the explicit purpose of increasing human security, well-being, quality of life, resilience, and sustainable development."

The current methods and best practices in the UK for managing the risks associated with coastal and river flooding are thus explored here, within the context of the above definition. Other causes of flooding, such as failures in man-made infrastructure and rises in ground water levels, are not discussed due to their more localized nature.

Coastal Flooding

Coastal flooding occurs when sea levels exceed normal tidal ranges and any existing flood defences are overtopped. The causes of abnormal sea levels are typically split into two groups, namely: storm surges, which are a combination of naturally high 'spring' tides and increased sea level generated by areas of low pressure or high winds; and tsunamis, where large waves are created by the displacement of a significant volume of water after a earthquake, landslide or volcanic eruption.

Coastal flooding is generally best managed with 'hard' engineering schemes, such as concrete sea walls, barrages, and breakwaters. Natural habitats, such as mangrove forests and other wetlands, can also help to minimize flood risk and coastal erosion by attenuating the energy of storm and tsunami waves (Alongi 2008, Teo 2011). However, such ecological systems are usually found only in countries with tropical climates and are therefore not a viable solution in the UK.

River Flooding

The two key factors in river or fluvial flooding are: the volume of rainfall and the duration over which it occurs; and the capacity of the ground and rivers to absorb and transport the water. Perhaps the most damaging example of this in the UK occurred during the summer of 2007, when extreme levels of rainfall were compressed into a relatively short period of time. The extensive flooding that resulted in the north-east and west midlands (Fig. 1.1) is estimated to have cost £3.2 billion and was one of the worst floods globally in that year (ICE 2011).

Figure 1.1: Aerial photograph of Tewkesbury Abbey taken during the July 2007 flooding of the Avon and Severn rivers. Reproduced from Pitt (2008).

Although such extreme events are thankfully rare, the lessons learnt from the subsequent Pitt Review (Pitt 2008) regarding flood risk management are applicable across the country. The main findings of the report were broadly in

line with the Government's 2004 Foresight project (King 2004), which reviewed the long-term impact of climate change on the UK and concluded that there must be a shift from a reliance on 'over-designed' physical infrastructure, to a more holistic approach based on sustainable measures.

Typical 'hard' engineering solutions for minimizing fluvial flood risk include: levees and flood walls; reservoirs to store water for release at safer flow rates; channel diversions to route flood waters around areas needing protection; and increasing the size and number of culverts through floodplain embankments. However, it is neither cost-effective nor practical to build such flood defences everywhere. Moreover, these projects, with the exception of reservoirs, can potentially exacerbate flooding further downstream as they simply displace the problem along the reach, rather than addressing the source of the issue.

In contrast, it is possible to reduce overall flow rates, and thus mitigate the risk of fluvial flooding, by employing 'soft' engineering approaches. These more sustainable options include: the reforestation and re-vegetation of floodplains in order to drastically increase infiltration and reduce run-off (Marshall *et al.* 2014); reintroducing meanders to rural river channels to slow flow rates and promote flooding in non-critical areas (CRT 2014); and encouraging large woody debris dams to form at regular intervals in order to create additional flood storage, as demonstrated by the Defra funded 'Slowing the flow at Pickering' project in North Yorkshire, UK (Nisbet *et al.* 2011).

1.1.2 Riparian Woodland

Aside from the benefits to fluvial flood risk reduction, riparian woodland plays an important role in the ecological, commercial, and recreational management of floodplains. However, due to commercial pressures and misguided river management activities, floodplain forests are now considered a threatened habitat in many European countries (UNEP 2000, Hughes 2003). In order to combat this, there has been a resurgence in the conservation and restoration of riparian woodland in recent years (UN 2006).

Ecological Benefits

In many river systems, forests form the natural vegetation inhabiting the floodplain zones, with the range of plant species at a given location being influenced by the position within the river basin (Tabacchi *et al.* 1996). The forests support a large amount of the surrounding wildlife and fauna in numerous ways. For example, the woodland canopy creates shade that inhibits weed growth and helps to reduce extremes of water temperature that can be damaging to freshwater life (Broadmeadow *et al.* 2011). Additionally, the roots of trees and other vegetation bind and strengthen soils and stream banks, thus reducing erosion and sedimentation (Thorne *et al.* 2010). The roots can also filter agricultural nutrients and other pollutants from run-off before it reaches the main watercourse (SEPA 2009).

Commercial Benefits

Riparian woodland can also be designed to not only improve stream habitat and water quality, but to provide commercial opportunities to landowners. The conditions along river floodplains are usually particularly amenable to tree species, such as poplar and willow, that can be regularly harvested or coppiced (Fuller and Warren 1993, Starr 2013). This process is known as short rotation coppicing (SRC) and the wood is grown as an energy crop, with the biomass typically being used for heating or electricity generation. It is anticipated that biomass and SRC will play a key part in reaching the UK Government's target for 15% of energy consumption in 2020 to be from renewable sources (McKay 2011).

Recreational Benefits

Finally, there are many indirect benefits to introducing or restoring woodland to the riparian zone. For example, the diversity of habitats within these areas offer recreation for fishers, bird watchers, hikers and canoeists. In addition, it can increase the value of local residential property (Mansfield *et al.* 2005)

1.2 Motivation

With the shift to sustainable flood risk management and the increasing awareness of the benefits of riparian woodland, it is imperative that the impact of such vegetation on the flood characteristics of natural river systems is understood. This is of particular importance when using numerical models to assess the flood risk of a particular catchment where lives and property may be affected by inaccurate predictions. However, as will be explored briefly here and in detail in section (§ 2.3), current widely-adopted methods for the treatment of vegetative flow resistance in numerical modelling can be improved.

1.2.1 Current Practices and Limitations

The definition for riparian woodland covers a relatively broad range of habitats and species, including mature natural woodland, restoration woodland planted at a specific density and pattern, and short rotation coppice used as energy crops. For flood flows through such regions the flow-vegetation interactions are numerous and complex. As a result, typical modelling approaches have relied on abstracting the vegetation as an increase to the surface roughness. The most widely utilized of the roughness coefficients are Manning's n and the Darcy-Weisbach friction factor f.

While this approach is trivial to implement and requires no extra parameters, it can require significant calibration to obtain a value that provides a reasonable approximation. In addition, calibration is typically only performed with respect to the water elevation or inundation extent as velocity measurements are rarely available on the floodplain, and therefore localized flow phenomenon may not be accurately recreated. Furthermore, Manning's n values are dependent on the flow depth and constant values for n and f do not take into account the flexibility or heterogeneity of natural vegetation.

An alternative approach is to directly model the drag force exerted on the vegetation by the flood flows. For vegetation which can be assumed to be rigid and cylindrical, such as mangroves, the relationship between the flow velocity and the drag force follows a well-known relationship, with only a standard drag coefficient and the diameter of the vegetation required as inputs. However, natural vegetation

is often flexible (compared to the hydrodynamic force exerted) and variable in morphology and therefore cannot be approximated as rigid or cylindrical.

As a consequence, recent research has focused on parameterizing the drag force in terms of the vegetation's measurable physical properties. However, while drag force experiments involving rigid cylinders are numerous, those involving full-scale trees are much rarer due to the size constraints of most experimental facilities. The paucity of data sets means that there is still considerable uncertainty over which physical properties may be most useful in parameterizing the drag force exerted on trees within riparian woodland regions.

1.3 Thesis Scope and Objectives

The main aims of this thesis can be identified as:

1. Analyse photographs and video footage of full-scale trees from a large experimental drag force study in order to assess how the trees bend and deform in response to hydrodynamic loading and how this affects their hydraulic resistance.

2. Formulate practical and physically-based models for predicting *a priori* the hydrodynamic resistance of flexible riparian vegetation, namely trees and saplings. The models will be developed from sound theoretical reasoning so that they may be applicable to as wide a range of flow conditions as possible, without the need for time-consuming calibration.

3. Optimize an existing numerical modelling software code to take advantages of advances in heterogeneous computing so that flood risk mapping can be carried out over large reaches in a manageable time frame.

4. Utilize the new hydrodynamic resistance models to asses the potential impact of riparian woodland on typical and extreme fluvial flood events at a case study site in Somerset, UK. This will be investigated through a range of different floodplain arrangements, including no vegetation, native riparian woodland, energy crops, and floodplain storage.

This research is necessary to further extend existing knowledge and assist policy-makers in making key decisions regarding land use and flood risk management.

1.3.1 Thesis Layout

Given the aims and objectives outlined above, this thesis is split into two main sections: experimental data analysis and model development; and numerical modelling of the flooding processes at a riparian case study site. Synopses for each of the chapters in this thesis are provided in the following paragraphs.

An overview of the current literature with respect to the aero- and hydrodynamic modelling of trees and other vegetation is given in the second chapter (§ 2). The topics explored include: a general background to aero- and hydrodynamic drag force; existing models for predicting the drag force of rigid and flexible vegetation under emergent and submerged flow conditions; and previous numerical modelling studies involving vegetated flows.

The third chapter (§ 3) begins the first of the two main themes and introduces the two experimental data sets used in this thesis: the first consists of high-resolution drag force and physical property measurements for a large number of foliated and defoliated full-scale trees; the second is independent and contains similar measurements for partially and fully submerged tree branches.

After investigating the impact of foliage on the trees' drag characteristics and quantifying the specimens' reconfiguration, photos and videos of the trees in still air and during drag force testing are analysed using sophisticated image processing techniques. This enables the variation in the trees' projected areas, and thus drag coefficients, with flow velocity to be determined and discussed, providing insight into the deformation of flexible vegetation under hydrodynamic loading.

In the fourth chapter (§ 4), two drag force models are proposed: the first is empirical and uses the vegetation's projected area in still air and a modified Reynolds number to predict the variation in drag coefficient with flow velocity; the second is developed from dimensional consideration and strong emphasis is placed on accurately representing the deformation of the trees by considering

their flexural rigidity via the Cauchy number. Both models are applied to the experimental tree and branch data from the previous chapter and compared to existing drag force approaches. A parameter sensitivity analysis is also carried out for the second model.

The fifth chapter (§ 5) contains the research relevant to the second of the two main themes in this thesis. It begins by revising the underlying equations of motion for a fluid and the numerical scheme chosen to solve those equations. The Cauchy drag force model from the previous chapter is then inserted into an existing computational fluid dynamics code. General optimizations, both serial and parallel, are performed and the code is refactored to enable it to take advantage of recent advances in heterogeneous computing.

The case study site is then introduced and the numerical model set up and subsequently calibrated against flow gauging data. To assess the impact of riparian woodland on the flood characteristics of the site, a number of different scenarios are modelled, including: removing all woodland from the floodplains; utilizing the existing riparian woodland; replacing the existing woodland with short rotation coppice plantations; expanding the short rotation coppices to cover the full extent of the floodplains; and mixing woodland and floodplain storage by introducing earthen bunds at the downstream boundary.

Finally, a summary of the main findings in this thesis and suggested areas for future research are presented in the final chapter (§ 6).

Chapter 2

Literature Review

2.1 Introduction

In this chapter, the current state-of-the-art with respect to the aero- and hydro-dynamic modelling of trees and other vegetation is reviewed. Firstly, an overview of the theory behind the drag force exerted on objects subject to a fluid flow is given. An introduction into the existing techniques most commonly used for predicting the hydraulic resistance of rigid or idealized vegetation is then provided. The merits and limitations of such methods when applied to modelling flexible vegetation are then discussed, with more suitable approaches presented from the literature. Examples of previous numerical modelling studies involving vegetated flows are also included and assessed. Finally, the gaps in existing knowledge with respect to the accurate treatment of flexible vegetation in aero- and hydro-dynamic flows are highlighted.

2.2 Drag Force Theory

When there is relative motion between a fluid and an immersed body, the fluid will exert a force on that object. For flows over a plane surface parallel to the direction of the free stream, such as a thin flat plate, the force is due to the shear stress caused by the viscous interaction between the fluid and the surface. This is usually known as the skin friction drag. In the case where the surface of the

body is not completely parallel to the direction of the flow, there is an additional drag force arising from changes in pressure over the surface. This is termed the pressure drag. It is also referred to as the form drag since the magnitude of the force is dependent on the shape of the object. The total drag F, often termed the profile drag, is therefore the sum of these two forces:

$$F = F_S + F_P \tag{2.1}$$

where F_S is the drag due to skin friction and F_P is the drag due to pressure.

The relative proportion of friction and pressure drag that accounts for the total drag is dependent on the shape of the object and its orientation in the fluid stream. For example, a thin flat plate held parallel to the flow, as shown in Fig. 2.1a, will experience a drag force that is almost entirely due to skin friction. On the other hand, if the same plate is rotated so that its surface is perpendicular to the flow, as shown in Fig. 2.1b, the skin friction will become negligible and the pressure drag will dominate.

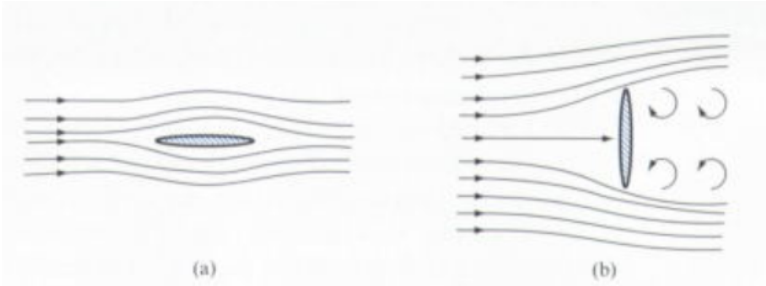

Figure 2.1: Streamlines for: (a) streamlined object; (b) bluff object. Reproduced from Douglas *et al.* (2005, pp. 398).

Although F_S and F_P in Eq. (2.1) can be determined analytically by integrating around the surface of the body, this requires detailed knowledge of the distribution of pressure and shear stress around the object. Therefore, in practice the total drag force F is usually determined experimentally and is related to certain parameters via the following expression:

$$F = \frac{1}{2}\rho C_d A u^2 \tag{2.2}$$

where ρ is the density of the fluid; C_d is the dimensionless drag coefficient; A is the reference area of the body; and u is the reference velocity.

In experiments with cylinders and investigations into plant drag, the reference area is usually taken as the projected area A_p of the body perpendicular to the flow, while the reference velocity corresponds to the free stream velocity, typically denoted as u_m or U. It can be seen that for cases where the reference area and drag coefficient are constant, such as a bluff inflexible body in a flow of relatively constant Reynolds number, the drag force follows a quadratic relationship with velocity.

2.2.1 Drag Coefficient

The equation used to determine the total drag (Eq. 2.2) is based on an idealized situation where the fluid comes to a complete stop over the projected area of the body and the force on the rigid or bluff object is completely due to stagnation pressure over the whole front area. Since no real object exactly corresponds to this behaviour, a drag coefficient C_d is introduced. This drag coefficient is the ratio of drag for any real object to that of the ideal object and incorporates the effects of both skin friction and pressure drag. For instance, the ideal plate shown in Fig. 2.2a would have a drag coefficient of 1, while the actual plate, depicted in Fig. 2.2b, experiences additional drag due to a suction pressure on the rear face as the fluid flows around it and subsequently has a higher drag coefficient of around 1.15 (Shames 2003).

(a) Ideal (b) Actual

Figure 2.2: Stagnation pressure for flow around: (a) an idealized plate; (b) a real plate.

The value of the drag coefficient for a particular object is determined experimentally using Eq. (2.2):

$$C_d = \frac{F}{\frac{1}{2}\rho A_p U^2} \tag{2.3}$$

Since the drag coefficient is the ratio of two forces, it is the same for two dynamically similar flows and is, therefore, independent of the size of the object (although not of its shape) and is a function of the Reynolds number Re. Fig. 2.3 illustrates how the value of the drag coefficient varies with the Reynolds number for a selection of two-dimensional bodies; the thick line represents an infinitely long, smooth circular cylinder held with its long axis perpendicular to the flow.

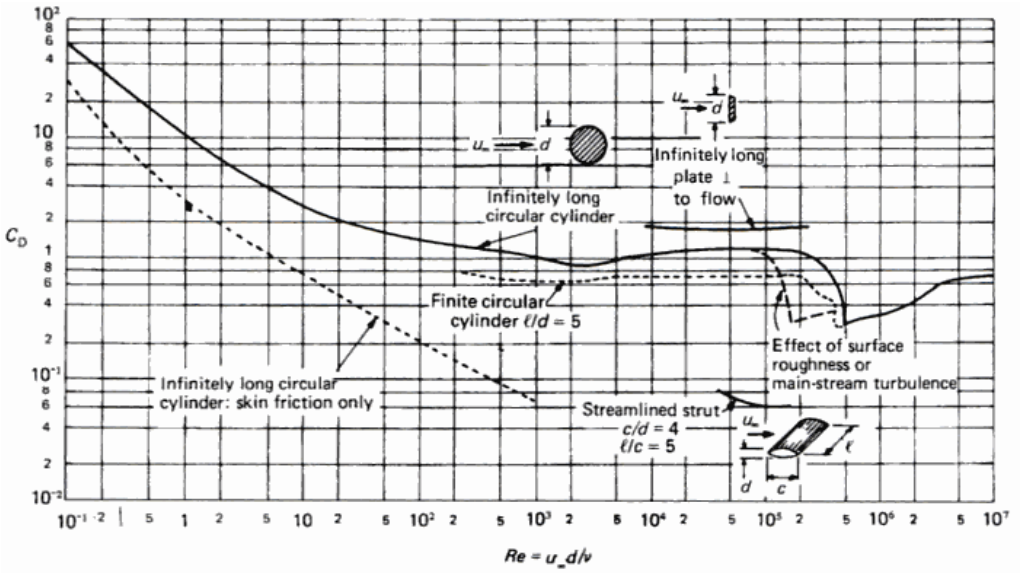

Figure 2.3: Variation in drag coefficient with Reynolds number for two-dimensional objects. Reproduced from Massey (2006, pp. 330).

2.3 Vegetative Drag and Resistance

The most widely utilized approach for representing the hydraulic effect of vegetation has been through the use of friction coefficients such as Manning's n or Darcy-Weisbach's f. These combine multiple roughness effects, such as bed friction, vegetative drag, effects of channel cross-section, etc., into a single term

by utilizing the superposition principle (e.g. Cowan 1956, Petryk and Bosmajian 1975, Yen 2002). Recent studies, however, have criticized the use of the dimensional Manning's n coefficient (Ferguson 2010) and instead favoured the use of the dimensionless Darcy-Weisbach friction factor f (e.g. Järvelä 2002a, Fathi-Moghadam 2007).

Focusing on flow situations where only bed friction and vegetative drag are of significance, the total friction factor can be decomposed into a bed roughness factor f' and a form resistance factor f'' according to the linear superposition principle, i.e. $f = f' + f''$. In investigations with rigid vegetation and cylinders (e.g. Li and Shen 1973, Huthoff *et al.* 2007), the form factor f'' is related to the spatially-averaged drag force $\langle F \rangle$ via:

$$f'' = \frac{8\langle F \rangle}{s_x s_y \rho U^2} \tag{2.4}$$

where s_x and s_y are the longitudinal and lateral spacing of the roughness elements; ρ is the density of the fluid; and U is the reference velocity, typically taken as the free stream velocity.

2.3.1 Idealized Vegetation

In order to calculate the spatially-averaged drag force, the drag force on a single element must be known. In the case of rigid cylinders and other idealized vegetation, the classical drag force equation (Eq. 2.2) can be employed without modification. There have been numerous tests on isolated cylinders and other standard objects, and the variation in drag coefficient C_d with flow Reynolds number Re is well documented for such cases (see Fig. 2.3). At higher Reynolds numbers, the drag coefficient is essentially constant and Eq. (2.2) describes a quadratic relationship between drag force and velocity. Indeed, this quadratic drag force relationship has been found to be applicable for artificially stiffened vegetation (Armanini *et al.* 2005, Aberle and Dittrich 2012).

Although the variation in drag coefficient with Reynolds number for isolated cylinders is well understood, the flow pattern around multiple cylinders quickly becomes very difficult to predict as the number of elements increases. As such, research into the flow resistance of idealized vegetation has primarily been fo-

cused on the bulk drag coefficient C_D of arrays of cylinders (e.g. Lindner 1982, Wu *et al.* 1999, Stone and Shen 2002, Tang *et al.* 2012).

An important experimental study undertaken by Nepf (1999) investigated the link between the bulk drag coefficient and the density of emergent cylinder arrays. Both random and staggered arrays of rigid cylinders were tested under uniform flow conditions in a 24 m long by 38 cm wide flume. Data was also collated from a number of similar previous studies. It was found that the bulk drag coefficient decreased both with increasing array density, due to wake interference, and with increasing stem Reynolds number. A model was also proposed that described the interdependence of drag, turbulence and diffusion within arrays of emergent rigid vegetation. The model was validated against experimental data with array densities ranging from 0.01% to 0.5% and with stem Reynolds numbers up to 1×10^5.

Recent studies have also found a similar trend, with the bulk drag coefficient tending to decrease with increasing stem Reynolds number (Ishikawa *et al.* 2000, Tanino and Nepf 2008, Kothyari *et al.* 2009). However, there appears to be some contradiction with regards to the relationship between the bulk drag coefficient and the density of the cylinder array. For example, a study performed by Tanino and Nepf (2008) found that the bulk drag coefficient increased with increasing array density, rather than decreased, for arrays of randomly distributed cylinders. The experiments were carried out under steady, non-uniform flow conditions with the arrays having solid volume fractions of 0.1 to 0.35 and with stem Reynolds numbers ranging from 25 to 685.

Although the experimental conditions in Tanino and Nepf (2008) were somewhat different to those in Nepf (1999), the results from recent studies (e.g. Ishikawa *et al.* 2000, Kothyari *et al.* 2009, Stoesser *et al.* 2010) agree that the bulk drag coefficient tends to increase with increasing array density, even for similar experimental conditions. Aberle and Järvelä (2013) postulated that the contradictory findings may be a result of experimental differences, such as the establishment of quasi- or non-uniform flow, the manner in which the drag force is measured (i.e. direct drag force sensors or indirectly through velocity measurements), and neglecting the effect of wake interference on the spatial variability of the drag force within the array.

2.3.2 Flexible Vegetation

When modelling flexible or non-cylindrical vegetation, a common compromise is to idealize the vegetation into rigid cylinders, as discussed above. The plant or tree is then assigned an equivalent diameter and a value for the drag coefficient is taken from the literature. For example, one of the earliest experimental studies investigating the drag force response of flexible vegetation was carried out by Hirata (1951) who used small live cuttings of plants in a wind tunnel to estimate drag coefficients for full-scale vegetation.

Additionally, Mayhead (1973) analysed data previously collected from wind tunnel experiments in 1962 and 1967, in which mature conifers (from 6 m to 8 m in height) were tested over wind velocities ranging from 9.1 $\mathrm{m\,s^{-1}}$ to 38.3 $\mathrm{m\,s^{-1}}$. The projected area of each tree in still air was determined both photographically and also from an estimate based on the length and diameter of the crown. Using the measured drag force and the projected area of the tree in still air, Mayhead was able to recommend drag coefficients for use in wind force uprooting predictions.

In a study of the damage caused to trees and forests due to wind loading, Papesch (1977) measured the drag force and bending moment of natural trees positioned on the outer edges of two separate forests. The projected area in still air was determined through photographic analysis and was assumed to stay constant with increasing wind speed so that the variation in drag coefficient with wind velocity could be calculated for each tree.

Reconfiguration

Using an idealized approach, where an initial value for the projected area and a simple relationship for the drag coefficient are utilized, ensures that the resulting calculations are trivial to perform; however, the modelled drag force is often much higher than would be expected. This is because such models do not take into account any changes to the vegetations' structure, and thus projected area, that can occur with increasing velocity (Vogel 1984). It is claimed that this 'reconfiguration' is an essential mechanism employed by vegetation in order to reduce the stress induced by an external flow (Harder *et al.* 2004, Nikora 2010).

Indeed, many studies investigating the drag force exerted on flexible vege-

tation have found that this reconfiguration causes the measured force-velocity relationship to deviate away from a quadratic response, even at high Reynolds numbers. For example, Fathi-Maghadam and Kouwen (1997) placed saplings of pine and cedar in an open channel flume and recorded the effect of reconfiguration on the drag coefficient and the momentum absorbing area at different flow depths and velocities. Using dimensional analysis and the experimental results, the authors devised a functional relationship between the physical parameters (plant density and flexural stiffness) and the flow conditions (depth and velocity). However, while the model provided relatively accurate predictions for the friction factor, it has not been widely adopted, perhaps due to the practical difficulty in quantifying the spatial distribution of the vegetation's momentum absorbing area.

The non-quadratic force-velocity relationship for flexible vegetation has also been observed in numerous similar studies (e.g. Oplatka 1998, Freeman *et al.* 2000, Järvelä 2004, Sand-Jensen 2008, Wilson *et al.* 2008, Schoneboom 2011, Siniscalchi and Nikora 2013). Some researchers have suggested that the force-velocity relationship for flexible vegetation may, in fact, be characterized as linear at certain velocities (Vischer and Oplatka 1998, Sand-Jensen 2003, Armanini *et al.* 2005, Cullen 2005, Xavier 2009). However, where authors have proposed models for predicting the drag force of flexible vegetation, they have typically been based on empirical approaches and it is therefore unclear whether they would be applicable to vegetation of differing morphology or scale.

For example, the reconfiguration and hydrodynamic drag of flexible macroalgae was investigated by Boller and Carrington (2006). The drag force, projected area, and shape of *Chondrus crispus* specimens were recorded in a flume for velocities up to 2 m s^{-1}. The change in a specimen's projected area with increasing velocity was found to contribute more to the reduction of the drag force than the change in the drag coefficient. A empirical model for the drag force was developed which assumed that the reduction in projected area and drag coefficient followed an exponential decay. The exponential relationship was chosen by the authors as it was claimed to give the best correlation. However, while the drag force predicted by the model was closer to the measured force than the classical drag equation, there was still significant deviation from the measured force for the majority of specimens.

Vogel Exponent

The extent to which the vegetation reconfigures and the drag force deviates from the squared velocity relationship (Eq. 2.2), has often been expressed in terms of a Vogel exponent ψ. The idea was first introduced by Vogel (1984) and later studied by, for example, Gaylord *et al.* (1994), O'Hare *et al.* (2007), and Gosselin and de Langre (2011). The Vogel exponent was originally devised in order to investigate the drag force response of vegetation in regions of large deformation, i.e. above a certain threshold velocity.

In general terms and not considering the dependency of C_d on Re, the Vogel exponent modifies the power to which the velocity is raised in the classical drag formula, so that:

$$F \propto U^{2+\psi} \tag{2.5}$$

with most reported values of ψ ranging between -0.2 and -1.2 (de Langre *et al.* 2012).

For a rigid object or plant $\psi = 0$ and Eq. (2.5) returns to a classical squared relation, while a value of $\psi = -1$ would indicate a linear force-velocity relationship. Alben *et al.* (2002) and de Langre (2008) showed that for flexible fibres, scaling predicts an exponent of $\psi = -2/3$, with similar values reported for individual leaves (Albayrak *et al.* 2012). The dependence of the Vogel exponent on the flexural rigidity of the object was highlighted by Oplatka (1998), who tested full-scale trees in a flume and found that for a fully stiff tree $\psi = 0$, for a partially stiffened tree $\psi = -0.36$ and for a fully flexible tree $\psi = -1$.

The Vogel exponent concept is also represented in the work of Järvelä (2004), who proposed that the form resistance factor f'' for just submerged vegetation is dependent on the leaf area index (LAI) and certain species-specific parameters:

$$f'' = 4C_{d\chi} LAI \left(\frac{U}{U_\chi}\right)^{\chi} \tag{2.6}$$

where $C_{d\chi}$ is a species-specific drag coefficient; χ is also unique to a particular species and accounts for the reconfiguration of flexible vegetation; and U_χ is a scaling value included to ensure dimensional homogeneity, equal to the lowest velocity used in determining χ.

Under the assumption that the LAI varies linearly with vegetation height, Eq. (2.6) can be extended to emergent vegetation by scaling the LAI term by the relative depth (i.e. $H/\zeta \leq 1$ where H is the vegetation height and ζ is the water depth). It can also be found from rearranging Eqs. (2.4) and (2.6) that the χ value is equivalent to the Vogel exponent, i.e. $F \propto U^{2+\chi}$ (Aberle and Järvelä 2013).

The use of Eq. (2.6) has been prevalent in a number of recent studies. For example, Dittrich *et al.* (2012) measured the spatially-averaged drag force for arrays of submerged artificial plants in a 32 m long, 0.6 m wide and 0.4 m deep flume for velocities up to 0.8 m s^{-1}. The authors found that Eq. (2.6) accurately described the variation in f'' when using χ values of -0.74 for the staggered arrays and -0.73 for the in-line arrays.

The impact of varying the LAI was investigated by Jalonen *et al.* (2013), where the spacing and vertical leaf distribution of arrays of artificial plants were systematically modified. The spatially-averaged drag forces were recorded for just-submerged conditions and the velocities ranged from 0.11 m s^{-1} to 0.92 m s^{-1}. The experiments were carried out in the same flume as described in Dittrich *et al.* (2012). The authors varied the LAI between 0.2 and 3.2 and found that the f'' could be described using a relatively constant value of $\chi \approx -0.9$, thus suggesting that the χ parameter is indeed species-specific.

Flexural Rigidity

While the studies listed above have shown that Eq. (2.6) may be a useful model for predicting the flow resistance of leafy vegetation, it remains to be seen whether the approach can be applied to defoliated vegetation since in such cases the LAI will be equal to zero. Additionally, Eq. (2.6) relies on an empirical scaling factor U_χ that must be determined experimentally and is not based on physical reasoning. Furthermore, such models do not explicitly include the vegetation's flexural rigidity, but rather incorporate it into the Vogel exponent.

As a result, it is difficult to accurately predict the Vogel exponent (or χ value) *a priori*. Therefore, various studies have sought to decouple the flexural rigidity from the Vogel exponent by including it explicitly in the proposed drag force model. This is typically achieved via the addition of a dimensionless 'vegetative'

Cauchy number, as discussed by de Langre (2008):

$$Ca = \frac{\rho U^2 S^3}{E} \tag{2.7}$$

where ρ is the density of the fluid; U is the flow velocity; S is a 'slenderness' number, defined as the ratio of the minimum to maximum cross-sectional dimensions; and E is the modulus of elasticity.

One of the first studies to parameterize the relationship between reconfiguration and flexural rigidity in such a manner was undertaken by Gosselin *et al.* (2010), where the drag force for two simple geometries of flexible plates under aerodynamic loading was recorded. The authors performed a dimensional analysis and found that the force-velocity measurements collapsed onto a single curve when relating the magnitude of the reconfiguration to the scaled Cauchy number. In regions of large deformation the models accurately predicted that the flexible rectangular plate would have a Vogel exponent of $\psi = -2/3$ and that the flexible circular disk would have an exponent of $\psi = -4/3$.

This work was extended by Gosselin and de Langre (2011), who measured the drag force exerted on rigid and flexible poroelastic systems in a wind tunnel. A similar dimensional analysis was performed and the force-velocity measurements were observed to collapse onto a single curve when the reconfiguration was related to the Cauchy number and the surface density. The authors found that as the surface density increased, the Vogel exponent in regions of large deformation transitioned from $\psi = -2/3$ to a relatively constant value of $\psi = -1$.

The Cauchy number approach was applied to real, albeit simplified, aquatic vegetation by Luhar and Nepf (2011), where it was defined as:

$$Ca = \frac{\rho C_D U^2 l^3 b}{2EI} \tag{2.8}$$

where l and b were the length and breadth of the idealized beam, respectively.

Although the model, in conjunction with a buoyancy term, accurately predicted the reconfiguration and drag force of the specimens considered, it is unclear whether the definition of the Cauchy number would be applicable to full-scale vegetation, such as trees and other riparian vegetation, since it was based on an idealized slender beam.

In order to model the drag force exerted on vegetation with more complex morphology, Whittaker *et al.* (2013) replaced the length and breadth terms in Eq. (2.8) by the vegetation's volume and height. The redefined Cauchy number was then incorporated into the classical drag equation (Eq. 2.2) via dimensional analysis to produce the following drag force model:

$$F = \frac{1}{2}\rho K \left(U\sqrt{\frac{\rho V H}{EI}} \right)^{\psi} U^2 \tag{2.9}$$

where K corresponds to an initial $C_d A_p$ value; V, H, and EI are the vegetation's volume, height and flexural rigidity, respectively; ψ is a species-specific Vogel exponent; and the terms within the parentheses represent the vegetative Cauchy number.

The model (Eq. 2.9) was able to predict the drag force exerted on submerged full-scale riparian woodland trees (in both foliated and defoliated states) with fairly good accuracy once species-specific values for the Vogel exponent ψ and linear relationships between K and the tree's volume were determined. However, limited data availability meant that the model was unable to be validated against an independent data set so it remains to be seen whether such a model would be applicable to vegetation of a different scale or relative level of submergence.

Table 2.1 provides a summary of the drag force models currently available for flexible vegetation and their required parameters.

Table 2.1: Summary of the currently available models for predicting the drag force exerted on flexible vegetation.

Model	Coefficients	Physical Properties	Notes
Kouwen and Fathi-Moghadam (2000)	α, β	m, E	Applicable for non-submerged and foliated vegetation only
Järvelä (2004)	$C_{d\chi}$, U_χ, χ	LAI, H	Scaling velocity U_χ may not be theoretically correct
Xavier (2009)	C_d, U_t, ψ	A_p	Assumes that drag force is linear above U_t threshold velocity
Whittaker *et al.* (2013)	K, ψ	H, V	Replaces $C_d A_p$ term with K, which is determined via a linear relationship with volume

2.3.3 Numerical Modelling Studies

Accompanying the experimental research detailed above, there have been numerous numerical modelling studies that have investigated the impact of vegetation on key flow properties. These studies can typically be split into two categories based on the scales at which the models operate, namely: the stem scale, where the interactions between the flow and vegetation at the individual plant level are modelled (Fig. 2.4a); and the reach scale, where only the overall impact of vegetation on flow resistance is taken into account (Fig. 2.4b).

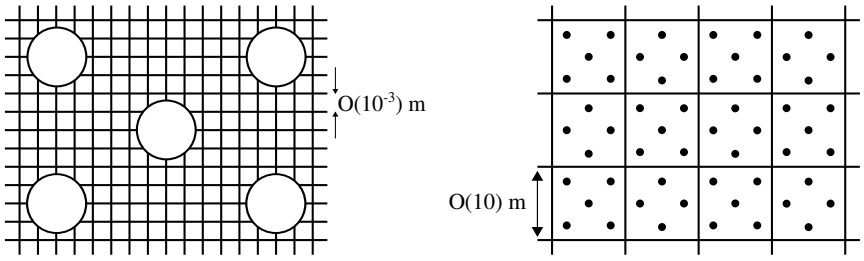

(a) Stem-scale grid (b) Reach-scale grid

Figure 2.4: Comparison of finite difference grid resolutions for: (a) stem-scale; and (b) reach-scale models. Individual plants or stems are represented as circles.

Stem-scale Modelling

In order to investigate local properties of the flow, such as turbulence and wake effects, the vegetation elements must be significantly larger than the individual grid cells used to discretize the flow field (Fig. 2.4a). To model these complex phenomenon, three-dimensional (3D) large eddy simulations (LES) are often employed to solve the governing equations (see § 5.2).

For example, Stoesser *et al.* (2009) utilized LES to model the flow through submerged vegetation, as represented by idealized rigid cylinders. The authors compared the results to those recorded by an experimental study of the same set-up (Liu *et al.* 2008) and found that the model accurately predicted the flow velocities and turbulence intensities. The model also correctly represented larger-scale flow structures, such as horseshoe and von Kármán vortices.

This approach was extended by Stoesser *et al.* (2010), who used high-resolution LES to investigate the flow through different densities of emergent rigid cylinders. Again, there was found to be good agreement for the velocities and turbulence intensities between the model and the experimental measurements (Liu *et al.* 2008). More importantly, however, the high-resolution of the simulations allowed the authors to explicitly calculate the pressure and skin friction drag forces acting on the cylinders, without the need for empirical relationships. The findings suggest that flow resistance due to rigid vegetation increases with both planting density and stem Reynolds number.

Although the previous study showed that high-resolution LES can provide accurate predictions for the flow around rigid vegetation with minimal calibration, the computational cost is prohibitive. Therefore, Kim and Stoesser (2011) investigated two, more computationally efficient, approaches. The first method incorporated the drag force as a sink term in the Reynolds-averaged Navier-Stokes (RANS) momentum equations (see Eq. 5.1a), while the second utilized LES with a low-resolution grid (20 times coarser than that used by Stoesser *et al.* 2010).

The results from both models were compared to the experimental data of Tanino and Nepf (2008) and also the results from the high-resolution LES study of Stoesser *et al.* (2010). The authors found that both models were able to accurately predict the observed velocities and turbulence intensities. However, the RANS model required careful calibration of the empirical drag coefficient, especially at higher vegetation densities. The authors also provided a summary of previous rigid cylinder modelling studies, along with the values that were used for the drag coefficient and any modifications that were made to the turbulence closure schemes.

Further study of the flow around vegetation at the stem-scale was carried out by Huai *et al.* (2011), who used 3D LES to model emergent rigid cylinders in super- and sub-critical flows. The velocity profiles from the model were corroborated by experimental data and the authors found that the drag coefficient for the vegetation decreased with increasing Froude number.

In addition, Mattis *et al.* (2012) investigated the relationship of the drag coefficient with respect to the stem Reynolds number for flows through densely vegetated wetlands (idealized as rigid cylinders). This was achieved by modelling the

flow using high-resolution LES. At lower Reynolds numbers, the well-established Darcy's Law was found to be applicable, while at higher Reynolds numbers two relationships were proposed: a modified Darcy-Forchheimer equation and a power law both provided reasonable approximations for the drag coefficient.

Reach-scale Modelling

While the stem-scale models are capable of directly determining the drag on idealized vegetation without the need for empirical relationships, they are not easily applied to flexible vegetation and are too computationally expensive to run over the reach scale, as required for effective flood risk management analysis. Therefore, modelling vegetation at the reach scale has typically relied on bulk friction coefficients, such as Manning's n, Chezy's C or the Darcy-Weisbach factor f. However, the range of possible values for these coefficients is large (e.g. Chow 1973, Arcement and Schneider 1989) and choosing a correct value for vegetated regions requires considerable experience and calibration.

To overcome these limitations, the drag force is often included directly into the momentum equations that govern fluid flow (see § 5.2). This approach reduces calibration uncertainties and offers a more physically-based model for incorporating vegetation resistance than the traditional use of a bulk friction coefficient. For example, Fischer-Antze *et al.* (2001) modelled a number of partially vegetated channels with the addition of a drag force term and a k-ϵ turbulence model. Although the vegetation was idealized as rigid cylinders, the resulting velocity profiles were in good agreement with the experimental measurements.

Stoesser *et al.* (2003) used the method validated by the experimental studies of Fischer-Antze *et al.* (2001) and Lopez and Garcia (2001) to model a 100 year flood event on a 3.5 km stretch of the River Rhine, Germany. The river floodplains contained a mix of riparian woodland which were idealized as arrays of rigid cylinders. Good agreement in the mean flow velocities on the floodplains was found between the measured values and the results of the 3D modelling. It should be noted that the k-ϵ turbulence closure model utilized in the study was not modified to take into account the presence of vegetation since the drag force term

was previously found to be dominant over the diffusive turbulent terms within emergent and submerged vegetation (Fischer-Antze *et al.* 2001, Stoesser 2002).

The hydraulic resistance of two species of willow trees (*Salix alba* and *Salix fragilis*) was also investigated for a compound channel over a test reach of 170 m by Wilson *et al.* (2006b). The authors directly included the drag force in the momentum equations and varied the parameterization of the trees' projected areas using uniform and non-uniform equivalent cylinder diameters and an empirical relationship with plant height. 3D modelling showed that the uniform parameterization resulted in relatively greater velocities in the region close to the bed and lower velocities in the upper region, compared to the non-uniform parameterization. This was particularly evident in the impact on bed shear stresses, where there was a 150% relative difference between the two approaches.

This work was further extended by Wilson *et al.* (2006a), who included the effects of reconfiguration via a simple angle of deflection model. The study demonstrated the need to include reconfiguration in drag force models and accurately predicted velocity profiles for a flood event in the same compound channel as the previous study. However, the reconfiguration model was not based on the physical processes and did not included key biomechanical properties, such as flexural rigidity.

More recently, Wang and Wang (2011) evaluated the effect of submerged aquatic vegetation on the velocity profiles within a shallow lake. The drag force was included as a sink term in the momentum equations and the k-ϵ scheme was used to model the turbulence. The velocity profiles predicted by the model were found to be in good agreement with those recorded at the site. The authors also compared the model to a simplified version, where the vegetation was only represented as an increase in the bed roughness. This showed that the drag force approach was more than twice as accurate as the bed roughness approach.

2.4 Summary

Over the past 60 years there have been a variety of investigations into the force exerted on prototype and full-scale flexible vegetation under aero- and hydrodynamic loading. The studies range from using small plant cuttings in a wind

tunnel (Hirata 1951), through to measuring the drag force of full-scale trees in towing tanks (Xavier 2009). However, there is still no universally agreed method for predicting the variation in drag force with velocity for flexible vegetation (Folkard 2011). This is due to a number of factors, such as the relative scarcity of comprehensive data sets, the heterogeneous and porous nature of a plant's branch and leaf structure, and the complexity of the resulting flow-field within that structure.

One of the main difficulties in the development of a universally applicable model, however, is the tendency of flexible vegetation to reconfigure and streamline in order to reduce the magnitude of the drag force it experiences (Vogel 1984, Aberle and Järvelä 2013). As a consequence, it is impractical to evaluate the projected area A_p at every required velocity and, at present, no computational approach exists to calculate it as a function of the flow conditions.

Furthermore, the drag coefficient C_d for a tree-like object is currently impossible to determine precisely *a priori* and is likely to be dependent on both velocity and tree morphology (Mayhead 1973, Vogel 1989, Gaylord *et al.* 1994, Armanini *et al.* 2005, Boller and Carrington 2006, Wunder *et al.* 2009, Dittrich *et al.* 2012). Additionally, both A_p and C_d depend on the presence and quantity of foliage, which has been identified to contribute significantly to drag (e.g. Vogel 1984, Armanini *et al.* 2005, Wilson *et al.* 2008, Västilä *et al.* 2011). Finally, the proportions of form and skin-friction drag with respect to the overall drag will also vary as the tree reconfigures into a more streamlined shape (Shames 2003, Sand-Jensen and Pedersen 2008, Wunder *et al.* 2011).

As a result of these issues, recent studies have focused on two approaches. The first relates the form factor f'' of an array of vegetation to the leaf area index and a number of species-specific parameters (Järvelä 2004, Västilä *et al.* 2011, Dittrich *et al.* 2012, Aberle and Järvelä 2013, Jalonen *et al.* 2013). This approach has been shown to be a useful and practical parameterization. It is also trivial to implement in numerical models. However, it requires extension to handle defoliated vegetation and is dependent on empirically derived values.

The second approach is based on dimensional analysis of the main processes that occur during aero- and hydro-dynamic loading of flexible vegetation and other flexible objects. A 'vegetative' Cauchy number is defined and used to

predict the reconfiguration of the vegetation based on a number of parameters, including flexural rigidity (de Langre 2008, Gosselin *et al.* 2010, Gosselin and de Langre 2011, Luhar and Nepf 2011). For simple geometries, this approach accurately predicts the magnitude of the reconfiguration, and thus drag force, with increasing velocity, without the need for empirical parameters. However, it remains to be seen whether such relationships can be applied to more complex, full-scale vegetation, such as trees and other riparian vegetation.

Chapter 3

Experimental Data and Analysis

3.1 Introduction

In this chapter, two experimental data sets of differing riparian plant scale are introduced. The first contains high-resolution drag force and physical property measurements for twenty-one foliated and defoliated submerged full-scale trees, including specimens of alder, poplar and willow (§ 3.2.1). The second data set is independent and consists of drag force and physical property measurements for natural and artificial branches of poplar, sedge and willow, under partially and fully submerged flow conditions (§ 3.2.2).

The testing of trees in both their foliated and defoliated states in the first experimental study allows the impact of foliage on the total drag force to be isolated and discussed (§ 3.3.1). The force-velocity data from both studies are then jointly used to quantify the deformation and reconfiguration of the trees when subject to hydrodynamic loading by examining the deviation of the drag force from a squared relationship with velocity (§ 3.3.2). The observed variation is compared to previous experimental drag force studies and any correlations between the extent of the reconfiguration and the trees' physical properties are also investigated.

In addition to the drag force and physical property measurements, further media were collected during the first study, including photographs of the trees in still air and video footage of the trees undergoing hydrodynamic loading. The

media are analysed here, using sophisticated image processing techniques, in order to provide both the trees' projected area in still air and the variation in projected area with flow velocity whilst towing (§ 3.4). The resulting projected areas at each flow velocity are then discussed, before being used to determine the corresponding variation in drag coefficient with velocity (§ 3.5).

3.2 Experimental Data

The drag force and physical property data sets analysed in this thesis are sourced from two previous experimental studies. The larger of the two data sets was collected at the Canal de Experiencias Hidrodinamicas de El Pardo (CEHIPAR), Madrid, within the framework of the EU Hydralab III scheme. The second data set is independent and was obtained from experiments undertaken at the Leichtweiß-Institut für Wasserbau (LWI), Technische Universität Braunschweig. The corresponding data sets are described below. It should be noted that only the raw data from the experiments are provided in this section and that the new and original analysis is performed in the following sections (§ 3.3–§ 3.5).

3.2.1 Hydralab Experiments

In this study, full-scale riparian trees (heights ranged from 1.8 m to 4.1 m, with an average of 2.9 m) were sampled from a local floodplain site and towed under fully-submerged conditions in a ship towing tank. In total, twenty-one full-scale trees were tested, including five *Alnus glutinosa* (common alder; A1–A5), four *Populus nigra* (black poplar; P1–P4), and twelve *Salix alba* (white willow; S1–S12) specimens. As the trees were collected during the spring months of mid March to mid April, a range of stages of leaf development were captured, from emerging leaf buds to more fully developed foliage.

The data were collected over a four week period during the spring of 2008 by members of Cardiff University (CU) in collaboration with Technische Universität Braunschweig (UB), Germany, the University of Natural Resources and Life Sciences (BOKU), Austria, and Forest Research UK (see Table 3.1). This section

provides the relevant data and an overview of the experimental procedure; full details can be found in Weissteiner (2009), Xavier (2009) and Xavier *et al.* (2010).

Table 3.1: List of participants in the Hydralab experiments. Reproduced from Xavier *et al.* (2010).

Person	Institute	Responsibility
Catherine Wilson	CU	Project leader
Jochen Aberle	UB	Drag force measurements
Hans-Peter Rauch	BOKU	Measurement of tree properties
Patricia Xavier	CU	Experimental work and force-velocity data analysis
Thomas Schoneboom	UB	Experimental work and force-velocity post-processing
Walter Lammeranner	BOKU	Determination of bending stiffness
Clemens Weissteiner	BOKU	Post-processing of tree properties
Huw Thomas	FR	Experimental work

Physical Properties

The tested trees were sourced at two week intervals from a local floodplain woodland site, rather than an artificial nursery, and were selected to cover a broad range of growth habitats (Weissteiner 2009). All trees were brought to the laboratory within five hours and kept with their stems submerged in the water of the canal. From visual inspection, the trees remained fresh and leaf growth was observed to continue for approximately two weeks before obvious signs of decay occurred, at which point they were discarded. It should be noted that the experimental time at the CEHIPAR facilities was limited so that not all of the properties could be determined for every tree.

Prior to the towing tank tests, the trees' physical dimensions were measured and recorded. This included the height H, and the diameter of the main stem at each quartile height (i.e. basal d_0, first-quartile d_{25}, mid-stem d_{50}, and third-quartile d_{75}). These properties are summarized in Table 3.2.

After a specimen had been tested in a foliated state, the foliage was removed and the fresh, or wet leaf mass $M_{L,w}$ was recorded using a scale with an accuracy of 0.1 g. The leaf volume V_L was determined by immersing the collected foliage in a known volume of water and recording the volume of water displaced. The foliage was then allowed to dry in a warm oven for at least 24 hours so that the

Table 3.2: Dimensions of the *A. glutinosa* (A), *P. nigra* (P) and *S. alba* (S) Hydralab trees. A dash (-) indicates data not recorded. The suffix 'B' denotes a branch cut from the tree with the same prefix.

Specimen	Height H (m)	Diam. d_0 (mm)	Diam. d_{25} (mm)	Diam. d_{50} (mm)	Diam. d_{75} (mm)
A1	2.45	58	29	25	11
A2	3.6	35	33	18	9
A3	2.6	28	21	16	5
A4	2.4	27	22	16	8
A5	1.8	28	20	12	8
Average	2.57	35.4	25	17.5	8
P1	2.68	35	18	12	8
P2	3.77	37	23	21	8
P2B1	3.77	37	23	21	8
P2B2	2.5	-	22	20	8
P3	2.6	23	20	16	7
P4	3.9	35	29	22	16
P4B1	2.3	22	-	16	-
P4B2	1.8	16	15	10	6
Average	2.92	29.1	21.4	17.3	8.8
S1	2.1	29	25	17	8
S2	2.4	26	21	11	3
S3	3.95	44	40	28	10
S4	2	23	16	9	5
S5	3.6	47	14	18	9
S5B1	3.6	47	14	18	9
S5B2	3.6	47	14	11	8
S6	3.2	25	12	9	5
S6B1	3.2	25	12	9	5
S6B2	2.8	-	16	8	4
S7	2.3	31	19	15	8
S7B1	2.3	31	19	15	8
S7B2	2.3	31	21	18	8
S7B3	2.18	31	19	14	7
S8	3	20	17	13	5
S9	3.6	29	23	14	7
S10	3.24	33	31	22	14
S11	3.5	26	18	11	7
S12	4.1	29	21	16	7
Average	3	32.1	19.5	14.6	7.2

dry leaf mass $M_{L,d}$ could be noted. Once a defoliated specimen had finished being tested, it was cut into sections and the wet mass $M_{S,w}$, volume V_S and dry mass $M_{S,d}$ of the wood was recorded using the same procedure as for the leaf matter. The trees' stem, leaf, and total volumes and masses are presented in Tables A.1–A.3, respectively.

In addition to the above properties, tests were also carried out to determine the trees' flexural rigidity EI and modulus of elasticity E. Each tree was fixed at its base to the edge of a secure table using G-clamps. Weights were then attached to the horizontal tree at either the first-quartile or mid-stem position and the resulting vertical deflection recorded. The weights were increased incrementally from 0.2 kg to 13 kg. The properties derived from placing weights at each position are denoted using a subscript suffix of 25 or 50 respectively. For example, EI_{50} would indicate the flexural rigidity calculated from placing weights at the mid-stem position.

Although classical beam bending theory (e.g. Coates *et al.* 1990) is derived for small deflections and based on the assumption that the beam is uniform in cross-section and has linear elasticity, it is often used in biomechanical studies of natural vegetation (Chen *et al.* 2011, Stone *et al.* 2011). Since the assumptions may not hold for natural vegetation (non-constant thickness, large deformations, differing properties of young and old wood, etc.) an averaging method was employed.

For each weight applied to the tree, the corresponding flexural rigidity value was calculated. Once the deflections became too large, no more weights were added and the previous flexural rigidity values were averaged to give a single result. While this method provides reasonably accurate approximations, a more detailed or rigorous procedure was outside the scope of this project. Representing the main stem as a beam of length L that is fixed at one end and has a concentrated load P at a distance l from the free end, the deflection δ can be expressed:

$$\delta = \frac{P}{3EI}(L - l)^3 \tag{3.1}$$

where $I = \frac{\pi r^4}{4}$ is the second moment of area for a circular cross-section of radius r.

Following the above procedure, flexural rigidity properties were calculated from placing weights at both the first-quartile (EI_{25}) and mid-stem (EI_{50}) heights. These are summarized in Table 3.3 for the alder, poplar and willow specimens, along with the equivalent modulus of elasticity values. Due to the tapering thickness of the trees' main stems, the average radius r of the stem between the base and the point of loading was used to determine I. The modulus of elasticity values reported in Table 3.3 are consistent with those given in the literature for similar willow trees (Green *et al.* 1999, Stone *et al.* 2011).

Table 3.3: Flexural rigidity and modulus of elasticity values for the *A. glutinosa* (A), *P. nigra* (P) and *S. alba* (S) Hydralab trees. A dash (-) indicates data not recorded. The suffix 'B' denotes a branch cut from the tree with the same prefix.

Specimen	EI_{25} (N m^2)	EI_{50} (N m^2)	E_{25} (N m^{-2})	E_{50} (N m^{-2})
A1	71	102	3.91×10^8	6.74×10^8
A2	430	249	6.49×10^9	1.03×10^{10}
A3	64	135	3.46×10^9	1.16×10^{10}
A4	106	82	5.96×10^9	7.58×10^9
A5	31	16	1.93×10^9	1.98×10^9
Average	140	117	3.64×10^9	6.43×10^9
P1	135	42	5.5×10^9	2.72×10^9
P2	122	184	3.23×10^9	5.48×10^9
P2B1	122	184	3.23×10^9	5.48×10^9
P2B2	37	43	-	-
P3	59	47	5.55×10^9	6.24×10^9
P4	664	541	1.22×10^{10}	1.66×10^{10}
P4B1	136	111	-	-
P4B2	-	-	-	-
Average	182	165	5.94×10^9	7.3×10^9
S1	-	-	-	-
S2	119	141	7.58×10^9	2.29×10^{10}
S3	367	559	2.34×10^9	6.81×10^9
S4	31	42	4.33×10^9	1.38×10^{10}
S5	-	-	-	-
S5B1	65	56	1.5×10^9	1.01×10^9
S5B2	157	51	3.79×10^9	1.44×10^9
S6	-	-	-	-
S6B1	20	18	3.4×10^9	4.06×10^9
S6B2	47	20	-	-
S7	-	-	-	-
S7B1	85	72	4.14×10^9	5.07×10^9
S7B2	84	48	3.68×10^9	2.66×10^9
S7B3	-	-	-	-
S8	35	40	5.89×10^9	1.06×10^{10}
S9	-	-	-	-
S10	258	349	4.89×10^9	1.24×10^{10}
S11	64	52	5.62×10^9	8.7×10^9
S12	141	174	7.45×10^9	1.4×10^{10}
Average	113	125	4.55×10^9	8.62×10^9

Drag Forces

The facilities at CEHIPAR included a calm water ship towing tank, with the following dimensions: 320 m long, 12.5 m wide and 6.5 m deep. A towing carriage was mounted on rails running the length of the canal (Fig. 3.1) and the speed at which it travelled in either direction could be set with an accuracy of 1 mm s^{-1}. The towing carriage had a maximum velocity of 10 m s^{-1} and a maximum acceleration of 1 m s^{-2}. A dynamometer, consisting of five separate load cells, was suspended underneath the carriage in order to measure the forces and moments in the three Cartesian axes at a rate of 10 Hz and with an accuracy of 9.8×10^{-3} N.

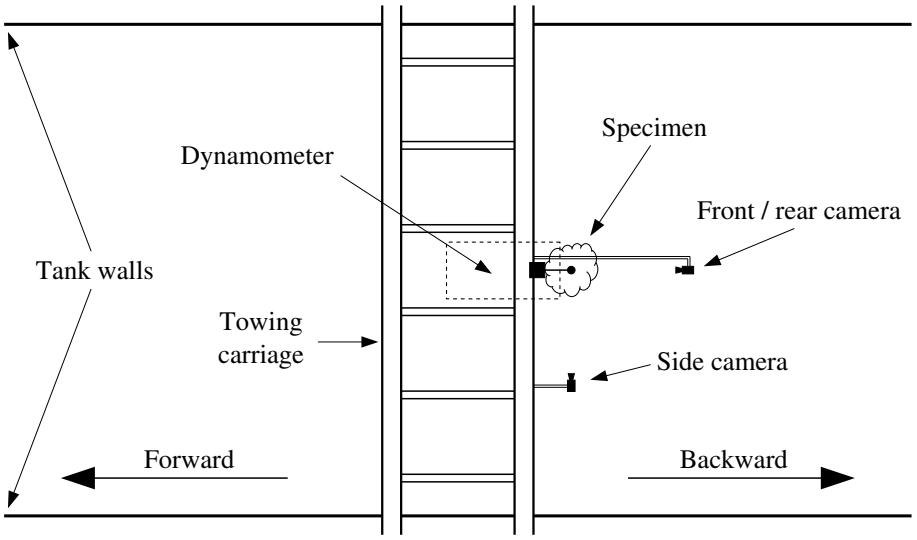

Figure 3.1: Plan view schematic of the towing carriage at the CEHIPAR facilities.

The tree specimens were attached upside down to the dynamometer so that they were fully submerged and were towed with velocities ranging from 0.125 m s^{-1} to 6 m s^{-1}. Although flood flows rarely reach such high velocities in practice, the large range provides important test cases for any proposed models. The use of fully submerged conditions was necessary due to the experimental facilities, but provides insight into the nature of the deformation of full-scale trees in extreme flow conditions.

To ensure repeatability of results each experiment was carried out twice, i.e. specimens were towed in both directions along the towing tank by the carriage. After each run the trees were rotated through 180 degrees in the dynamometer so that the direction of bending was consistent. Sufficient time (5–10 minutes) was also reserved between runs to allow any surface waves or eddies to dissipate before towing again.

The majority of trees were tested first in a foliated and then in a defoliated state. However, during preliminary tests it was observed that the trees exhibited apparent signs of inelastic deformation. It was therefore decided that the trees would be exposed to lower towing velocities while in their foliated state in order to minimize the impact on the subsequent defoliated tests.

Additionally, a number of trees were selected for further testing based on their branch morphology. These trees were only tested in a foliated state and then cut into their constituent stems, which were then tested separately in foliated and defoliated states. This allowed the contribution of the tree's branches to its overall drag force to be investigated. However, it also meant that the original main specimen could not be tested in a defoliated state since it was no longer whole. The sub-branches of the trees that contained multiple main stems are hereafter denoted using the suffix 'B' combined with the number of the respective sub-branch. For example, the first branch of the S5 tree is labelled S5B1, with the second branch being S5B2, and so on.

When undertaking the drag force testing, the length of the towing tank enabled multiple velocity readings to taken during a single run. However, the transition between velocities caused a small peak in the measured force which then subsided, as can be seen in Figure 3.2. This was due to the acceleration of the carriage as it increased its velocity to the next testing velocity.

In order to account for the peak at the start of each velocity time series and obtain representative values, a statistical analysis was carried out by Thomas Schoneboom of Technische Universität Braunschweig, Germany. On the basis of his analysis, the force and moment values were averaged over the 20 s period prior to the end of each velocity measurement where the recorded variation was minimal (Xavier 2009). The resulting variation in drag force with towing velocity for each of the Hydralab trees is presented in Figs. 3.3–3.5.

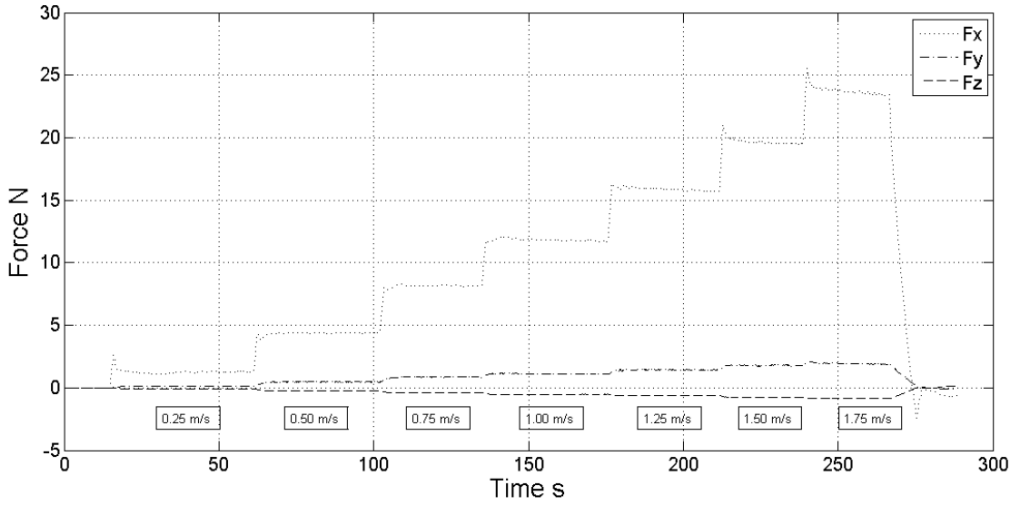

Figure 3.2: Component forces against time for a single run incorporating a number of velocities. Reproduced from Xavier (2009).

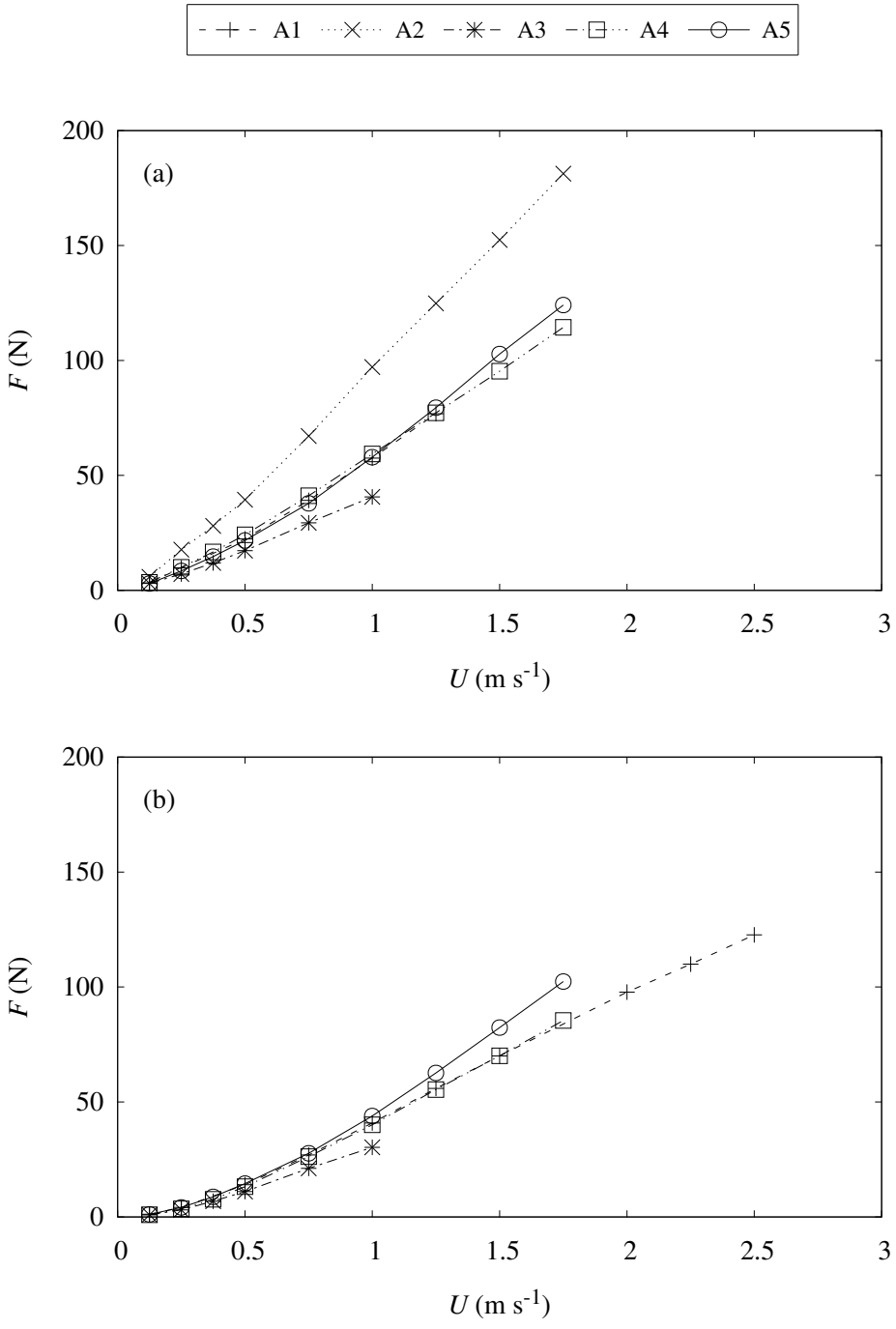

Figure 3.3: Variation in drag force with towing velocity for the: (a) foliated; and (b) defoliated *A. glutinosa* trees from the Hydralab experiments.

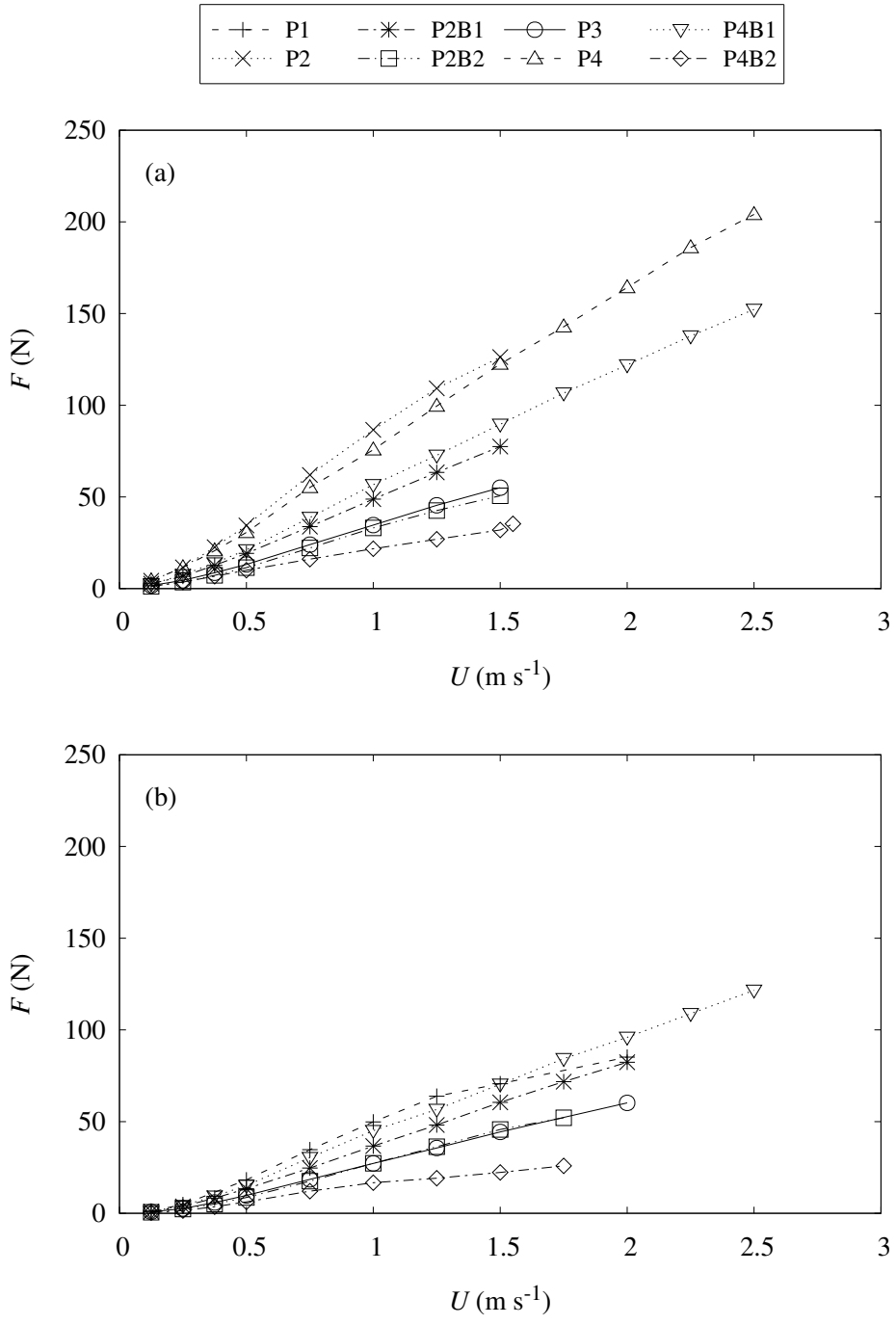

Figure 3.4: Variation in drag force with towing velocity for the: (a) foliated; and (b) defoliated *P. nigra* trees from the Hydralab experiments.

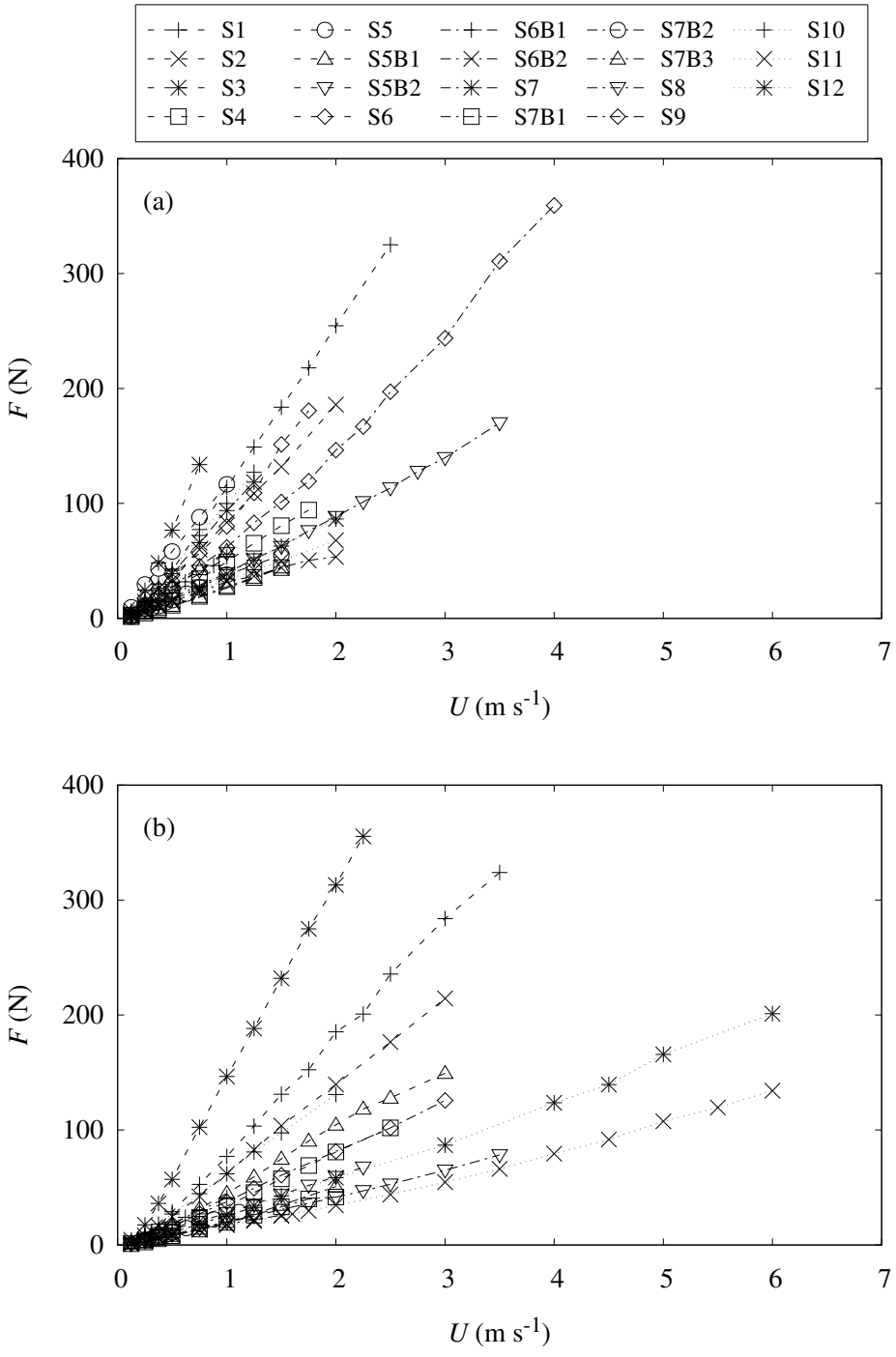

Figure 3.5: Variation in drag force with towing velocity for the: (a) foliated; and (b) defoliated *S. alba* trees from the Hydralab experiments.

3.2.2 LWI Experiments

The independent data used here are taken from flume experiments conducted at the Leichtweiß-Institut für Wasserbau (LWI), Technische Universität Braunschweig. The experimental set-up is described in detail in Schoneboom and Aberle (2009), Schoneboom (2011) and Dittrich *et al.* (2012). The data from this study consist of drag force and physical property measurements for isolated foliated branches of natural willow, natural poplar, and artificial poplar, tested in partially ($\zeta = 0.12$ m) and fully ($\zeta = 0.25$ m) submerged conditions (Fig. 3.6). The artificial poplar is included here as it has been found to show similar resistance behaviour to its natural counterparts (Dittrich *et al.* 2012).

(a) Natural willow

(b) Natural poplar

(c) Artificial poplar

Figure 3.6: Photographs of the fully submerged natural and artificial branches used in the LWI experiments. The images were captured in still water using a submersible digital camera.

Drag Forces

Drag forces were recorded using a custom strain gauge setup (described in detail in Schoneboom *et al.* 2008) that had a temporal resolution of 1613 Hz and an accuracy of 0.02 N. The drag force measurement system (DFS) was installed underneath a tilting flume measuring 32 m long, 0.6 m wide and 0.4 m deep. The flume bed was covered with a rubber mat with a pyramidal roughness height of 3 mm.

The individual branches were placed into the flume one at a time and secured to the DFS. Steady uniform flow was then obtained and the drag force on the individual branches measured at a rate of 200 Hz for a duration of 60 s. The measurements were carried out for a range of velocities ($0.198 \leq U \leq 0.957\ \mathrm{m\,s^{-1}}$) at two different water depths: partially submerged conditions ($\zeta = 12$ cm) and fully submerged conditions ($\zeta = 25$ cm). The resulting time-averaged drag forces at each velocity are presented in Fig. 3.7.

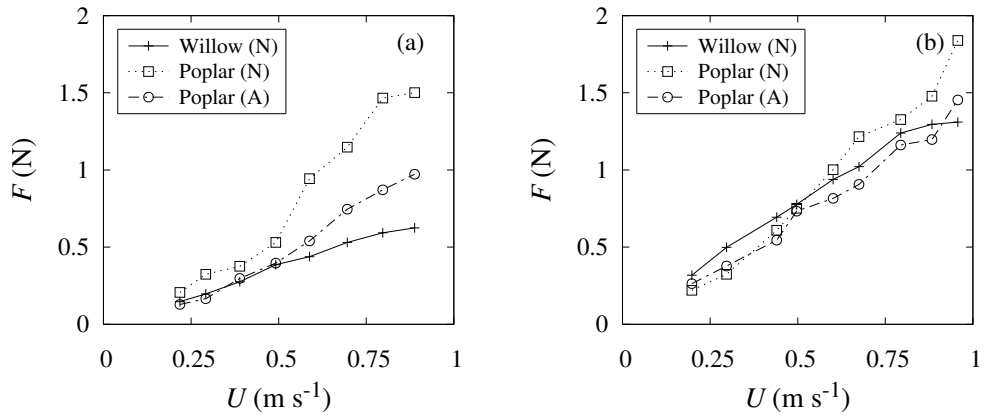

Figure 3.7: Variation in drag force with flow velocity for the: (a) partially submerged; and (b) fully submerged branches from the LWI experiments. The natural and artificial plants are denoted using (N) or (A), respectively.

Physical Properties

In addition to the force-velocity data, key physical properties, such as the stem diameter, height, total one-sided leaf area, and projected area in still water were

recorded (Schoneboom 2011). The images used to calculate the projected area in still water were obtained using a submersible digital camera and were taken from a front-facing direction. Although the projected area in still water is not directly comparable to the projected area in still air due to buoyancy effects, they are taken to be equivalent in this thesis as the buoyancy effects are observed to be minimal (see Fig. 3.6).

Bending stiffness tests were also carried out to determine the elastic modulus for the wire stem of the artificial poplar (Schoneboom 2011). For the two natural branches, main-stem elastic moduli are taken from the species-averaged values for the Hydralab trees (see Table 3.3).

The measured physical properties for the LWI branches are summarized in Table 3.4. Note that the water depth is used as the specimen height for the partially submerged cases. The proportion of the leaf area that was submerged in the partially submerged case was not listed in Schoneboom (2011).

Table 3.4: Measured physical properties of the poplar (P) and willow (W) LWI branches. The suffixes 'A' and 'N' denote artificial and natural branches, respectively, while '1' and '2' denote partially and fully submerged flow conditions, respectively.

Specimen	Height H (cm)	Stem diam. d (mm)	Elastic mod. E (N m^{-2})	Leaf area A_L (cm^2)	Proj. area A_{p0} (cm^2)
WN1	12	3.2	4.55×10^9 [a]	-	77
WN2	25	3.2	4.55×10^9 [a]	322	205
PN1	12	3.6	5.94×10^9 [a]	-	137
PN2	24	3.6	5.94×10^9 [a]	455	154
PA1	12	3	6.97×10^9	-	95
PA2	23	3	6.97×10^9	374	148

[a] Elastic modulus taken from Hydralab trees' species-average.

3.3 Drag Force Analysis

In this section, the force-velocity data sets from the Hydralab (§ 3.2.1) and LWI (§ 3.2.2) experiments are further analysed. The impact of the foliage on the total drag force is first investigated, although only for the Hydralab trees as the LWI branches were not tested in a defoliated condition. The reconfiguration of both

sets of specimens as a result of hydrodynamic loading is then quantified and discussed with regards to an existing metric, namely the Vogel exponent ψ (see Eq. 2.5).

3.3.1 Impact of Foliage

The testing of foliated and defoliated trees during the Hydralab experiments allows the impact of foliage on the overall drag force to be investigated by considering the ratio of the total foliated drag force to the defoliated drag force, i.e. $F_{\text{fol}} = (F_{\text{tot}} - F_{\text{defol}})/F_{\text{tot}}$. This analysis shows that as the velocity increases, the percentage of the drag force caused by foliage rapidly decreases until it becomes relatively constant with velocity for a given specimen (Fig. 3.8). This suggests that the reconfiguration and streamlining of the foliage (but not necessarily the entire tree) mostly occurs below a certain threshold velocity (see also Dittrich *et al.* 2012, Aberle and Järvelä 2013).

From examination of where the effect of foliage begins to become constant with velocity in Fig. 3.8, the threshold velocity appears to range from 0.35 $\mathrm{m\,s^{-1}}$ to 0.75 $\mathrm{m\,s^{-1}}$. This is in agreement with the findings of Västilä *et al.* (2013), who observed that the reconfiguration of foliated *Populus nigra* branches was mostly complete at flow velocities of 0.6 $\mathrm{m\,s^{-1}}$. At velocities below this threshold, the foliage of the trees in this study is responsible for a significant proportion (40% to 75%) of the total drag force. At higher velocities, the contribution of foliage to the total drag force is reduced and ranges from 10% to 50%.

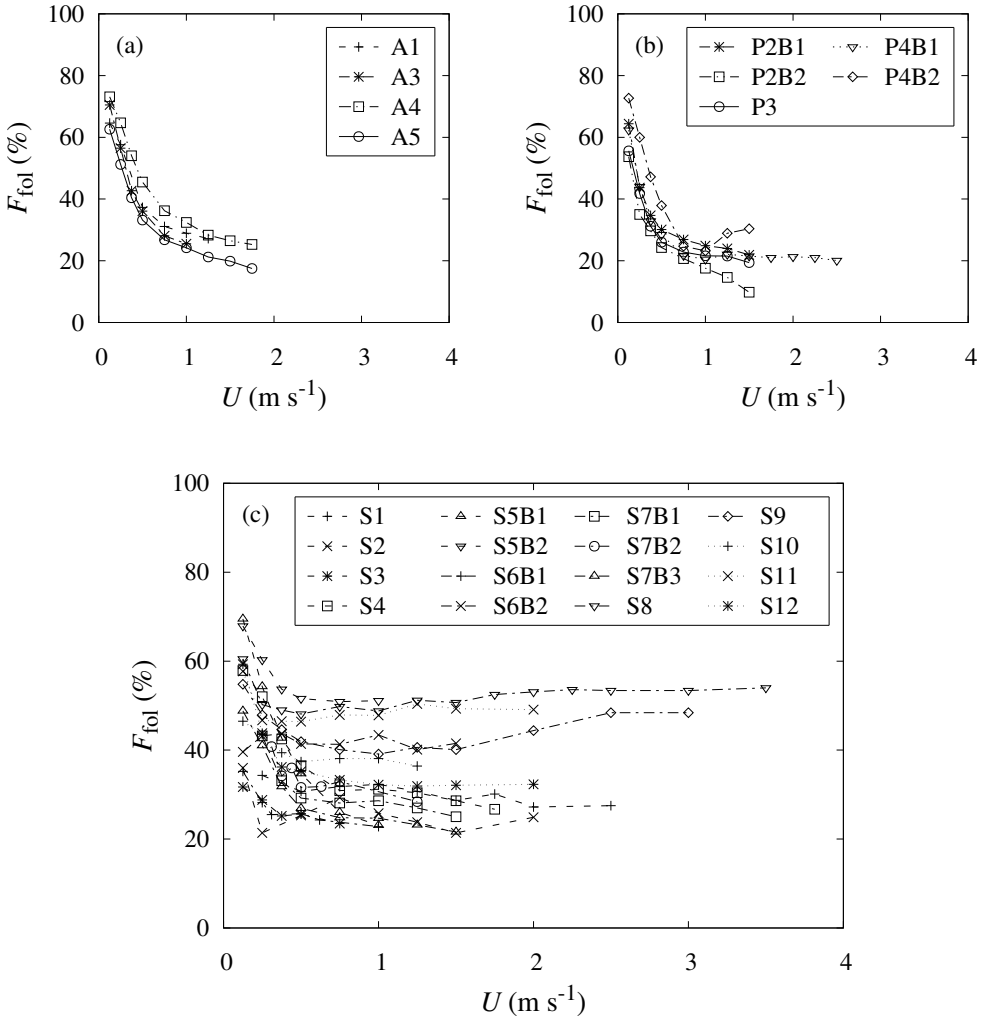

Figure 3.8: Proportion of total drag force caused by foliage for the: (a) *A. glutinosa*; (b) *P. nigra*; and (c) *S. alba* Hydralab trees.

3.3.2 Reconfiguration

Assuming that the density ρ of the water at the testing facilities was constant, it follows from Eq. (2.2) that any deviation away from a quadratic force-velocity response must be due to changes in the drag coefficient C_d and / or the projected area A_p. By combining these two terms into a 'characteristic' drag coefficient $C_d A_p$ (e.g. Wilson *et al.* 2008), any divergence in the drag force response from the classical, quadratic relationship can be discussed.

The variation in the characteristic drag coefficient with velocity is plot in Fig. 3.9 for the foliated and defoliated alder, poplar and willow Hydralab trees. The values for $C_d A_p$ were calculated by rearranging Eq. (2.2). For all specimens, it can be seen that the relationship between drag force and velocity does indeed deviate away from the quadratic law described by the classical drag equation (Eq. 2.2), which assumes that $C_d A_p$ is constant. This confirms the unsuitability of representing submerged flexible riparian woodland as rigid cylinders with the unmodified classical drag equation.

For the foliated trees, the characteristic drag coefficient decreases rapidly with velocity for $U \lesssim 0.5\ \mathrm{m\,s^{-1}}$ (Fig. 3.9), suggesting that the trees were subject to significant reconfiguration within this range. Above this velocity, the rate of change is not as great and at the highest velocities $C_d A_p$ is almost constant.

The variation in characteristic drag coefficient with velocity for the defoliated trees is slightly different to that of the foliated trees (see Fig. 3.9). Although there is a similar pattern of relatively rapid decrease in $C_d A_p$ with velocity before it becomes more constant, the velocities at which it happens are higher. There is also a region at the lowest velocities ($U \lesssim 0.5\ \mathrm{m\,s^{-1}}$) for which $C_d A_p$ is relatively constant. This initial response can be characterized as a 'stiff' regime, where the trees undergo minimal reconfiguration and thus act as a rigid object.

This 'stiff' regime is not exhibited for the foliated trees in Fig. 3.9 since the extra surface area of the foliage creates a larger drag force for a given velocity, thus forcing the trees to start reconfiguring at the lowest velocities tested here ($U = 0.125\ \mathrm{m\,s^{-1}}$). However, it is expected that the foliated trees would demonstrate such 'rigid' behaviour if lower velocities were tested during the experimental procedure.

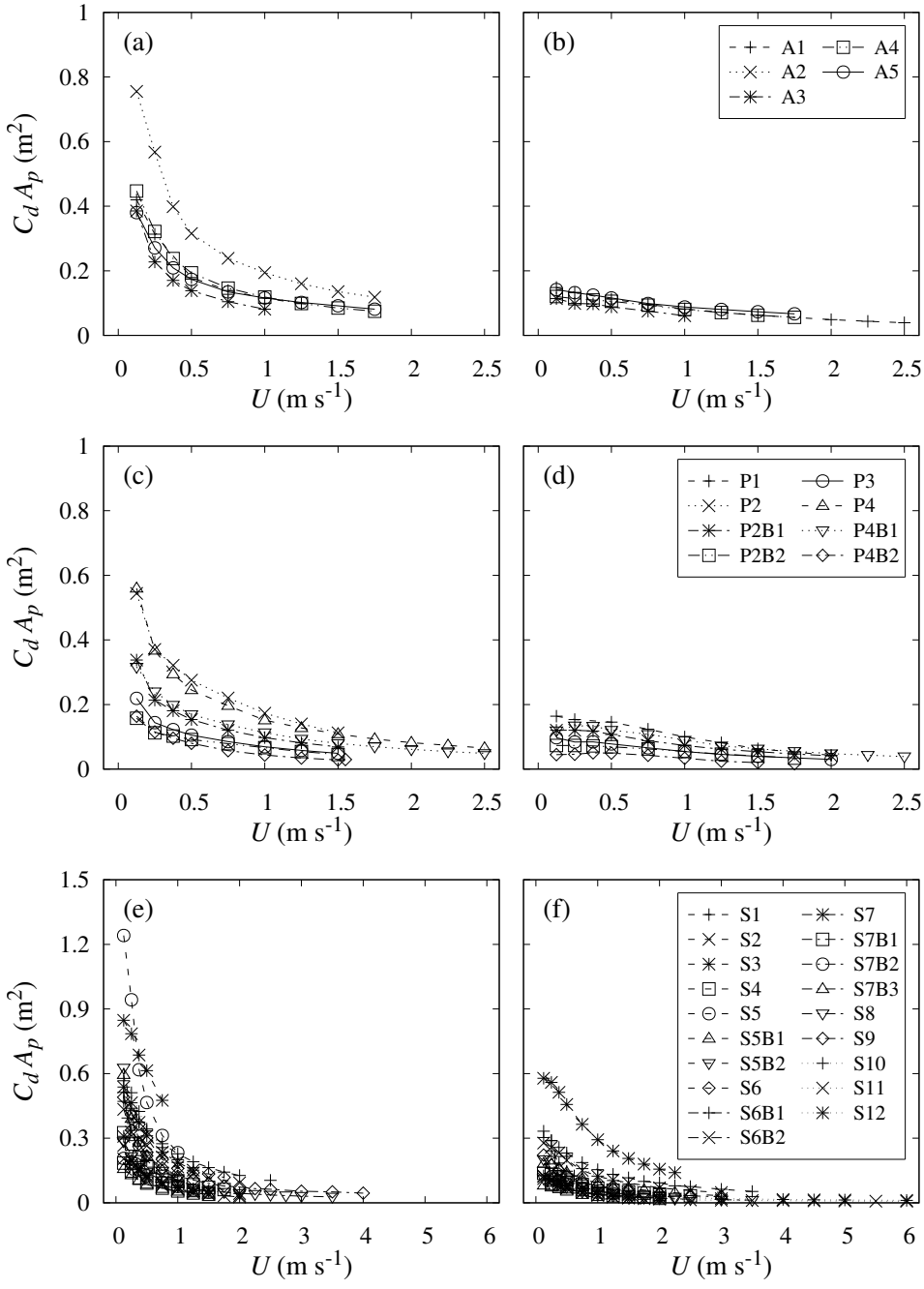

Figure 3.9: Variation in characteristic drag coefficient with velocity for the: (a,b) *A. glutinosa*; (c,d) *P. nigra*; and (e,f) *S. alba* Hydralab trees. The foliated and defoliated trees are in the left and right columns, respectively.

Values for $C_d A_p$ are also calculated for the LWI branches (Fig. 3.10) so that the effects of scale and relative level of submergence can be discussed. For the fully submerged branches, the variation in the characteristic drag coefficient with velocity is similar to that of the foliated Hydralab trees, suggesting that the mechanisms of reconfiguration are independent of vegetation scale. However, the reduction in $C_d A_p$ with velocity for the partially submerged branches appears to follow a more linear relationship, indicating that the rate of reconfiguration for these specimens was more gradual.

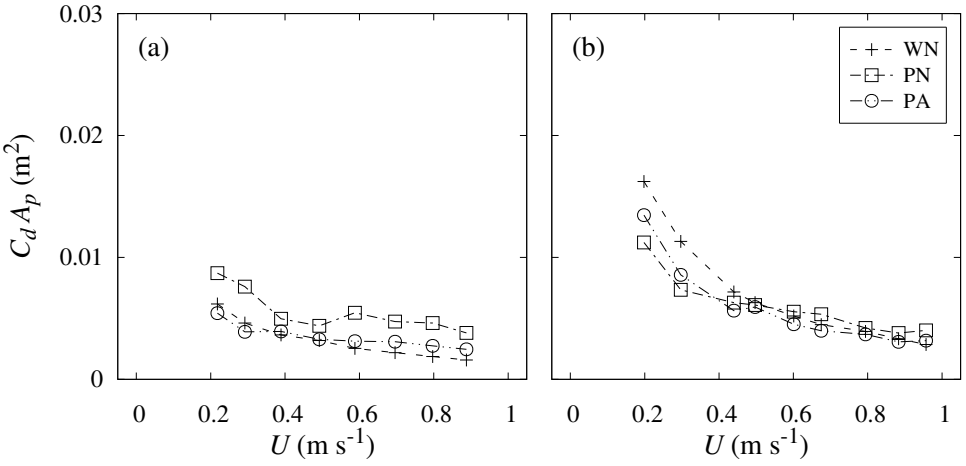

Figure 3.10: Variation in characteristic drag coefficient with velocity for the: (a) partially; and (b) fully submerged LWI branches.

Vogel Exponent Values: Hydralab Trees

Although the Vogel exponent ψ was originally formulated to investigate regions of high deformation (Vogel 1984), it has since been determined from the full force-velocity range in many studies involving flexible vegetation (Aberle and Dittrich 2012, Jalonen *et al.* 2013, Västilä *et al.* 2013). This is mainly due to the subjectivity of specifying lower or upper cut-off velocities. In this study, therefore, Vogel exponents are calculated from a power-law regression analysis using the full force-velocity range.

The resulting Vogel exponents and respective velocity ranges for the Hydralab trees are presented in Tables 3.5–3.7, with the species-averaged values given

in Table 3.8. The coefficient of determination R^2 was greater than 0.99 for the foliated trees, while for the defoliated trees $R^2 > 0.97$, thus verifying the power law as a suitable approximation.

Table 3.5: Vogel exponents obtained from a power-law regression on the full force-velocity data sets for the foliated and defoliated *A. glutinosa* Hydralab trees. The velocity ranges used in the regression analyses are also given.

	Foliated			Defoliated		
Specimen	U_{min} (m s^{-1})	U_{max} (m s^{-1})	ψ (-)	U_{min} (m s^{-1})	U_{max} (m s^{-1})	ψ (-)
A1	0.125	1.25	−0.677	0.125	2.5	−0.774
A2	0.125	1.75	−0.814	-	-	-
A3	0.125	1	−0.758	0.125	1	−0.501
A4	0.125	1.75	−0.777	0.125	1.75	−0.563
A5	0.125	1.75	−0.614	0.125	1.75	−0.456

Table 3.6: Vogel exponents obtained from a power-law regression on the full force-velocity data sets for the foliated and defoliated *P. nigra* Hydralab trees. The velocity ranges used in the regression analyses are also given.

	Foliated			Defoliated		
Specimen	U_{min} (m s^{-1})	U_{max} (m s^{-1})	ψ (-)	U_{min} (m s^{-1})	U_{max} (m s^{-1})	ψ (-)
P1	-	-	-	0.125	2	−1.002
P2	0.125	1.5	−0.826	-	-	-
P2B1	0.125	1.5	−0.737	0.125	2	−0.739
P2B2	0.125	1.5	−0.693	0.125	1.75	−0.655
P3	0.125	1.5	−0.718	0.125	2	−0.749
P4	0.125	2.5	−0.885	-	-	-
P4B1	0.125	2.5	−0.856	0.125	2.5	−0.825
P4B2	0.125	1.55	−0.881	0.125	1.75	−0.908

Before discussing the Vogel exponent, it is noted that the terms 'greater' and 'lesser' in this context refer to the magnitude of the exponent, rather than its absolute value, since a more negative exponent implies a greater degree of reconfiguration. For instance, an exponent of $\psi = -0.75$ is said to be greater than an exponent of $\psi = -0.50$. The Vogel exponents and the corresponding species-averaged values for the Hydralab trees are also illustrated in Fig. 3.11.

Table 3.7: Vogel exponents obtained from a power-law regression on the full force-velocity data sets for the foliated and defoliated *S. alba* Hydralab trees. The velocity ranges used in the regression analyses are also given.

	Foliated			Defoliated		
Specimen	U_{min} (m s^{-1})	U_{max} (m s^{-1})	ψ (-)	U_{min} (m s^{-1})	U_{max} (m s^{-1})	ψ (-)
S1	0.125	2.5	−0.8	0.25	3.5	−0.866
S2	0.125	2	−0.796	0.125	3	−0.857
S3	0.125	0.75	−0.509	0.125	2.25	−0.835
S4	0.125	1.75	−0.799	0.125	2.5	−0.78
S5	0.125	1	−0.97	-	-	-
S5B1	0.125	1	−0.869	0.125	3	−0.892
S5B2	0.125	1	−0.92	0.125	2.25	−0.894
S6	0.25	1.75	−0.641	-	-	-
S6B1	0.125	1	−0.849	0.125	1	−0.808
S6B2	0.125	2	−1.054	0.125	1.6	−0.978
S7	0.125	1.25	−0.757	-	-	-
S7B1	0.125	1.5	−0.771	0.25	2	−0.825
S7B2	0.125	1.5	−0.857	0.31	1.25	−0.76
S7B3	0.125	1.5	−0.705	0.125	2	−0.64
S8	0.125	3.5	−0.837	0.125	3.5	−0.895
S9	0.125	4	−0.707	0.125	3	−0.891
S10	0.125	1.25	−0.787	0.125	2	−0.862
S11	0.125	2	−0.94	0.125	6	−0.777
S12	0.125	2	−0.797	0.125	6	−0.843

Table 3.8: Species-averaged Vogel exponents obtained from a power-law regression on the full force-velocity data sets for the foliated and defoliated Hydralab trees. The standard deviations around the averaged values are also given.

	Foliated		Defoliated	
Species	ψ	σ	ψ	σ
A. glutinosa	−0.728	0.081	−0.573	0.141
P. nigra	−0.799	0.081	−0.813	0.126
S. alba	−0.809	0.122	−0.838	0.076
All specimens	−0.794	0.11	−0.791	0.135

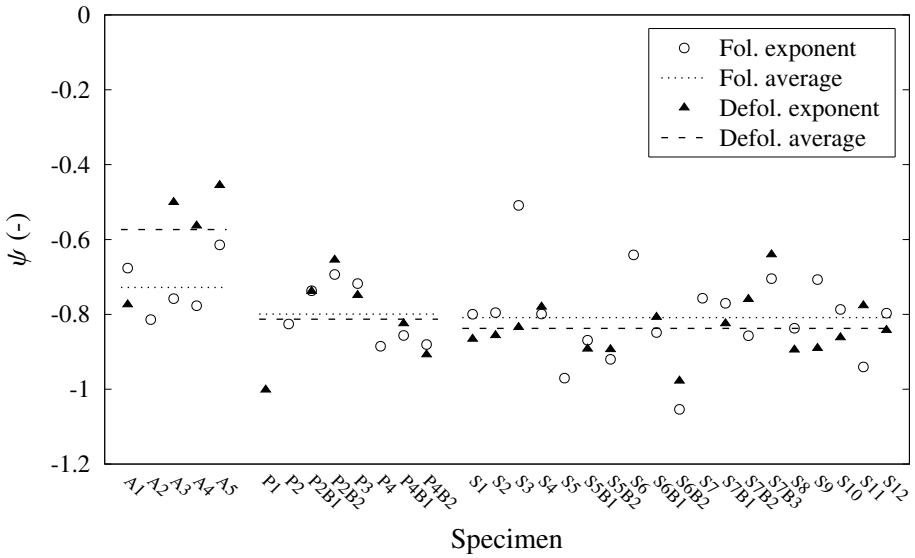

Figure 3.11: Individual and species-averaged Vogel exponents obtained from a power-law regression on the full force-velocity data sets for the *A. glutinosa* (A), *P. nigra* (P) and *S. alba* (S) Hydralab trees.

From Tables 3.5–3.7, it can be seen that the Vogel exponents obtained here are roughly similar in magnitude, with the minimum and maximum values being -0.46 and -1.05, respectively. It might be expected that the Vogel exponents for the foliated trees would be greater than those for the defoliated trees (i.e. ψ_{fol} more negative than ψ_{defol}) since the addition of foliage significantly increases the total drag force, and thus reconfiguration, for a given velocity (Fig. 3.8). Indeed, this is found to be the case for the majority of the alder trees (Table 3.5). However, for the alder specimen A1 and the majority of the poplar and willow trees, the opposite is found to be true (ψ_{fol} is less negative than ψ_{defol}).

The reason for this behaviour is that for the majority of the alder trees, the maximum towing velocities were equal for the foliated and defoliated states (i.e. $U_{\text{max,fol}} = U_{\text{max,defol}}$). On the other hand, the alder specimen A1 and the majority of the poplar and willow trees were tested to higher velocities when in a defoliated state. Therefore, the regression analyses for those specimens included more points at higher velocities, where $\psi \approx -1$, than the foliated analyses and the resulting Vogel exponents are correspondingly more negative.

Considering the species individually, it can be seen from Table 3.8 and Fig. 3.11 that the alder trees tend to have a Vogel exponent that is less negative than the other two species. This behaviour is especially evident when the alder trees are in a defoliated state, with the exponents of the trees A3, A4 and A5 accounting for three of the least negative exponents overall. The results thus suggest that the alder trees are less flexible than the poplar and willow specimens currently tested. However, the alder specimens actually had the lowest (i.e. most flexible) average E_{25} and E_{50} values (Table 3.3).

This may seem contradictory, but, as previously discussed, is most likely a result of the generally lower $U_{\max}$ values obtained for the alder trees compared to the poplar and willow trees (Tables 3.5–3.7). In addition, the variation could be due to branch morphology and the distribution of flexural rigidity over the entire tree. For example, while the alder specimens had more flexible main stems (EI_{25} and EI_{50} values), their outer branches may have been thicker and thus less flexible than those of the poplar and willow specimens. The mode of reconfiguration is also likely to differ between species, therefore further altering the Vogel exponent.

Regardless of these issues, the Vogel values calculated here are consistent with those reported in the literature. For example, Västilä *et al.* (2013) tested arrays of foliated *P. nigra* branches in a tilting flume and evaluated an average Vogel exponent of -1.03 using the full velocity range (0.03 m s^{-1} to 0.61 m s^{-1}). This is close to the value of $\psi = -1.0$ for the foliated poplar specimen P1, although the average exponent for the foliated poplar trees in the present study is lower at -0.799 (Table 3.8). The difference may be due to the fact that only one tree at a time was tested in the current study, as opposed to the arrays of branches utilized in the aforementioned study. Further, the difference in scale (trees versus small branches) and range of testing velocities between the two studies could be responsible for some variation.

Västilä *et al.* (2013) summarized additional exponent values from similar experiments (Järvelä 2004, 2006, Schoneboom *et al.* 2010) involving *Salix caprea* ($\psi = -0.57$), *Salix triandra x viminalis* ($\psi = -0.90$), and artificial branches ($\psi = -0.74$). These values are in good agreement with those presented here for the *S. alba* trees.

Vogel Exponent Values: LWI Branches

The Vogel exponents from power-law regression analyses of the full force-velocity ranges for the LWI branches are summarized in Table 3.9, along with the upper and lower velocities. The coefficient of determination R^2 was greater than 0.98 for all specimens.

Table 3.9: Vogel exponents obtained from a power-law regression on the LWI data sets for the partially and fully submerged branches. Both the natural (N) and artificial (A) plants are included. The velocity ranges used in the regression analyses are also given.

	Partially sub.			Fully sub.		
Specimen	$U_{\min}$ ($\mathrm{m\,s^{-1}}$)	$U_{\max}$ ($\mathrm{m\,s^{-1}}$)	ψ (-)	$U_{\min}$ ($\mathrm{m\,s^{-1}}$)	$U_{\max}$ ($\mathrm{m\,s^{-1}}$)	ψ (-)
Willow (N)	0.218	0.888	−1	0.198	0.957	−0.677
Poplar (N)	0.218	0.888	−0.467	0.198	0.957	−0.679
Poplar (A)	0.218	0.888	−0.51	0.198	0.957	−0.883

It can be seen that, apart from the natural willow branch, the Vogel exponent is greater (i.e. more negative) when the branches are fully submerged. This is consistent with the idea that the Vogel exponent is a measure of the rate of reconfiguration; a specimen will deform more for a given velocity when fully submerged than compared to when it is partially submerged, since the bending moment acting on the main stem will be greater due to the increased drag force and lever arm length. The reason that the Vogel exponent for the natural willow branch is greater when partially submerged is perhaps due to experimental error. For example, there is a slight bump in the fully submerged drag force for this specimen at $U \approx 0.8\ \mathrm{m\,s^{-1}}$ (see Fig. 3.7b). The small number of specimens tested at the LWI facilities, however, makes it difficult to determine whether this exception is an error or an unknown physical phenomenon.

Examining the Vogel exponent values for the fully submerged natural poplar and willow LWI branches (Table 3.9), it can be seen that there is general agreement with the values determined for the foliated poplar and willow trees from the Hydralab study (Tables 3.6 and 3.7, respectively). The Vogel exponent for the LWI poplar is closer to the Hydralab poplar species-average value in Table 3.8

than the value for the LWI willow is to the Hydralab willow species-average. However, as previously discussed, the Vogel exponent for the fully submerged natural willow from the LWI experiments may have been affected by experimental error.

It is also interesting to note that the Vogel exponents determined here for the LWI willow and poplar branches differ slightly from those reported in Dittrich *et al.* (2012). This is due to the authors using a linear least squares regression analysis after transforming the force-velocity data onto log-log space, whereas in this study a non-linear least squares regression analysis based on the Levenberg-Marquardt algorithm is utilized. The method used here is marginally more accurate, with $R^2 \geq 0.986$ compared to $R^2 \approx 0.98$ given in Dittrich *et al.* (2012). This highlights the need for consistent and robust regression methodologies across studies when dealing with power laws (Clauset *et al.* 2009).

Physical Property Correlation

In order to investigate whether the Vogel exponent may be predicted *a priori*, linear regression analyses were performed with respect to the Hydralab trees' physical properties, including: height H; diameter of the main stem at each quartile height (i.e. basal d_0, first-quartile d_{25}, mid-stem d_{50}, and third-quartile d_{75}); total wet M_w and dry M_d masses; wood-only wet $M_{S,w}$ and dry $M_{S,d}$ masses; total V and wood-only V_S volumes; main-stem modulus of elasticity E; and main-stem flexural rigidity EI.

The resulting coefficients of determination are presented in Table 3.10 for all of the Hydralab trees combined and in Table 3.11 for the individual species. Physical property correlations are not determined for the LWI branches as there are an insufficient number of specimens.

It can be seen that there is essentially no correlation between the Hydralab trees' physical properties and the Vogel exponent when the species are combined (Table 3.10). When the species are taken separately (Table 3.11), there appear to be possible correlations for the alder and poplar trees. However, on closer inspection, the higher R^2 values can be attributed to the small sample sizes ($N < 5$).

Table 3.10: Coefficients of determination obtained from linear regression analyses of the variation in Vogel exponent with the Hydralab trees' physical properties. The number of data points N used in each regression analysis is also given.

	Foliated		Defoliated	
Property	R^2	N	R^2	N
H (m)	0.01	31	0.11	26
d_0 (mm)	0	29	0.01	24
d_{25} (mm)	0.21	30	0.01	25
d_{50} (mm)	0.14	31	0.02	26
d_{75} (mm)	0.01	30	0	25
M_w (g)	0.11	30	0.02	24
M_d (g)	0.03	19	0	14
V (cm^3)	0.07	24	0.08	20
$M_{S,w}$ (g)	0.14	30	0.01	25
$M_{S,d}$ (g)	0	25	0.01	20
V_S (cm^3)	0.09	27	0.01	23
E_{25} ($N\,m^{-2}$)	0.17	21	0.05	19
E_{50} ($N\,m^{-2}$)	0.02	21	0	19
EI_{25} ($N\,m^2$)	0	24	0.07	22
EI_{50} ($N\,m^2$)	0.09	24	0.01	22

Table 3.11: Coefficients of determination obtained from linear regression analyses of the variation in Vogel exponent with the Hydralab trees' physical properties. The number of data points N used in each regression analysis is also given.

	A. glutinosa				*P. nigra*				*S. alba*			
Property	R^2_{fol}	N	R^2_{defol}	N	R^2_{fol}	N	R^2_{defol}	N	R^2_{fol}	N	R^2_{defol}	N
H (m)	0.69	5	0.2	4	0	7	0.11	6	0	19	0.13	16
d_0 (mm)	0.05	5	0.88	4	0.04	6	0	5	0.01	18	0.06	15
d_{25} (mm)	0.18	5	0.99	4	0.01	6	0.6	5	0.33	19	0	16
d_{50} (mm)	0.01	5	0.96	4	0.08	7	0.74	6	0.2	19	0	16
d_{75} (mm)	0.05	5	0.63	4	0.18	6	0.07	5	0.03	19	0	16
M_w (g)	0.26	4	0.88	3	0.23	7	0	5	0.28	19	0.03	16
M_d (g)	-	2	-	1	0.21	7	0	5	0.35	10	0.01	8
V (cm^3)	0.41	4	0.65	3	0.96	3	0.94	3	0.24	17	0.04	14
$M_{S,w}$ (g)	0.24	4	0.85	3	0.21	7	0	6	0.3	19	0.02	16
$M_{S,d}$ (g)	-	2	-	1	0.18	7	0	6	0.03	16	0.07	13
V_S (cm^3)	0.38	4	0.23	3	0.28	5	0.07	5	0.26	18	0.01	15
E_{25} ($N\,m^{-2}$)	0.72	5	0.21	4	0.45	4	0.27	3	0.04	12	0	12
E_{50} ($N\,m^{-2}$)	0.72	5	0.23	4	0.6	4	0.94	3	0.03	12	0	12
EI_{25} ($N\,m^2$)	0.48	5	0.14	4	0.51	6	0.53	5	0.5	13	0	13
EI_{50} ($N\,m^2$)	0.65	5	0.14	4	0.51	6	0.04	5	0.65	13	0	13

The lack of correlation between the Vogel exponent and the trees' physical properties is somewhat unexpected, but is possibly related to the difficulty in classifying the reconfiguration of complex objects such as full-scale trees. For example, the differing flexural rigidities of the stem, branches and leaves are not recorded in the current study. Any relationship between the Vogel exponent and a tree's physical properties may also not be linear, as assumed here.

Therefore, it is recommended that the species-averaged Vogel exponents are used to classify the trees. This is supported by the lower standard of deviations seen in Table 3.8 for the species-averaged values as compared to the overall-averaged values. The use of species-specific Vogel exponents is also common in previous studies (e.g. Järvelä 2004, Aberle and Dittrich 2012) and provides a more practical metric for any reconfiguration models.

3.4 Projected Area Analysis

In this section, the photographs and videos of the Hydralab trees are analysed to determine the trees' projected areas, both in still air and during drag force testing. Quantifying exactly how the projected area varies with flow velocity is important as it allows the rate of the trees' reconfiguration in response to increasing flow velocity to be investigated.

3.4.1 In Still Air

Specimen Leaf Area

Once the trees had been drag force tested in a foliated state, the leaves and buds were removed so that they could be tested in a defoliated state (§ 3.2.1). During this defoliating process, the leaves and buds were collected so that their physical properties, such as wet and dry mass, volume and density, could be recorded (Table A.2). In addition to these properties, the leaves from a selection of trees were scanned using an A4 digital scanner, with the leaves pressed flat and not overlapping (Weissteiner 2009). Not all specimens were chosen to have their leaves scanned due to time constraints at the experimental facilities.

Due to the large sizes of the trees, only 100 leaves were scanned for each selected tree. The dry masses $M_{L,d}^{100}$ were also recorded for those 100 leaves. This enables the specific leaf area (SLA) to be calculated as the ratio of the one-sided area per 100 leaves to their dry mass, i.e. $A_L^{100}/M_{L,d}^{100}$. Combining the SLA values with the measurements for the total dry leaf masses $M_{L,d}$ (Table A.2) thus allows the total one-sided leaf areas A_L to be estimated. In this study, the procedure used to analyse the scanned images and calculate A_L can be summarized as:

1. Isolate the leaf pixels from the background by selectively removing certain colours using GIMP (v2.8).

2. Determine the area per pixel by using the known dimensions of the scanned image (A4).

3. Calculate A_L^{100} by multiplying the number of leaf pixels by the area per pixel.

4. Calculate the specific leaf area as the ratio of the one-sided area to the dry mass for each set of 100 leaves, i.e. SLA $= A_L^{100}/M_{L,d}^{100}$.

5. Calculate the total one-sided leaf area by multiplying the SLA by the total dry leaf mass, i.e. $A_L = \text{SLA} \times M_{L,d}$.

The resulting one-sided leaf areas for the selected trees are presented in Table 3.12. Unfortunately the dry mass of the 100 leaves for the alder specimen A3 was not recorded and therefore an equivalent total one-sided leaf area cannot be computed.

Specimen Stem Area

Once the defoliated trees had been drag force tested, they were cut into sections so that they could be placed in an oven and the dry mass recorded (§ 3.2.1). Before being dried, however, the stem and branch sections for three specimens were sorted into quartiles and photographed on a large white table using a high resolution digital camera (Canon EOS 400D). A sheet of coloured A4 paper and a red plastic ball of known diameter ($d = 62$ mm) were also included for scale. Not

Table 3.12: Total one-sided leaf area for the *A. glutinosa* (A), *P. nigra* (P) and *S. alba* (S) Hydralab trees. The one-sided area and dry mass per 100 leaves are also given.

Specimen	A_L^{100} (m^2)	$M_{L,d}^{100}$ (g)	A_L (m^2)
A1	0.065	2.59	0.797
A2	0.1	4.8	0.998
A3	0.118	-	-
A4	0.082	3.33	0.735
A5	0.09	3.45	0.576
P2	0.048	1.6	1.086
P3	0.052	2.05	0.408
P4	0.066	3.7	1.201
S4	0.01	0.48	0.692
S7	0.014	0.45	1.29

all trees were chosen to have their stems photographed due to time constraints at the experimental facilities.

In this thesis, the images are analysed to obtain the total one-sided stem and branch area A_S. The procedure can be summarized as:

1. Isolate the stem pieces from the background by selectively removing certain colours using GIMP (v2.8).

2. Isolate the red plastic ball and sheet of A4 paper, again using GIMP.

3. Determine the area per pixel by using the known dimensions of the red ball and the sheet of A4 paper.

4. Calculate the total stem area for each quartile by multiplying the number of stem pixels by the area per pixel.

The one-sided stem area per quartile for each of the selected trees is shown in Fig. 3.12. The error bars indicate the minimum and maximum values calculated by using either the ball or paper derived pixel area, rather than the average of the two. The total one-sided stem area for each specimen is also given in Table 3.13. Note that the experimental time at the CEHIPAR facilities was limited so that it was not possible to photograph the stems of every tree.

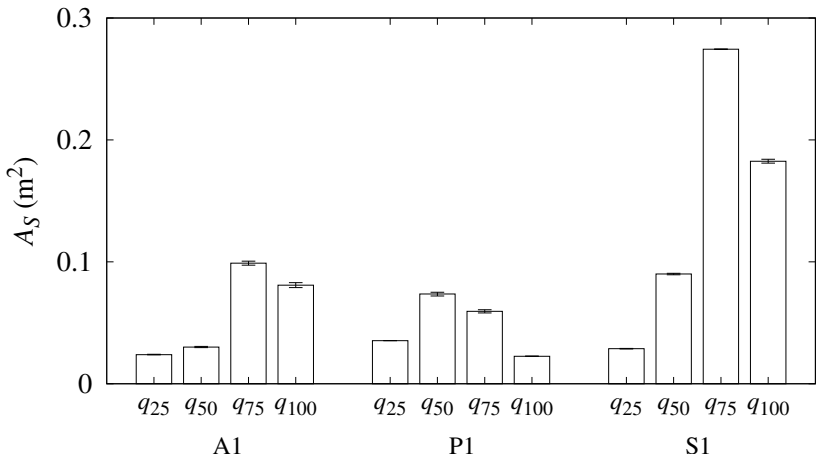

Figure 3.12: One-sided stem area per quartile for the *A. glutinosa* (A), *P. nigra* (P) and *S. alba* (S) Hydralab trees. Error bars show minimum and maximum values depending on pixel area definition.

Table 3.13: Total and per-quartile one-sided stem area for the *A. glutinosa* (A), *P. nigra* (P) and *S. alba* (S) Hydralab trees.

Specimen	H_1 (%)	H_2 (%)	A_S (m^2)
A1	0	25	0.0239
A1	25	50	0.0301
A1	50	75	0.0989
A1	75	100	0.0809
		Total	0.234
P1	0	25	0.0353
P1	25	50	0.0736
P1	50	75	0.0594
P1	75	100	0.0225
		Total	0.191
S1	0	25	0.0288
S1	25	50	0.09
S1	50	75	0.2744
S1	75	100	0.1825
		Total	0.576

It can be seen from Fig. 3.12 that the variation in stem area as derived from using either the plastic ball, the A4 sheet of paper, or an average of the two is essentially negligible. This thus shows that image processing technique used here is valid and that there is minimal error in the reported A_S values.

Specimen Total Area

In addition to the photographs of the stems, the trees were photographed in still air before drag force testing. The procedure can be summarized as:

1. The tree's stem was securely tied to a metal stand, with the tree orientated such that a red arrow on one of the stand's four bases corresponded to the direction in which the tree was later towed.

2. The stand was then placed directly in front of a large white sheet in order to obscure any background items.

3. A red plastic ball of known diameter (62 mm) was then attached to the top of a tripod and positioned next to the tree.

4. The tree was then photographed using a high resolution digital camera (Canon EOS 400D) and the stand rotated by 90 degrees until each 'face' and the plan view had been photographed.

This was carried out for all of the foliated trees, except for the poplar specimen P1 and the willow specimen S2 which were photographed in a defoliated state. The procedure used here to calculate the projected area of the trees from the images is as follows:

1. Isolate the tree from the background / foreground by selectively removing certain colours and regions using GIMP (v2.8).

2. Isolate the red plastic ball from the rest of the image, again using GIMP.

3. Determine area per pixel using the known diameter of the red ball.

4. Count the number of tree pixels using ImageMagick (v6.8) and multiply by the area per pixel to generate the total projected area in still air.

The projected areas for each of the four 'faces' (here termed north, east, south, and west, with north being the projected area while towing) and the plan view are presented in Table 3.14.

Table 3.14: Projected area in still air for the foliated *A. glutinosa* (A), *P. nigra* (P) and *S. alba* (S) Hydralab trees. The directions correspond to projected areas for each 'face' of the tree, with north being the projected area while towing. A dash (-) indicates data not recorded. Note that the specimens P1 and S2 are defoliated and are not included in their respective species' average.

Specimen	North (m^2)	East (m^2)	South (m^2)	West (m^2)	Top (m^2)
A1	0.523	0.421	0.552	0.439	0.331
A2	0.664	0.617	0.783	0.568	0.947
A3	0.398	-	0.4	0.392	0.307
A4	0.387	0.422	0.44	0.429	0.299
A5	0.333	0.356	0.358	0.382	0.241
Average	0.46	0.45	0.51	0.44	0.42
P1 [a]	0.159	0.163	0.155	0.137	0.068
P2	0.567	0.721	0.835	0.63	1.024
P3	0.269	0.312	0.382	0.304	0.185
P4	0.709	0.703	0.659	0.681	0.542
Average	0.52	0.58	0.63	0.54	0.58
S1	0.5	0.469	0.544	0.521	0.494
S2 [a]	0.235	0.201	0.208	0.189	0.215
S3	1.025	0.848	0.931	0.765	0.912
S4	0.304	0.287	0.33	0.304	0.316
S5	1.559	1.219	0.747	0.883	0.5
S6	0.636	0.804	0.831	0.689	0.524
S7	0.539	0.569	0.502	0.541	0.35
S8	0.393	0.348	0.333	0.261	0.22
S9	0.506	0.575	0.697	0.601	0.481
S10	0.601	0.688	0.708	0.68	0.505
S11	0.41	0.265	0.277	0.278	0.223
S12	0.28	0.459	0.374	0.45	0.282
Average	0.61	0.59	0.57	0.54	0.44

[a] Defoliated trees (not included in species-average).

Theoretically, the north and south projected areas should be equal; however, errors may be introduced in the programmatic isolation of the tree pixels from the foreground / background image. This is visualized in Fig. 3.13, where the

projected areas for the north, south and an average of the two are presented for each Hydralab tree.

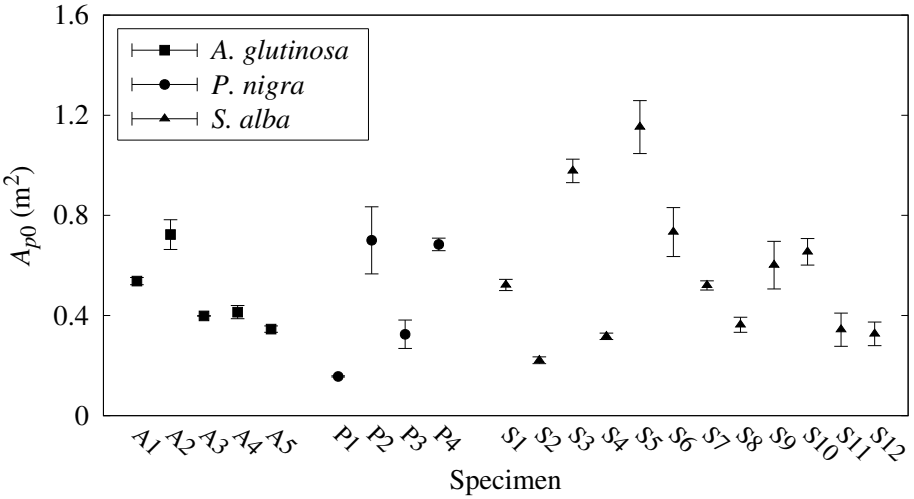

Figure 3.13: Minimum, maximum, and average of the north and south projected areas in still air for the foliated *A. glutinosa* (A), *P. nigra* (P) and *S. alba* (S) Hydralab trees. Note that the specimens P1 and S2 are defoliated.

It can be seen from Fig. 3.13 that, for most trees, the north and south projected areas are in good agreement. However, for a couple of the trees, namely the poplar P2 and the willows S5, S6 and S9, there is more significant divergence. Therefore, in order to minimize any uncertainty introduced during the image analysis, the average of the north and south projected areas, denoted A_{p0}, is used hereafter as the reference projected area in still air.

Before presenting the values for A_{p0}, it is interesting to note that the total one-sided stem area for the poplar specimen P1 (A_S = 0.191 m^2; see Table 3.13) is 21.7% greater than the defoliated projected area for the same specimen (A_{p0} = 0.157 m^2). The projected area is lower due to some of the branches overlapping when the tree is projected onto a 2D image. Although only derived from one specimen, this relative difference can be used to estimate the defoliated projected areas for the other two specimens for which stem areas were measured: the alder and willow specimens A1 and S1, respectively. The values for A_{p0} are presented in Table 3.15 for the foliated and defoliated trees.

Table 3.15: Foliated and defoliated projected areas in still air for the *A. glutinosa* (A), *P. nigra* (P) and *S. alba* (S) Hydralab trees. A dash (-) indicates data not recorded.

Specimen	Foliated A_{p0} (m^2)	Defoliated A_{p0} (m^2)
A1	0.538	0.187 [a]
A2	0.723	-
A3	0.399	-
A4	0.414	-
A5	0.346	-
Average	0.484	0.187
P1	-	0.157
P2	0.701	-
P3	0.325	-
P4	0.684	-
Average	0.57	0.157
S1	0.522	0.461 [a]
S2	-	0.221
S3	0.978	-
S4	0.317	-
S5	1.153	-
S6	0.734	-
S7	0.52	-
S8	0.363	-
S9	0.601	-
S10	0.654	-
S11	0.343	-
S12	0.327	-
Average	0.592	0.341

[a] Projected area estimated from total one-sided stem area.

While it is informative to know the total projected area in still air, it is often important when modelling vegetation to know how the projected area is distributed over the trees' height so that non-submerged cases may also be modelled. In previous studies where the exact distribution is unknown, it has been assumed that this variation is linear (Järvelä 2004, Aberle and Järvelä 2013).

In this study, the exact distribution of the projected area over the trees' height H can be calculated directly. This is achieved by splitting the processed image of each tree into sub-images of equal height h and counting the number of tree pixels within each segment. In this case the images are split into 20 sections to provide projected areas at 5% increments of the total height. The resulting distributions are illustrated in Fig. 3.14 for each of the species.

As might be expected, the cumulative projected areas do not follow a linear trend with increasing percentage height due to the roughly oval profile of the trees. The lines of best fit shown in Figs. 3.14a–3.14c are based on a sigmoid function of the form:

$$f(x) = A + \frac{B - A}{1 + \exp\left[(x - C)/D\right]} \tag{3.2}$$

where A, B, C, and D are coefficients to be found via regression. The values for these regression coefficients, along with the coefficients of determination, are presented in Table 3.16 for each of the species.

Table 3.16: Species-specific regression parameters for the lines of best fit describing the cumulative vertical distribution of projected area for the foliated Hydralab trees.

Species	A	B	C	D	R^2
A. glutinosa	101.1	−12.4	32.7	15.6	0.933
P. nigra	101.2	−6.5	38.3	13.9	0.991
S. alba	100.3	−4.6	36.2	11.7	0.957

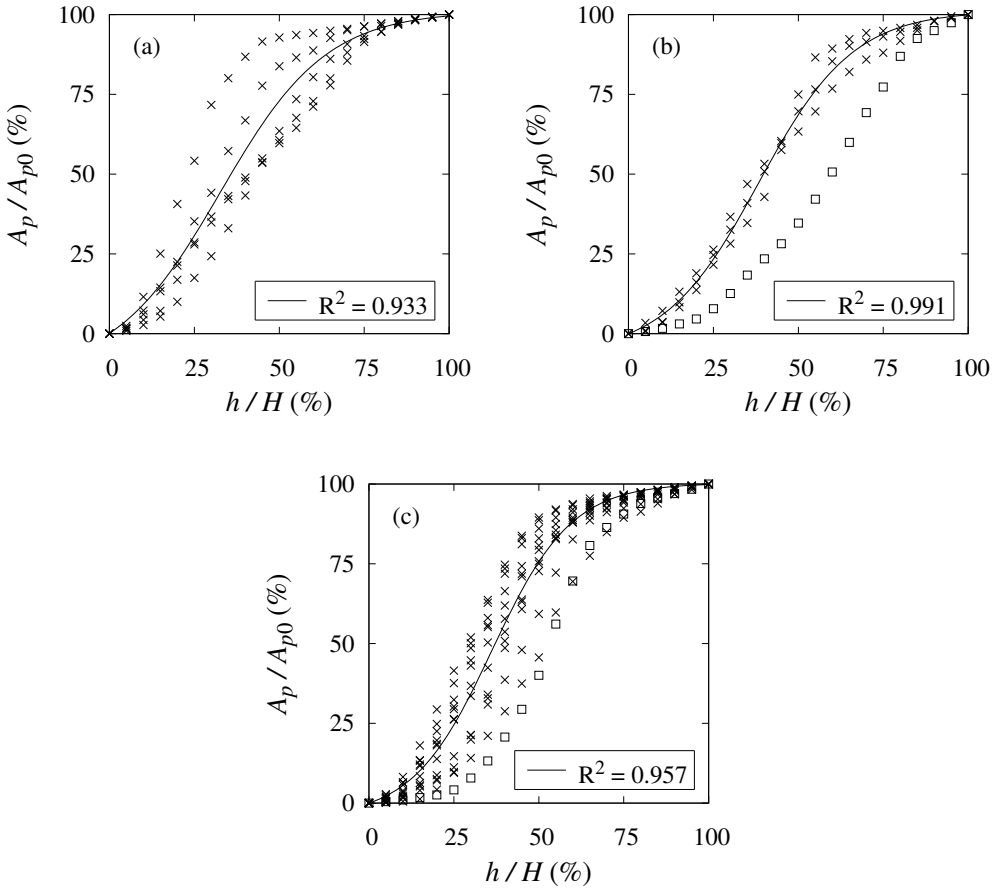

Figure 3.14: Cumulative vertical distribution of foliated projected area in still air for the: (a) *A. glutinosa*; (b) *P. nigra*; and (c) *S. alba* Hydralab trees. The defoliated specimens P1 and S2 are denoted using squares and are not included in the lines of best fit calculations.

3.4.2 Variation with Towing Velocity

In conjunction with the photographs of the Hydralab trees in still air, video footage of the trees during the drag force towing tests was also recorded. Underwater cameras were mounted to the towing carriage, such that one was positioned 3 m perpendicular to the specimens, while the other was attached 5 m ahead of the towing carriage (see Fig. 3.1). This provides side and front / rear facing footage of the trees under hydrodynamic loading at varying towing velocities.

In this section, the front- and rear-facing towing tank videos are analysed to obtain the variation in projected area with towing velocity. The procedure used here for processing the videos can be summarized as:

1. For each test run video, a frame is taken at the start of the run when the carriage is stationary and then further separate frames are taken at each tested velocity. The frames are only taken once the tree is observed to have finished reconfiguring due to the towing velocity increase.

2. The video frames are then cropped to a rectangle, enclosing only the tree as bounded by the water surface.

3. To reduce pixel noise caused by the low resolution and sensitivity of the underwater camera, an anisotropic bilateral filter is applied using G'MIC (v1.5.5).

4. High frequency 'contours' are then obtained by splitting the images into low and high frequencies based on a smoothness parameter, again using G'MIC.

5. The outline of the tree at each velocity is then determined by running an edge detection algorithm with a Sobel operator on the high frequency contours using GIMP (v2.8).

6. The resulting outlines are then converted to binary images based on a brightness threshold, again using GIMP.

7. An 'erode' and 'dilate' pass is next applied using G'MIC in order to fill any discontinuities in the tree's areas.

8. Finally, a particle analysis is performed using ImageJ (v1.47) and any regions not contiguous with the tree are removed.

The fully automated method described above produces binary (i.e. black and white) images where the black pixels represent the pixels occupied by the tree. As an example, the cropped raw and processed stills for each velocity from the footage for a single backwards-travelling run are presented in Fig. 3.15.

As opposed to the image analysis in the previous section, where the area per pixel could be determined, there was no object to provide dimensional scale in the video footage. Therefore, the sum of black (tree) pixels in each binary image is compared to the pixel sum for the still condition to provide the percentage reduction in projected area at each velocity. Combined with the initial projected area in still air A_{p0} (Table 3.15), the projected area A_p at each velocity can also be calculated.

It should be noted that during initial testing on the foliated willow specimen S1, it was observed that there was a variation of up to 2.66% in the measured drag force due to wake effects caused by the front-facing camera (Xavier 2009). Therefore, the camera was removed from its mounting in all other tests where the carriage travelled in a backwards direction. In this study, however, the front-facing footage for the S1 specimen is analysed regardless as the observed variation of up to 2.66% is deemed to be within acceptable limits.

The majority of the video footage obtained during the drag force towing tests at the CEHIPAR facilities was recorded from behind, i.e. the deformation of the rear 'face' of the tree was captured. Theoretically, two projections (separated by 180°) of a 3D object onto a 2D plane should provide identical areas. However, during video processing, it was noticed that some trees were deforming and deflecting to such a degree that their proximity to the camera was causing them to either be exaggerated in size or to move out of shot. Unfortunately the focal length of the underwater camera is not known and therefore no allowance can be made for the distortion effects caused by those trees that move particularly close to the camera. The following analysis focuses on those trees where the whole tree is visible and the camera-distance distortion is minimal.

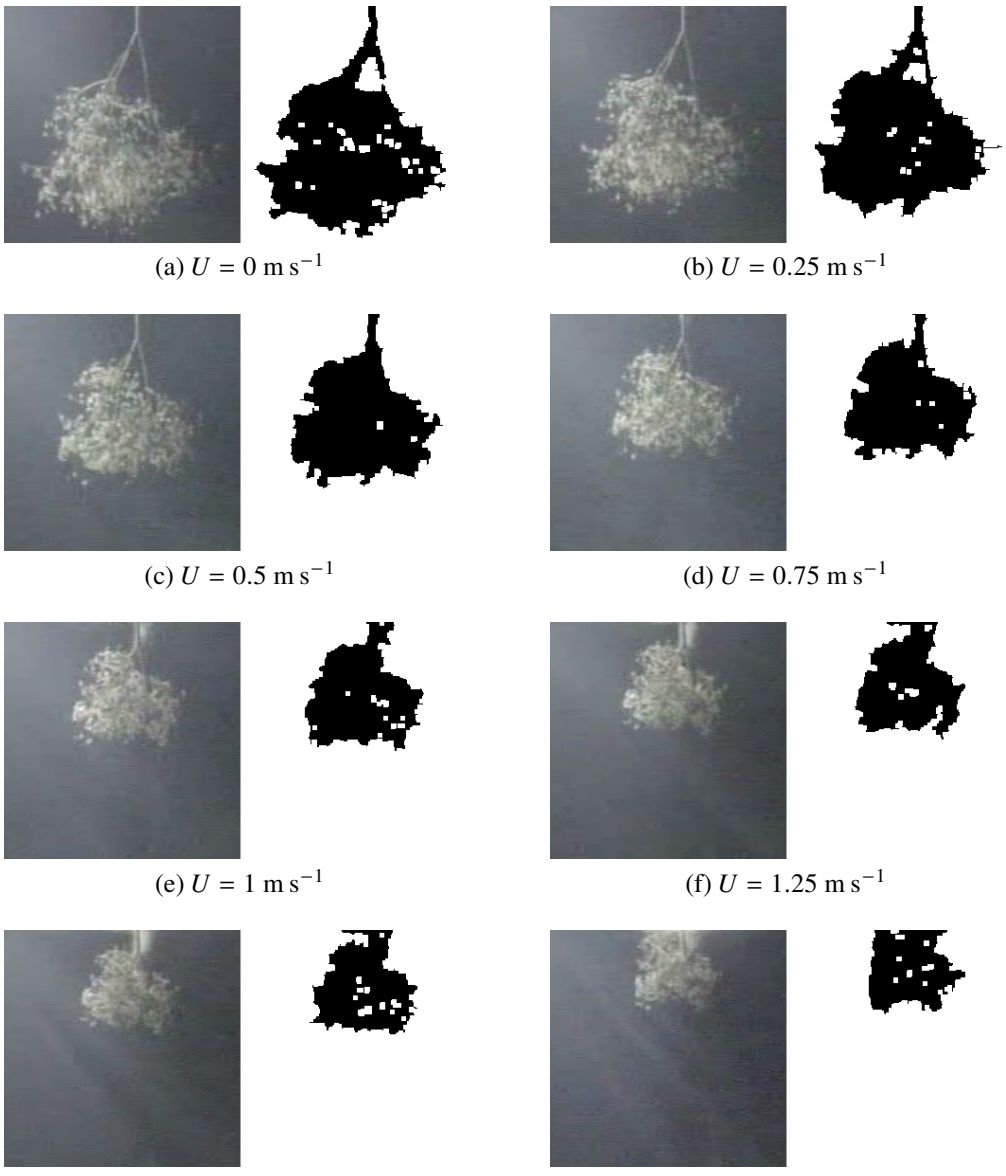

(a) $U = 0\ \mathrm{m\,s^{-1}}$ (b) $U = 0.25\ \mathrm{m\,s^{-1}}$

(c) $U = 0.5\ \mathrm{m\,s^{-1}}$ (d) $U = 0.75\ \mathrm{m\,s^{-1}}$

(e) $U = 1\ \mathrm{m\,s^{-1}}$ (f) $U = 1.25\ \mathrm{m\,s^{-1}}$

(g) $U = 1.5\ \mathrm{m\,s^{-1}}$ (h) $U = 1.75\ \mathrm{m\,s^{-1}}$

Figure 3.15: Raw and processed frames at each velocity for a single test run of the foliated willow tree S1. The camera was positioned in front of the tree as it was towed.

Foliated

Following the procedure detailed above, the variation in projected area with towing velocity is determined for the foliated trees. A number of artefacts in the video stills, such as patches of bright light from overhead windows, had to be removed manually. The resulting variations are presented in Fig. 3.16.

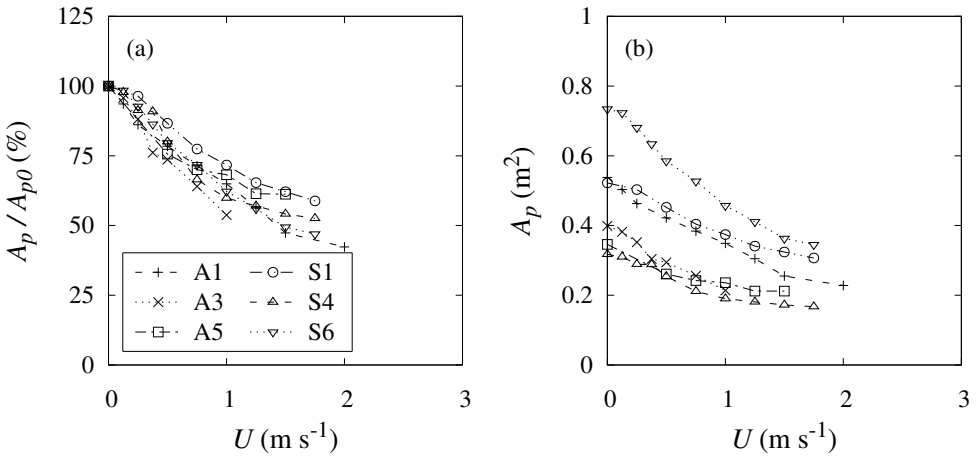

Figure 3.16: Variation in: (a) percentage; and (b) absolute projected area with velocity for the foliated Hydralab trees.

From inspection of Fig. 3.16, it appears that the trees' responses can be split into three regions based on the rate of reduction in the projected area. At the lowest velocities ($U < 0.25$ m s^{-1}), there is minimal reduction and the trees may be thought of as 'rigid'. As the velocity and thus drag force increases, the trees undergo significant reconfiguration and by $U = 1$ m s^{-1} the projected area is around 50% to 70% its original value. Above this velocity, the rate of reduction slows again as the majority of the trees' reconfiguration is complete, with the projected area only decreasing by around a further 20% from $U = 1$ m s^{-1} to $U = 2$ m s^{-1}.

To the author's knowledge, this is the first time that the variation in projected area with flow velocity has been determined for fully submerged full-scale trees. However, Vollsinger *et al.* (2005) were able to determine such variation for full-scale trees in a wind tunnel. The authors tested foliated trees of *Populus trichocarpa* (black cottonwood), *Alnus rubra* (red alder) and *Betula papyrifera*

(paper birch) for velocities of 4 m s^{-1} to 20 m s^{-1} and recorded the projected area at each velocity. A similar 'three region' pattern to that shown in Fig. 3.16 was observed for the alder and cottonwood trees, with minimal reduction in A_p for $U < 5$ m s^{-1}, a rapid reduction in A_p for $5 < U < 12$ m s^{-1}, and then a less rapid reduction in A_p for $U > 12$ m s^{-1}. However, by a wind velocity of $U = 20$ m s^{-1} the trees had reached a greater level of reconfiguration (20% to 38%) than those tested in this thesis (Fig. 3.16). It is also interesting to note that the projected area for the paper birch trees decreased rapidly, even at the lowest velocity tested, perhaps suggesting that the birch trees were more flexible.

The variation in A_p with towing velocity was also measured by Västilä *et al.* (2013) for stands of foliated *Populus nigra* (black poplar) branches. The branches were tested in fully submerged conditions at velocities of 0.1 m s^{-1} to 0.61 m s^{-1}. Although the velocities are much lower than those tested for the Hydralab trees in this thesis, the variation follows a similar pattern to that in Fig. 3.16 due to the branches being more flexible.

Defoliated

The analysis of the video footage for the defoliated trees posed a greater challenge, as the poor resolution (340×570 pixels) and contrast of the video made it difficult to detect the edges of the trees using the algorithm described above. Therefore, the outlines for those trees where the defoliated projected area is known (P1 and S2) or can be estimated (A1 and S1; see Table 3.15) were manually traced using image processing software. Other trees were not processed in this manner due to time constraints. The resulting variations in projected area with towing velocity for the aforementioned defoliated trees are presented in Fig. 3.17.

It can be seen from Fig. 3.17 that the general trend in the reduction in projected area can be characterized in a similar manner to the three regions discussed for the foliated trees (Fig. 3.16). The poplar specimen P1, however, exhibits slightly different behaviour in that it remains less deformed at lower velocities and only starts to significantly reduce in projected area at $U \approx 0.5$ m s^{-1}. It also deforms less overall, with the magnitude of the reduction in projected area at each velocity being lower than the other defoliated trees. This is most likely due to the specimen

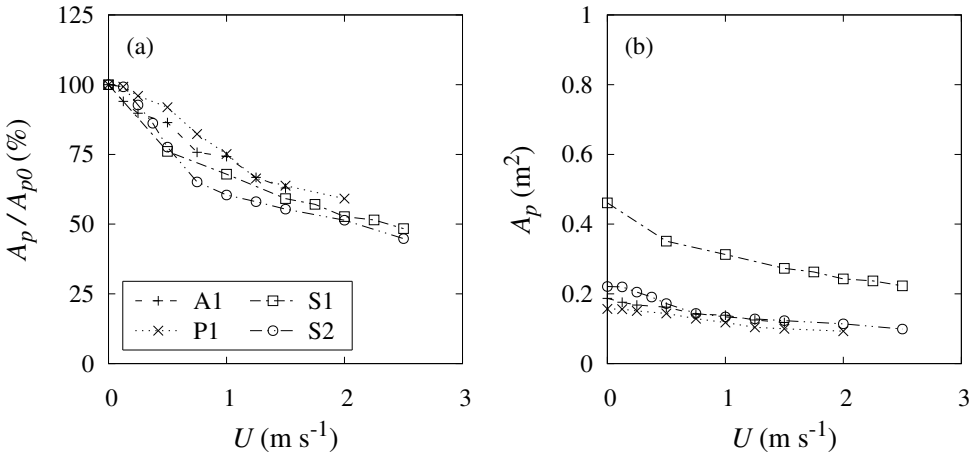

Figure 3.17: Variation in: (a) percentage; and (b) absolute projected area with velocity for the defoliated Hydralab trees.

being stiffer and more resistant to deformation, as seen in the higher flexural rigidity values recorded for the poplar trees compared to the alder and willow trees (see Table 3.3).

Impact of Foliage

The impact of foliage on the reconfiguration of the trees can be examined by comparing the rate of reduction in the projected area for the two trees for which there is both foliated and defoliated data (A1 and S1). The foliated and defoliated variations are presented simultaneously in Fig. 3.18.

It can be seen from Fig. 3.18 that, for the alder specimen A1, the rate of reduction in projected area with towing velocity is greater when it is foliated. This is to be expected since the foliage will increase in total drag force at a given velocity (see Fig. 3.8) and thus cause greater reconfiguration.

In the case of the willow specimen S1, however, the rate of reduction in projected area appears to be more similar between the foliated and defoliated states. This may seem contradictory, but is most likely due to the fact that the S1 specimen was tested during the early stages of the Hydralab experimental study and was thus not as foliated. This can be quantified by calculating the leaf to wood volume ratio V_L/V_S for the two specimens (see Tables A.1 and A.2 for V_S

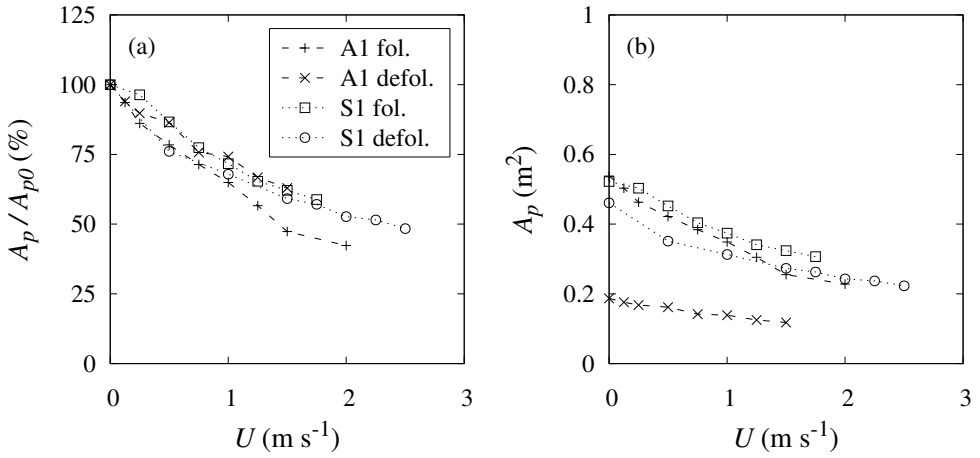

Figure 3.18: Impact of foliage on the variation in: (a) percentage; and (b) absolute projected area with velocity for the available Hydralab trees.

and V_L, respectively). For the alder specimen A1 this ratio is 15.9%, while for the willow specimen S1 it is just 4.4%, thus confirming that it had a substantially lower level of foliation.

It is also interesting to note that, for both foliage states, the rate of reduction in projected area with towing velocity is greater for the alder specimen A1 (Fig. 3.18). This suggests that it is more flexible and prone to deformation than the willow specimen S1. Although bending stiffness data is not available for the S1 specimen, the flexural rigidity value for the A1 specimen is indeed roughly two-thirds the willows' overall average (Table 3.3).

3.5 Drag Coefficient Analysis

In this section, the drag force measurements (§ 3.2.1) and previously derived projected areas (§ 3.4.2) for the Hydralab trees are combined in order to determine the variation in drag coefficient with towing velocity. The drag coefficients are calculated at each velocity using Eq. (2.3).

3.5.1 Foliated

The resulting drag coefficients for the foliated trees are presented in Fig. 3.19. It can be seen that, for all specimens, the drag coefficient rapidly decreases from an initial value of $C_d \approx 1$ for $U < 1\ \mathrm{m\,s^{-1}}$. Above this 'threshold' velocity the drag coefficient is relatively constant and ranges from 0.33 to 0.54, depending on the specimen. This is consistent with the observed pattern for the foliated trees' reduction in projected area, where the majority of the trees' reconfiguration was complete by $U \approx 1\ \mathrm{m\,s^{-1}}$ (Fig. 3.16).

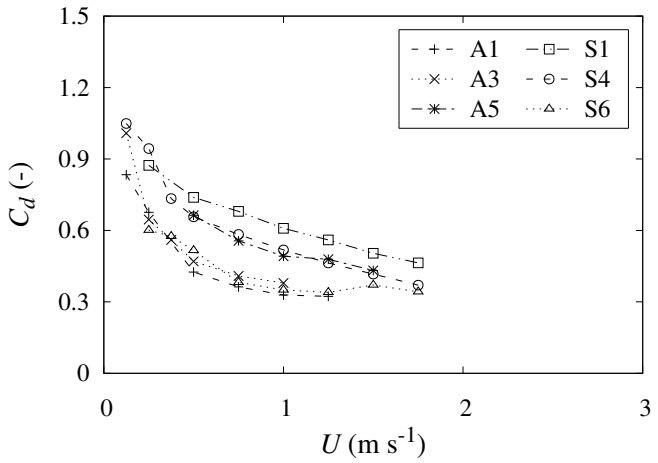

Figure 3.19: Variation in drag coefficient with towing velocity for the foliated Hydralab trees.

The general pattern shown in Fig. 3.19 is also similar to that found by Vollsinger *et al.* (2005) for *Populus trichocarpa* (black cottonwood), *Alnus rubra* (red alder) and *Betula papyrifera* (paper birch) trees in a wind tunnel. However, while the drag coefficients in that study did decrease from their initial value of around unity, they only reduced to around 0.5 to 0.7 before becoming relatively constant with velocity. This is most likely due to the fact that the projected areas for the trees in the present study were found to reduce by a maximum of 45% to 70%, as opposed to around 60% to 80% for those trees tested by Vollsinger *et al.* (2005).

3.5.2 Defoliated

The drag coefficients for the defoliated Hydralab trees, calculated using the previously derived variations in projected area with towing velocity (Fig. 3.17), are plot in Fig. 3.20.

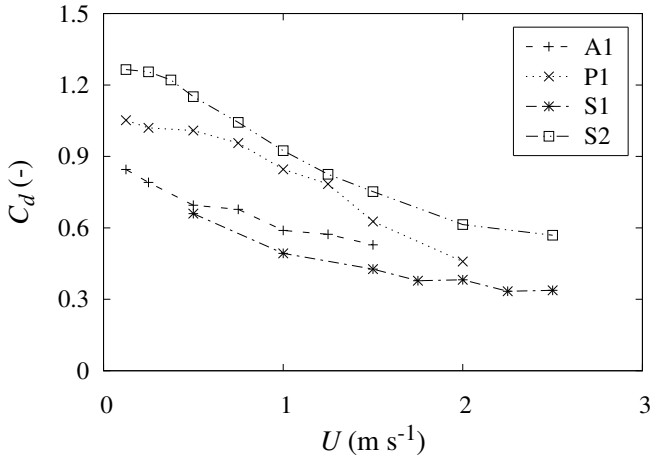

Figure 3.20: Variation in drag coefficient with towing velocity for the defoliated Hydralab trees.

For the specimens P1 and S2, the drag coefficient is relatively constant for $U < 0.3$ m s^{-1} (Fig. 3.20), suggesting that they could perhaps be characterized as a collection of rigid cylinders at such velocities. This agrees with the minimal reconfiguration seen at low velocities for these trees (Fig. 3.17). For all specimens, however, a general trend of gradually decreasing drag coefficients is observed.

It is interesting to note that the drag coefficients for the A1 and S1 specimens are somewhat less than those for the P1 and S2 specimens. This indicates that the factor used previously to estimate the defoliated projected area from the one-sided stem area for the A1 and S1 specimens (see Table 3.15) may have been too high. Unfortunately, there is no further data available to refine the factor in this study.

3.5.3 Impact of foliage

The impact of foliage on the trees' drag coefficients can be investigated by comparing the results for those trees for which there is both foliated and defoliated

data (A1 and S1). The foliated and defoliated drag coefficients are presented simultaneously in Fig. 3.21.

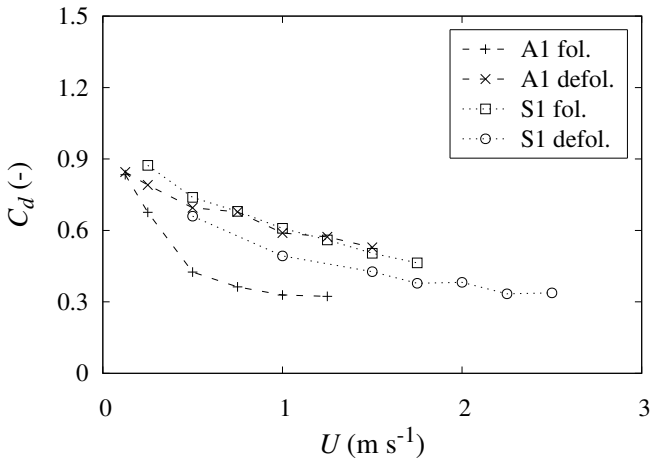

Figure 3.21: Impact of foliage on the variation in drag coefficient with towing velocity for the available Hydralab trees.

From Fig. 3.21 it can be seen that, for the alder specimen A1, the magnitude of the drag coefficient is less when the specimen is in a foliated state. On-the-other-hand, the opposite is true for the willow specimen S1. However, as previously discussed for Fig. 3.20, the factor used to estimate the defoliated projected area A_{p0} from the one-sided stem area for the A1 and S1 specimens (see Table 3.15) may have been too high.

If that is the case, then the actual defoliated areas in still air would be lower than those used here and thus the drag coefficients for these defoliated specimens would be correspondingly greater. This would then mean that both the A1 and S1 specimens would have a lower drag coefficient when foliated, as opposed to when defoliated. In drag force tests on foliated and defoliated branches of *Salix viminalis* (osier), *Salix alba* (white willow) and *Salix purpurea* (purple willow), Wunder *et al.* (2011) also found that the drag coefficients were greater when the branches were defoliated.

3.6 Summary

In this chapter, high-resolution force-velocity data from two previous experimental studies involving branches and full-scale trees were analysed to quantify the effect of reconfiguration on the force-velocity relationship for flexible vegetation (see Figs. 3.9 and 3.10). It was found that this reconfiguration significantly reduced the drag force exerted on the vegetation. Indeed, instead of following a quadratic force-velocity response, the specimens exhibited an almost linear force-velocity relationship, with Vogel exponents ranging from -0.46 to -1.05 (see Tables 3.5–3.7 and 3.9). However, no correlation was found between the specimens' Vogel exponents and any of the measured physical properties. The testing of foliated and defoliated trees also showed that the foliage was responsible for a significant proportion (40% to 75%) of the total drag force (see Fig. 3.8).

In addition to the force-velocity and physical property measurements reported from the previous experimental studies, photographs and scanned images of the trees were analysed using computer software to obtain the total one-sided leaf and stem areas and the projected areas in still air (see Tables 3.12, 3.13 and 3.15, respectively). Reference objects of known area in the images allowed these values to be determined with good accuracy. It was found that the distribution of the trees' projected area over their height did not follow a linear relationship, as has been assumed in previous experimental studies, but rather followed a sigmoid shape curve.

Video footage of the trees during drag force testing, obtained from underwater cameras, was also presented and analysed using a series of image processing algorithms. Combined with the projected area in still air, the video analysis allowed the variation in projected area with towing velocity to be explicitly calculated for a number of the trees (see Figs. 3.16 and 3.17). In all cases, the projected area was found to decrease with velocity as the trees reconfigured in the flow. However, the difficulty in this study of estimating the error in the video analyses highlights the need for the precise consideration of camera angle, position, and focal length when designing experimental procedures to capture the variation in projected area for flexible vegetation.

The variation in projected area with velocity enabled the drag coefficient

to be directly computed for the available trees (see Figs. 3.19 and 3.20). This showed that the foliated trees typically had a greater drag coefficient than the defoliated trees, for a given velocity. The reduction in drag coefficient with velocity for the foliated trees was initially rapid, before reaching a somewhat constant value at higher velocities. For the defoliated trees, the reduction in drag coefficient was approximately linear with velocity. Empirical relationships were not proposed for the drag coefficient, since any such relationships would also require the variation in projected area to be known in order to predict the drag force and would, therefore, not be of general modelling interest.

Chapter 4

Drag Force Models for Flexible Vegetation

4.1 Introduction

In this chapter, two drag force models for flexible riparian trees are proposed. The first is empirical and aims to provide a simple, yet effective, means of predicting the vegetation's drag coefficient based on the vegetation's projected area in still air. The second is a theoretical model derived from dimensional consideration that directly incorporates the effects of the vegetation's flexibility.

For both models, the relevant species-specific parameters are derived from the data collected for the Hydralab trees. The models are then validated using the Hydralab data, before being applied to the independent LWI branch-scale data set. For the second model, a sensitivity analysis is carried out for the model's coefficients and the results are also compared to two existing drag force approaches.

4.2 Drag Coefficient Model

Knowing the variation in projected area (and thus drag coefficient) with velocity is interesting from a theoretical point of view; however, it has limited scope in current modelling techniques since it is impractical to determine such relationships

for every type of vegetation that may be required at each site under modelling consideration. Therefore, a more practical solution is suggested here, whereby only the projected area in still air is required. This metric can be determined on-site via non-destructive photo-analysis methods.

4.2.1 Theory

In previous studies involving drag force measurements for full-scale trees in wind tunnels (e.g. Vollsinger *et al.* 2005, Koizumi *et al.* 2010) and branches in flumes (e.g. Wunder *et al.* 2011, Dittrich *et al.* 2012, Västilä *et al.* 2013), a 'rigid' drag coefficient is often calculated using the projected area in still air, rather than the projected area at each velocity:

$$C_d^* = \frac{2F}{\rho A_{p0} U^2} \tag{4.1}$$

where F is the drag force; ρ is the fluid density; U is the flow velocity; and A_{p0} is the projected area in still air for a particular specimen (see Table. 3.15). Since the projected area in still air is constant, the 'rigid' drag coefficient C_d^* will also incorporate any reduction in the projected area A_p due to the specimen reconfiguring (see Figs. 3.16 and 3.17).

When deriving empirical relationships for the drag coefficient of rigid objects, such as cylinders, it has been common to normalize the flow velocity using the dimensionless Reynolds number Re (see Fig. 2.3). In this study, the Reynolds number is defined so that the projected area in still air is used as the characteristic length scale:

$$Re = \frac{U A_{p0}^{1/2}}{\nu} \tag{4.2}$$

where ν is the kinematic viscosity of the fluid; U is the flow velocity; and A_{p0} is the projected area in still air.

The use of the projected area in still air as the characteristic length scale differs from the typical Reynolds number definition for vegetation, where either the flow depth or stem diameter are utilized (e.g. Shames 2003). However, it is proposed here since the flow depth or stem diameter provide little information on the portion of the plant or tree that the flow is acting on. Further, the use of

the projected area in still air minimizes the number of model parameters as it is already required to calculate the rigid drag coefficient.

The variation in rigid drag coefficient with Reynolds number is plot in Fig. 4.1 for the foliated and defoliated Hydralab trees.

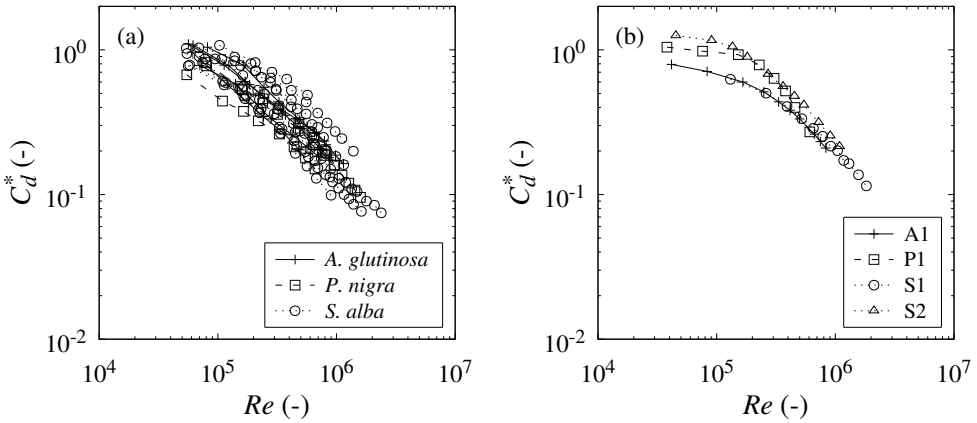

Figure 4.1: Variation in rigid drag coefficient with Reynolds number for the: (a) foliated; and (b) defoliated Hydralab trees. The projected area in still air was used as the characteristic length scale when calculating the Reynolds number.

It can be seen that the foliated alder and poplar specimens collapse onto almost a single line for their respective species, implying that the current definition of the Reynolds number is a useful metric. However, the willow specimens are not quite as tightly grouped and there appears to be less of a singular relationship between the rigid drag coefficient and the Reynolds number.

Although there are a limited number of trees for which the defoliated projected area in still air is available, it can be seen that they mostly collapse onto a single curve (Fig. 4.1). However, as previously discussed (§ 3.4.2), the projected areas in still air for the specimens A1 and S1 may have been slightly overestimated from their one-sided stem areas. If the initial projected areas for these trees were reduced, the rigid drag coefficient would increase while the Reynolds number would decrease, for a given velocity. This would then move the curves for the specimens A1 and S1 closer to those for the specimens where the defoliated projected area was directly measured (P1 and S2).

For an empirical model, the curves in Fig. 4.1 suggest that a power-law relationship between the rigid drag coefficient and Reynolds number would be appropriate. However, negative-power laws are unbounded at the lower end (i.e. asymptotic with the y axis), which would result in non-physical drag coefficients at low velocities. The use of an exponential law would remedy this problem, since they are bounded at the lower end, although they tend to decay much faster than power-law relationships.

A possible solution would be to combine the two relationships; however, the exponential law can be approximated with a constant value at lower Reynolds numbers, thus reducing the complexity of any empirical relationship. Therefore, the following piecewise model is proposed:

$$C_d^* = \begin{cases} C_{d0}^* & : \quad Re \leq Re_t \\ \alpha Re^p & : \quad Re > Re_t \end{cases} \tag{4.3}$$

where Re_t is a threshold Reynolds number; C_{d0}^* is a constant value, equal to the initial value for C_d^*; α is a power-law coefficient; and p is a power to be found through regression analysis.

The model assumes that the rigid drag coefficient does not increase dramatically at low Reynolds numbers due to viscous skin friction (see Fig. 2.3 for $Re < 100$), since these effects would not be of practical interest when modelling floodplain vegetation where the Reynolds numbers are typically much greater.

4.2.2 Results and Discussion

Calibration

In order to find values for Re_t, C_{d0}^*, α and p for each of the three Hydralab species, a regression analysis was applied in an iterative fashion. At each iteration the threshold Reynolds number Re_t was increased, up to an arbitrary limit of $Re = 3 \times 10^5$, determined from visual inspection of Fig. 4.1. Once complete, the parameters from the regression analysis with the greatest coefficient of determination R^2 were selected (see Table 4.1).

From Table 4.1, it can be seen that the threshold area Reynolds number Re_t is similar across the three species and corresponds to a velocity of roughly

Table 4.1: Regression parameters for the proposed model (Eq. 4.3) describing the variation in rigid drag coefficient with Reynolds number for the Hydralab trees. The number of data points N used in each regression analysis is also given.

Species	C^*_{d0}	Re_t	α	p	R^2	N
A. glutinosa	0.994	9×10^4	1.64×10^3	−0.661	0.923	39
A. glutinosa (defol.)	0.752	9×10^4	9.03×10^2	−0.605	0.981	10
P. nigra	0.756	9×10^4	2.94×10^2	−0.54	0.916	28
P. nigra (defol.)	0.984	1.6×10^5	1.61×10^5	−0.989	0.982	8
S. alba	0.891	1×10^5	2×10^3	−0.671	0.819	101
S. alba (defol.)	1.255	8×10^4	2.19×10^3	−0.66	0.926	23

$0.2\ \mathrm{m\,s^{-1}}$. This agrees with the velocity at which the trees were observed to begin reconfiguring significantly (see Figs. 3.16 and 3.17).

Excluding the defoliated poplar trees, for which only one specimen was available, the power p to which the Reynolds number is raised in Eq. (4.3) is also fairly consistent, only ranging between -0.54 and -0.67. However, the value for α varies quite significantly between the species, with there being an order of magnitude difference between the poplar trees and the other two species. The sample size for the poplar trees is smaller than that for the alder and willow trees, so it is hard to conclude whether the discrepancy is due to physical processes, differences in species' homogeneity, or sample size.

The relationships none-the-less capture the main variation in rigid drag coefficient, with the coefficient of determination ranging from 0.819 to 0.923. The resulting relationship for the foliated willow trees is illustrated in Fig. 4.2.

Although the power law described in Eq. (4.3) is asymptotic with the x axis (i.e. $C^*_d > 0$), it is expected that the rigid drag coefficient becomes independent of the Reynolds number for $Re \gg 1 \times 10^6$, similar to the effect for isolated cylinders (Douglas *et al.* 2005). However, this is not incorporated into the current model since it is unlikely that riparian flood flows under modelling consideration will achieve such high Reynolds numbers ($U_{\max} = 4\ \mathrm{m\,s^{-1}}$ for the foliated trees tested in this study).

The model defined above in Eq. (4.3) for the rigid drag coefficient can now be used to predict the variation in drag force. The species-specific regression parameters from Table 4.1 are used to determine the rigid drag coefficient C^*_d,

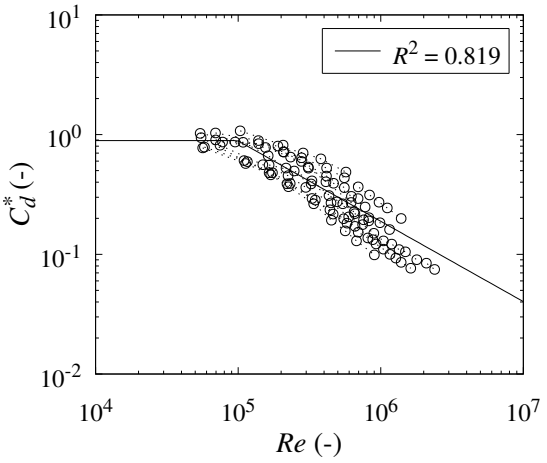

Figure 4.2: Proposed model (Eq. 4.3) for the variation in rigid drag coefficient with Reynolds number for the foliated willow Hydralab trees. The projected area in still air was used as the characteristic length scale when calculating the Reynolds number.

which is then substituted into Eq. (4.1), along with the towing velocity U and projected area in still air A_{p0}, to provide the drag force. The resulting drag force predictions are plot against the measured drag forces in Fig. 4.3 for the foliated and defoliated Hydralab trees.

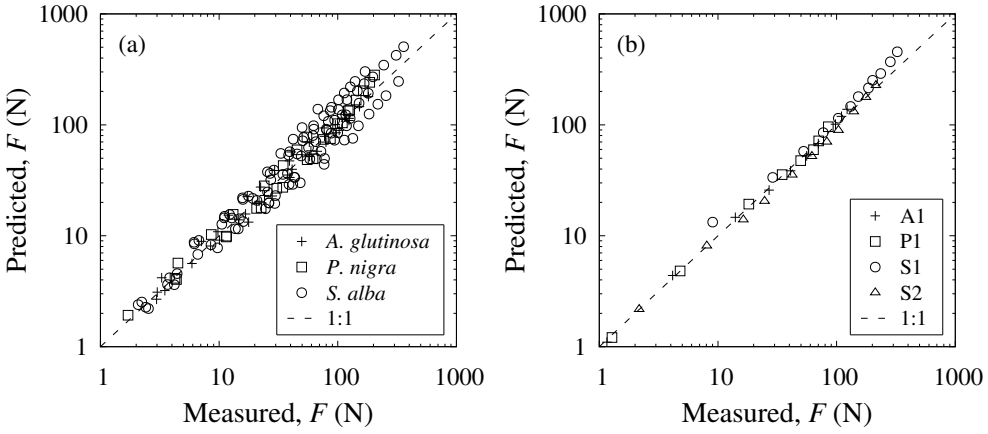

Figure 4.3: Drag force as predicted using the rigid drag coefficient model (Eqs. 4.1 and 4.3) for the: (a) foliated; and (b) defoliated Hydralab trees.

As can be seen from Fig. 4.3, the drag force predictions are in good agreement with the measured values, even over the broad range of towing velocities tested in this study ($0.125 \leq U \leq 6\ \mathrm{m\,s^{-1}}$). The average errors $\epsilon_{\%}$ between the predicted and measured drag forces are presented in Table 4.2.

Table 4.2: Average percentage errors $\epsilon_{\%}$ for predictions of the foliated and defoliated Hydralab trees' drag forces based on the rigid drag coefficient model (Eqs. 4.1 and 4.3). The number of data points N used to calculate the average errors is also given.

	Foliated		Defoliated	
Species	$\epsilon_{\%}$	N	$\epsilon_{\%}$	N
A. glutinosa	13.2	39	6	10
P. nigra	17.1	28	5	8
S. alba	29.8	101	15.9	23

The low average errors reported in Table 4.2 indicate that the model approach is valid and that using species-specific values is applicable. The rigid drag coefficient model (Eqs. 4.1 and 4.3) also represents an order of magnitude improvement over a traditional constant C_d approach, where the drag force predictions would be many times greater than the expected drag force at higher velocities.

Application

Now that the rigid drag coefficient model has been shown to be effective at predicting the drag force for the Hydralab trees, it is applied to the independent, branch-scale data set from the LWI experiments (§ 3.2.2). For each force-velocity point, the rigid drag coefficient is first calculated using Eqs. (4.2) and (4.3), with the values for C^*_{d0}, Re_t, α, and p taken from the foliated *P. nigra* and *S. alba* values in Table 4.1. The A_{p0} values are taken from Table 3.4. The resulting drag forces, calculated by substituting the rigid drag coefficient back into Eq. (4.1), for the partially and fully submerged willow and poplar branches are presented in Fig. 4.4.

From Fig. 4.4 it can be seen that, although the drag coefficient model's drag force predictions are in relatively good agreement with the measured values at the lowest velocities, the model quickly begins to overestimate the drag force by

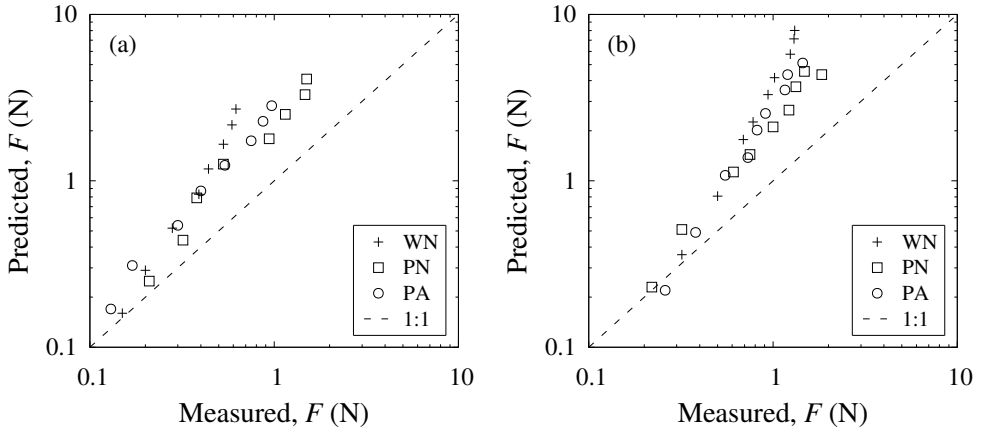

Figure 4.4: Drag force as predicted using the rigid drag coefficient model (Eqs. 4.1 and 4.3) for the: (a) partially; and (b) fully submerged LWI branches.

relatively wide margin for $U \gtrsim 0.25$. This is reflected in the high average errors reported in Table 4.3.

Table 4.3: Average percentage errors $\epsilon_{\%}$ for predictions of the partially and fully submerged LWI branches' drag forces based on the rigid drag coefficient model (Eqs. 4.1 and 4.3). The number of data points N used to calculate the average errors is also given.

	Partial sub.		Fully sub.	
Specimen	$\epsilon_{\%}$	N	$\epsilon_{\%}$	N
WN	155	8	256	9
PN	101	8	110	9
PA	116	8	142	9

For both the partially and fully submerged conditions, the predicted drag forces are on average more than double the measured values (Table 4.3). The reason for this overestimation is that the Reynolds numbers stay below the threshold Re_t, due to the much lower A_{p0} values for the branches compared to the Hydralab trees from which Re_t was derived (Table 4.1). As a consequence, the rigid drag coefficient C_d^* is held at its initial value C_{d0}^* and does not decrease with velocity, thereby replicating a quadratic force-velocity response. This therefore implies that the current model (Eq. 4.3) is not scale independent.

4.3 Cauchy Reconfiguration Model

The drag coefficient model proposed in the previous section was derived from empirical observations. While it was shown to be accurate when properly calibrated, significant errors were observed when attempting to apply it to vegetation of a different scale and level of submergence. In this section, therefore, a drag force model is developed from theoretical principles, based on the drag force observations and analyses in the previous chapter (see sections § 3.3–§ 3.5).

4.3.1 Theory

In order to parameterize the complex flow-body interactions experienced by flexible vegetation, it is assumed that the drag force F is dependent on the velocity U, density ρ and kinematic viscosity ν of the fluid, along with the vegetation's projected area A_p and modulus of elasticity E. According to the Π theorem of Buckingham (1914), this system can be described by three dimensionless numbers. Here, we choose the drag coefficient, Reynolds number and the Cauchy number:

$$C_d = \frac{2F}{\rho A_p U^2}; \qquad Re = \frac{A_p^{1/2} U}{\nu}; \qquad Ca = \frac{\rho U^2}{E} \tag{4.4}$$

This implies that the drag coefficient is dependent on both the Reynolds number and the Cauchy number. For a fully stiff object, the Cauchy number will be less than unity and therefore there will be no deformation under loading (Blevins 1990, Cermak and Isyumov 1998, Chakrabarti 2002). This leads to the well known observation that for rigid objects, such as plates and cylinders, the drag coefficient is a function of the Reynolds number only. Further, for flows where the Reynolds number effect is essentially constant, the above set of parameters form the classical drag equation (2.2).

The Cauchy number defined above, however, does not take into account the cross-sectional area or 'slenderness' of an object and, as such, cannot accurately represent the compressibility of vegetation (de Langre 2008). Therefore, the Cauchy number is re-defined to incorporate the flexural rigidity EI:

$$Ca = \frac{\rho U^2 A_{p0} H^2}{EI} \tag{4.5}$$

where I is the second moment of area of the main stem; A_{p0} is the projected area in still air; and H is the vegetation's height.

The definition of the 'vegetative' Cauchy number used here (Eq. 4.5), differs slightly from that used previously by Luhar and Nepf (2011) and Whittaker *et al.* (2013) (see Eqs. 2.8 and 2.9, respectively). In this study, the use of $A_{p0}H^2$ as opposed to the product of the breadth and length (bl^3) used by Luhar and Nepf (2011) is favoured since A_{p0} more accurately describes the vegetation's flow-interacting area when considering vegetation with complex morphology. In the case of idealized slender beams, $A_{p0}H^2$ and bl^3 are equivalent. With respect to the Cauchy number utilized in Whittaker *et al.* (2013), the volume term is replaced by the projected area, which may be easier to measure *in situ* using non-destructive methods.

In drag force studies on flexible plates and fibres, Gosselin *et al.* (2010) and Gosselin and de Langre (2011) also described the reconfiguration in terms of the Cauchy number. The authors define a separate reconfiguration number $\mathcal{R}$ that compares the measured drag force to that of an equivalent rigid object with the same geometry:

$$\mathcal{R} = \frac{2F}{\rho C^*_{d0} A_{p0} U^2} \tag{4.6}$$

where C^*_{d0} is the drag coefficient of the rigid object (see Eq. 4.1).

If buoyancy and Reynolds number effects are assumed to be negligible, it follows from the dimensional analysis in Eq. (4.4) that the reconfiguration number is a function of the Cauchy number, i.e. $\mathcal{R} = f(Ca)$ (Gosselin *et al.* 2010, Gosselin and de Langre 2011, de Langre *et al.* 2012, Barois and de Langre 2013). In order to test this relationship, the variation in reconfiguration number with Cauchy number is plot in Fig. 4.5 for the foliated and defoliated Hydralab trees. The previously calculated initial rigid drag coefficients C^*_{d0} (see § 4.2.2) are used for the values of the rigid drag coefficient in Eq. (4.6).

From Fig. 4.5 it can be seen that the variation follows the expected behaviour, i.e. that the drag force exerted on the trees only deviates away from the rigid approximation once they begin to reconfigure ($Ca > 1$). This thus suggests that the parameterization of the 'vegetative' Cauchy number in Eq. (4.5) is valid. The results for the case where the mid-stem flexural stiffness EI_{50} values are utilized

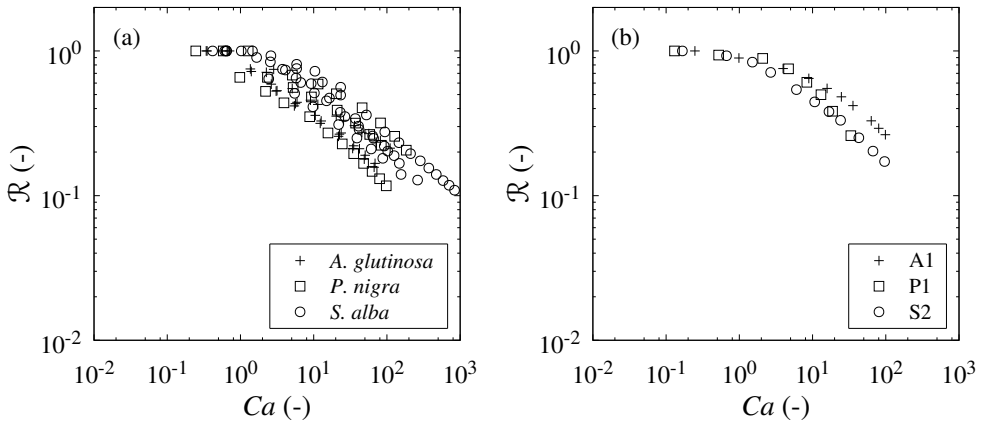

Figure 4.5: Variation in reconfiguration number with the Cauchy number for the: (a) foliated; and (b) defoliated Hydralab trees. The value of EI_{25} was used for the flexural rigidity term in the Cauchy number calculation.

are very similar and are therefore not included here.

Assuming that the density of the fluid is constant, the deviation of the reconfiguration number $\mathcal{R}$ away from unity with increasing velocity (Fig. 4.5) must be caused solely by the change in the characteristic drag coefficient term in Eq. (2.2). Indeed, in the previous chapter (§ 3.3.2) it was shown that the characteristic drag coefficient for flexible trees and branches decreases rapidly with velocity, following a roughly inverse power law (see Figs. 3.9 and 3.10).

Considering that $\mathcal{R} = f(Ca)$, it follows that the characteristic drag coefficient is a function of the Cauchy number, i.e. $C_d A_p = f(Ca)$ (de Langre 2008). Furthermore, assuming that the relationship between $\mathcal{R}$ and Ca follows a power law, it can be found that the power to which the Cauchy number is raised is equivalent to half the Vogel exponent ($\psi/2$). The variation in the characteristic drag coefficient with velocity can therefore be described by the following:

$$C_d A_p = C^*_{d0} A_{p0} Ca^{\psi/2} \tag{4.7}$$

where C^*_{d0} is taken to be species-specific, similarly to $C_{d\chi}$ in Eq. (2.6). The Vogel exponent is also thought to be species-specific (Järvelä 2004, Aberle and Dittrich 2012, Aberle and Järvelä 2013).

Physically, Eq. (4.7) represents the magnitude (Ca) and rate (ψ) of the recon-

figuration that flexible objects experience in fluid flows, through the reduction in the characteristic drag coefficient from its initial 'rigid' value ($C^*_{d0}A_{p0}$) with increasing velocity. It is also applicable to rigid bodies, since when $\psi = 0$ there will be no variation in the characteristic drag coefficient, assuming independence of Reynolds number effects.

It should be noted that, since a Cauchy number of less than unity indicates that there is no deformation or reconfiguration by definition (Blevins 1990, Cermak and Isyumov 1998, Chakrabarti 2002), a limiter must be placed on the Cauchy number in Eq. (4.7), i.e. $Ca = \max(1, Ca)$. This prevents the characteristic drag coefficient deviating away from its initial rigid value of $C^*_{d0}A_{p0}$ when the drag force exerted on an object is not great enough to overcome the object's bending resistance and cause reconfiguration.

To illustrate the relationship defined in this model between the characteristic drag coefficient and the Cauchy number (Eq. 4.7), the variation in characteristic drag coefficient with velocity is plot schematically in Fig. 4.6.

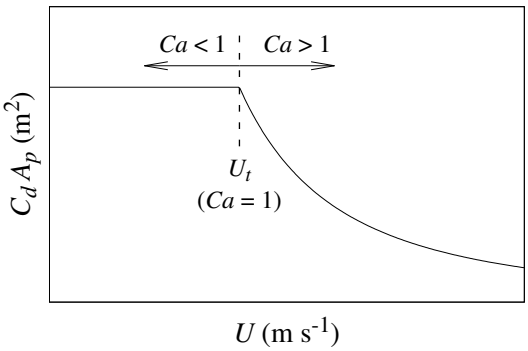

Figure 4.6: Proposed variation in characteristic drag coefficient with velocity (Eq. 4.7) for a flexible object (i.e. assuming that $\psi < 0$).

Replacing the drag coefficient and projected area terms in the classical drag equation (2.2) with the relationship defined above (Eq. 4.7), we thus arrive at the new 'Cauchy reconfiguration model' for predicting the hydrodynamic drag force exerted on flexible vegetation:

$$F = \frac{1}{2}\rho C^*_{d0}A_{p0}Ca^{\psi/2}U^2 \tag{4.8}$$

4.3.2 Results and Discussion

Now that the theoretical model has been developed, it can be applied to both the Hydralab and independent LWI data sets.

Validation

In order to validate the model's approach, it is first used to predict the drag forces of the trees from the Hydralab experiments. The physical properties that Eq. (4.8) requires, namely the height H, main-stem flexural rigidity EI, and projected area in still air A_{p0}, are taken from Tables 3.2, 3.3, and 3.15, respectively. In addition to the trees' physical properties, the model also requires two species-specific coefficients: the rigid drag coefficient C^*_{d0} (Table 4.1) and the Vogel exponent ψ (Table 3.8).

During the experimental procedure at the CEHIPAR facilities, two values were obtained for the main-stem flexural rigidity of each tree (see § 3.2.1). For this validation, both the first quartile EI_{25} and mid-stem EI_{50} flexural rigidities are employed in determining the Cauchy number (Eq. 4.5). The resulting drag force predictions for the foliated and defoliated Hydralab trees are presented in Figs. 4.7 and 4.8 for the EI_{25} and EI_{50} cases, respectively.

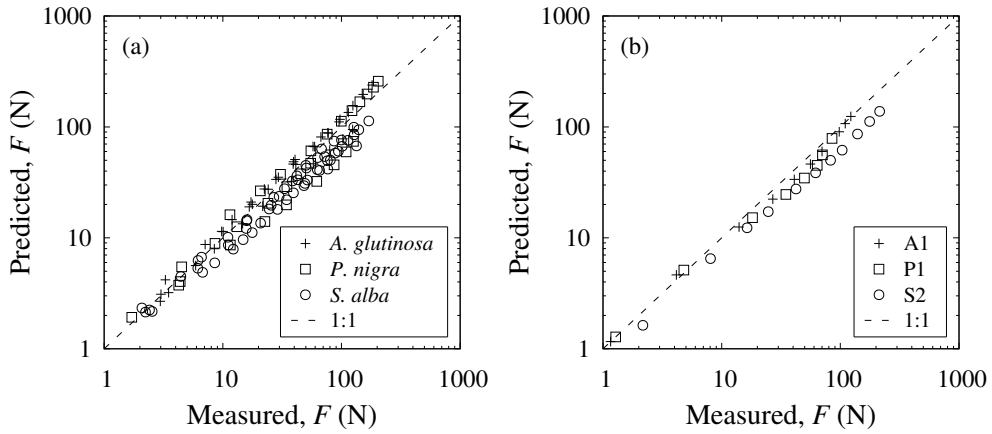

Figure 4.7: Drag force as predicted using the Cauchy reconfiguration model (Eq. 4.8) for the: (a) foliated; and (b) defoliated Hydralab trees. The value of EI_{25} was used for the flexural rigidity term in the Cauchy number calculation.

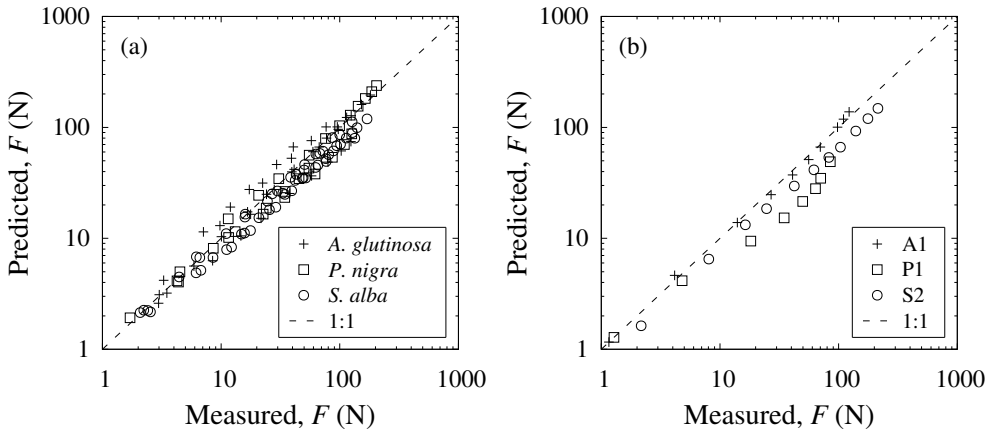

Figure 4.8: Drag force as predicted using the Cauchy reconfiguration model (Eq. 4.8) for the: (a) foliated; and (b) defoliated Hydralab trees. The value of EI_{50} was used for the flexural rigidity term in the Cauchy number calculation.

From Figs. 4.7 and 4.8, it can be seen that there is generally good agreement between the predicted and measured drag forces, although the model tends to somewhat underestimate the drag forces when the trees are defoliated. When comparing the EI_{25} and EI_{50} cases, the predicted drag forces are fairly similar. This is reflected in the average errors presented in Table 4.4.

Table 4.4: Average percentage errors $\epsilon_{\%}$ for predictions of the foliated and defoliated Hydralab trees' drag forces based on the Cauchy reconfiguration model (Eq. 4.8). The subscripts '25' and '50' for $\epsilon_{\%}$ denote whether EI_{25} or EI_{50}, respectively, was used to calculate the Cauchy number. The number of data points N used to calculate the average errors is also given.

	Foliated			Defoliated		
Species	$\epsilon_{\%25}$	$\epsilon_{\%50}$	N	$\epsilon_{\%25}$	$\epsilon_{\%50}$	N
A. glutinosa	17.4	22.1	39	10.1	6.6	10
P. nigra	22.9	17.3	28	17.6	40.5	8
S. alba	24.3	20.2	54	32.9	29	11

The difference in accuracy between the EI_{25} and EI_{50} cases is relatively minor, with EI_{25} producing lower errors for some species or foliation states and vice versa (Table 4.4). This suggests that the height at which the main-stem flexural rigidity is determined is not crucial, as long as both the second moment

of area I and modulus of elasticity E are measured at the same location.

It is interesting to note that the predictions for the defoliated *A. glutinosa* trees appear to be significantly more accurate than those for the foliated *A. glutinosa* trees (Table 4.4). This is most likely due to the small sample sizes used to determine the species-specific drag coefficient values for the defoliated *A. glutinosa* trees and thus the species-averaged values better reflect the individual specimens. Overall, the low average errors given in Table 4.4 represent roughly an order of magnitude improvement over a classical, constant characteristic drag coefficient approach that neglects the effects of reconfiguration (Eq. 2.2).

Application

In order to test whether the Cauchy reconfiguration model proposed in Eq. (4.8) is valid for vegetation of differing scale and relative submergence, the model is used to predict the drag force for the partially and fully submerged branches from the LWI experiments (see § 3.2.2). The artificial poplar branch is included here as it has been shown that its force-velocity response is similar to that of its natural counterparts (Dittrich *et al.* 2012).

The natural willow and natural and artificial poplar branches' height H, main-stem flexural rigidity EI, and projected area in still air A_{p0}, are taken from Table 3.4. For the partially submerged condition, the water depth is used as the height (i.e. $H = 12$ cm). The rigid drag coefficients C^*_{d0} and Vogel exponents ψ are taken from the species-averaged values for the foliated *P. nigra* and *S. alba* specimens in Tables 4.1 and 3.8, respectively. The resulting drag force predictions from the Cauchy reconfiguration model (Eq. 4.8) are presented in Fig. 4.9 for the partially and fully submerged LWI branches.

From Fig. 4.9 it can be seen that the model generally predicts the drag force with good accuracy, for both the partially and fully submerged conditions. For the partially submerged branches, however, the model tends to overestimate the drag force at the lower velocities. This is reflected in the average errors presented in Table 4.5, where the average errors for the partially submerged condition are roughly double those for the fully submerged condition.

Regardless of the difference between the partially and fully submerged

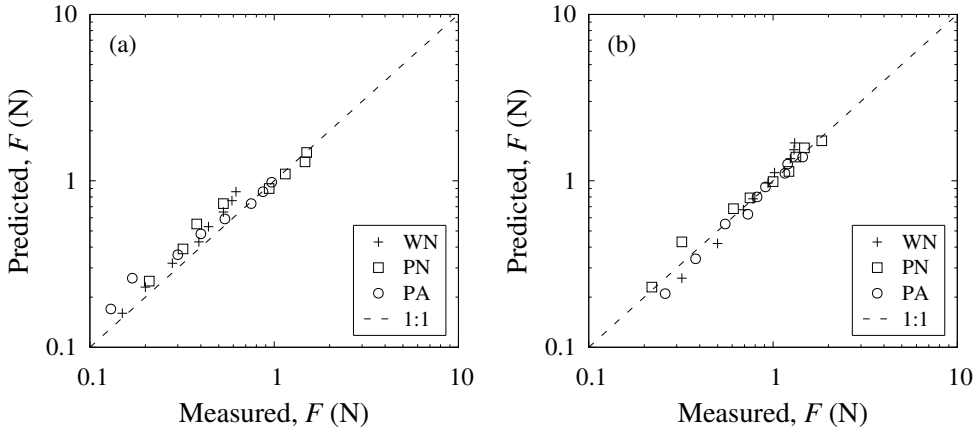

Figure 4.9: Drag force as predicted using the Cauchy reconfiguration model (Eq. 4.8) for the: (a) partially; and (b) fully submerged LWI branches.

Table 4.5: Average percentage errors $\epsilon_{\%}$ for predictions of the partially and fully submerged LWI branches' drag forces based on the Cauchy reconfiguration model (Eq. 4.8). The number of data points N used to calculate the average errors is also given.

	Partial sub.		Fully sub.	
Specimen	$\epsilon_{\%}$	N	$\epsilon_{\%}$	N
WN	20	8	12	9
PN	17.9	8	8.5	9
PA	18	8	6.8	9

branches, the low average errors presented in Table 4.5 suggest that the Cauchy reconfiguration model is independent of both vegetation scale and level of relative submergence.

4.3.3 Comparison to Existing Models

In the second chapter, a number of existing models for predicting the drag force of flexible riparian vegetation were discussed (§ 2.3.2). In this study, two of the most recent will be used to provide a benchmark against which the Cauchy reconfiguration model proposed in Eq. (4.8) can be measured.

The first is the friction factor model of Järvelä (2004), where the leaf area index (LAI) is used as the characteristic reference area (Eq. 2.6). The second

is the Cauchy reconfiguration model of Whittaker *et al.* (2013), which differs from that proposed here in the definition of the characteristic drag coefficient and Cauchy number terms (Eq. 2.9). The drag force predictions from each model are first presented, before the average errors from both models are summarized and compared to those of the Cauchy reconfiguration model developed in this thesis (Eq. 4.8).

Järvelä (2004)

For this approach, the form factor according to Eq. (2.6) is combined with the relationship between the form factor and the spatially-averaged drag force (Eq. 2.4), in order to provide a relationship for the drag force on a single plant:

$$F = \frac{1}{2}\rho C_{d\chi} A_L \left(\frac{U}{U_\chi}\right)^\chi U^2 \tag{4.9}$$

where $C_{d\chi}$ is a species-specific drag coefficient; A_L is the total one-sided leaf area; χ is equivalent to the Vogel exponent ψ; and U_χ is the lowest velocity used to determine χ.

Although recent work has expanded Eq. (4.9) to be applicable to both foliated and defoliated vegetation by splitting the total drag into its constituent leaf and stem parts (Västilä and Järvelä 2014), the defoliated Hydralab trees are not modelled here as there are only three trees for which one-sided stem areas were recorded (see Table 3.13). For the foliated Hydralab trees, the total one-sided leaf areas are taken from Table 3.12, species-specific Vogel exponents ψ are taken from Table 3.8, and it is assumed that $C_{d\chi}$ is equivalent to C^*_{d0} (Table 4.1). The lowest towing velocity of 0.125 m s^{-1} is used as the scaling velocity U_χ.

The drag forces exerted on the fully submerged LWI branches can also be modelled using Eq. (4.9). The species-specific Vogel exponents ψ and drag coefficients $C_{d\chi}$ are taken from the *P. nigra* and *S. alba* values in Tables 3.8 and 4.1, respectively. The total one-sided leaf area A_L is taken from Table 3.4, while the scaling velocity U_χ is equal to the lowest velocity tested for the Hydralab trees (0.125 m s^{-1}) as this was the lowest velocity used to determine the Vogel exponents. Unfortunately, the partially submerged branches cannot be modelled since the total one-sided leaf area is unknown for these specimens.

The resulting drag force predictions for the foliated Hydralab trees and fully submerged LWI branches are shown in Fig. 4.10. It can be seen that the model (Eq. 4.9) predicts the trees' drag forces with good accuracy, although there is some overestimation at the lower velocities. However, for the LWI branches, the model consistently overestimates the drag force by a relatively significant margin.

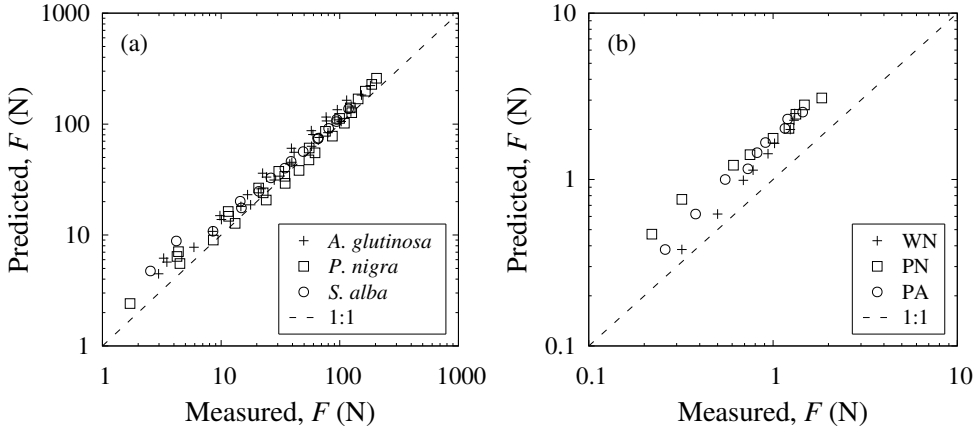

Figure 4.10: Drag force as predicted using the friction factor model (Eq. 4.9) of Järvelä (2004) for the: (a) foliated Hydralab trees; and (b) fully submerged LWI branches.

The fact that the drag forces for the LWI branches are overestimated by a relatively constant percentage (Fig. 4.10b) suggests that the curve of the force-velocity response, and thus the Vogel exponent, is correct. However, it also indicates that the 'rigid' drag coefficient C^*_{d0} may not be a suitable replacement for $C_{d\chi}$. Indeed, the values for $C_{d\chi}$ determined in previous studies are typically much less than those found for C^*_{d0} in this study (Table 4.1). For example, Aberle and Järvelä (2013) summarized $C_{d\chi}$ values from a number of previous studies, which included branches of *Populus nigra* ($C_{d\chi} = 0.33$), *Salix caprea* ($C_{d\chi} = 0.43$) and *Salix triandra x viminalis* ($C_{d\chi} = 0.53$).

Given that the model (Eq. 4.9) was able to predict the drag forces of the Hydralab trees with good accuracy using the same $C_{d\chi}$ values as used for the LWI branches, this might suggest that the model is not truly scale independent since separate $C_{d\chi}$ values may be required for each scale of vegetation.

Whittaker *et al.* (2013)

In this approach, the previous Cauchy reconfiguration model (Eq. 2.9) developed by Whittaker *et al.* (2013) is used to predict the Hydralab trees' drag forces. The drag forces for the LWI branches cannot be modelled here as their volumes were not recorded.

For the Hydralab trees, the model requires the height H (Table 3.2), main-stem flexural rigidity EI (Table 3.3), and total volume V (see Tables A.3 and A.1 for the foliated and defoliated trees, respectively). The species-specific Vogel exponents ψ are taken from Table 3.8. Species-specific linear relationships between the coefficient K and the trees' volumes are taken from Whittaker *et al.* (2013).

The resulting drag force predictions for the foliated and defoliated Hydralab trees are presented in Fig. 4.11. For the foliated alder and poplar trees, there is reasonable agreement between the measured and predicted drag forces. However, for the foliated willow trees, there appears to be significant deviation for a number of specimens. This is most likely a result of the linear K–V relationship not accurately describing the K values for those specimens.

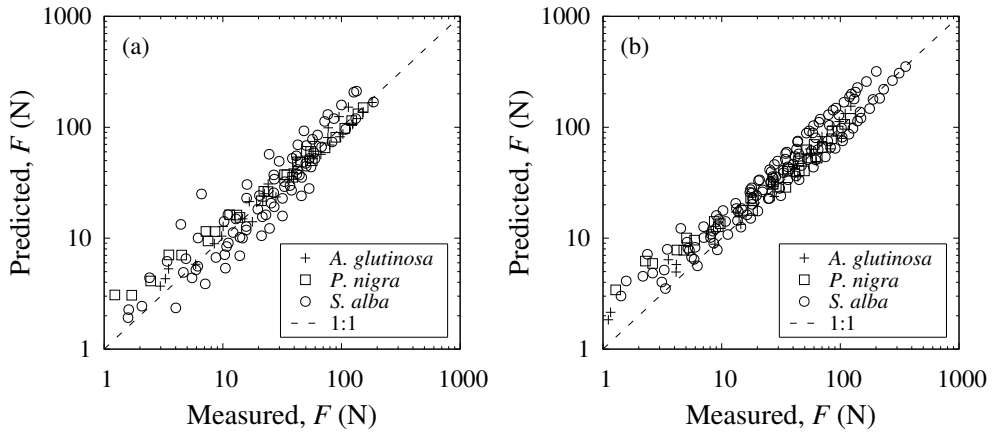

Figure 4.11: Drag force as predicted using the Cauchy reconfiguration model (Eq. 2.9) of Whittaker *et al.* (2013) for the: (a) foliated; and (b) defoliated Hydralab trees. The value of EI_{25} was used for the flexural rigidity term in the Cauchy number calculation.

When the trees are defoliated, the model tends to overestimate the drag force, particularly at the lower velocities (Fig. 4.11b). This is could possibly be due

to an incorrect parameterization of the Cauchy number in Eq. (2.9), since if the Cauchy number is less than unity there will be no reduction in the characteristic drag coefficient, thus leading to higher predicted drag forces.

Comparison

The average errors in the drag force predictions for each of the three models are summarized in Table 4.6 for the foliated Hydralab trees and the fully submerged LWI branches. The defoliated Hydralab trees and partially submerged LWI branches are not included as the two existing models (Eqs. 4.9 and 2.9) could not be applied to those data sets.

Table 4.6: Average percentage errors $\epsilon_{\%}$ for predictions of the foliated Hydralab trees' and fully submerged LWI branches' drag forces based on the current (Eq. 4.8) and two existing models, namely Eq. (4.9) (Järvelä 2004) and Eq. (2.9) (Whittaker *et al.* 2013). The number of data points N used to calculate the average errors is also given. The value of EI_{25} was used for the flexural rigidity term in the Cauchy number calculation.

Species /	Järvelä (2004)		Whittaker *et al.* (2013)		Current	
specimen	$\epsilon_{\%}$	N	$\epsilon_{\%}$	N	$\epsilon_{\%}$	N
A. glutinosa	31.3	33	26.6	33	17.4	39
P. nigra	19.2	28	29	28	22.9	28
S. alba	28.7	16	38.2	80	24.3	54
WN	52.6	9	-	-	12	9
PN	91.4	9	-	-	8.5	9
PA	73	9	-	-	6.8	9

It can be seen from Table 4.6 that the Cauchy reconfiguration model developed here (Eq. 4.8) has the lowest average errors in all cases, apart from for the poplar trees from the Hydralab experiments, where the model developed by Järvelä (2004) is more accurate. However, the difference of 3% in overall average error between the two models for those trees is relatively small.

For the independent LWI branch data, the difference in accuracy between the two models is much more pronounced, with the current model being almost 5–10 times more accurate. This may highlight scale dependency problems for the Järvelä (2004) approach. However, recent work by Jalonen *et al.* (2013)

found that the total one-sided area $A_T = A_S + A_L$ might be a better characteristic reference area than the one-side leaf area A_L for Eq. (4.9). Unfortunately A_T is only available here for one specimen, namely the alder tree A1, and therefore this approach was not tested.

The model of Järvelä (2004) is also dependent on an empirical scaling velocity U_χ (Eq. 4.9), which has to be determined experimentally and is not based on physical reasoning. Additionally, it is unclear how sensitive the model is to larger values of U_χ, since large errors may be introduced for velocities below this value.

While the Cauchy reconfiguration model proposed here has been found to be an improvement over existing drag force models (Table 4.6), it is noted that the projected area in still air A_{p0} may be more difficult to obtain in practice than the one-sided leaf area A_L. This is because A_L can be measured remotely (e.g. Rautiainen *et al.* 2003, Zheng and Moskal 2009, Antonarakis *et al.* 2010, Forzieri *et al.* 2011), while no such method currently exists for A_{p0}, which must be determined through photographic analysis.

4.3.4 Model Parameter Sensitivity Analysis

Although the current (Eq. 4.8) and previous drag force models (e.g. Eqs. 2.9 and 4.9) rely on only a couple of non-physical properties, typically a drag coefficient and a Vogel exponent, it is unclear how varying the values for these parameters affects the models' accuracy. Therefore, a sensitivity analysis for these parameters is undertaken for the Cauchy reconfiguration model developed in this thesis.

The resulting average errors for the model's drag force predictions for the Hydralab trees and LWI branches are presented in Figs. 4.12 and 4.13, respectively. The errors were obtained by varying the rigid drag coefficient C^*_{d0} from 0.25 to 1.5 in increments of 0.05, while the Vogel exponent ψ was varied with the same increment between 0 and -1.25. For the Hydralab trees, only the results from using the first quartile stem flexural rigidity EI_{25} in the Cauchy number calculation (Eq. 4.5) are presented here as the mid-stem flexural rigidity EI_{50} produced very similar patterns.

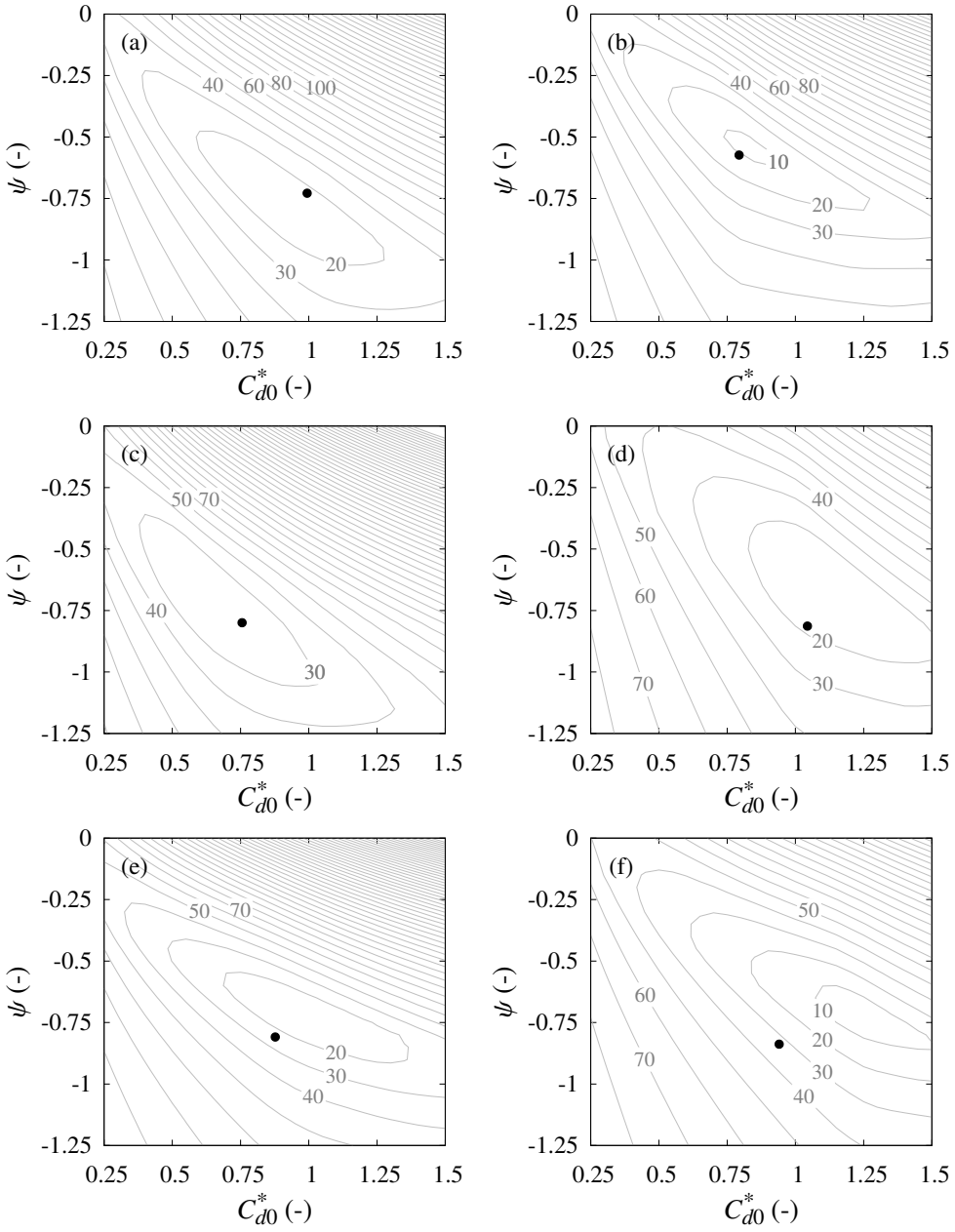

Figure 4.12: Sensitivity analysis for the Cauchy reconfiguration model parameters C^*_{d0} and ψ. Contour isolines show average percentage errors in the predicted drag force (obtained from Eq. 4.8) for the: (a,b) *A. glutinosa*; (c,d) *P. nigra*; and (e,f) *S. alba* Hydralab trees. The foliated and defoliated trees are in the left and right columns, respectively. The black dot indicates the values used in the model validation (§ 4.3.2). The value of EI_{25} was used for the flexural rigidity term in the Cauchy number calculation.

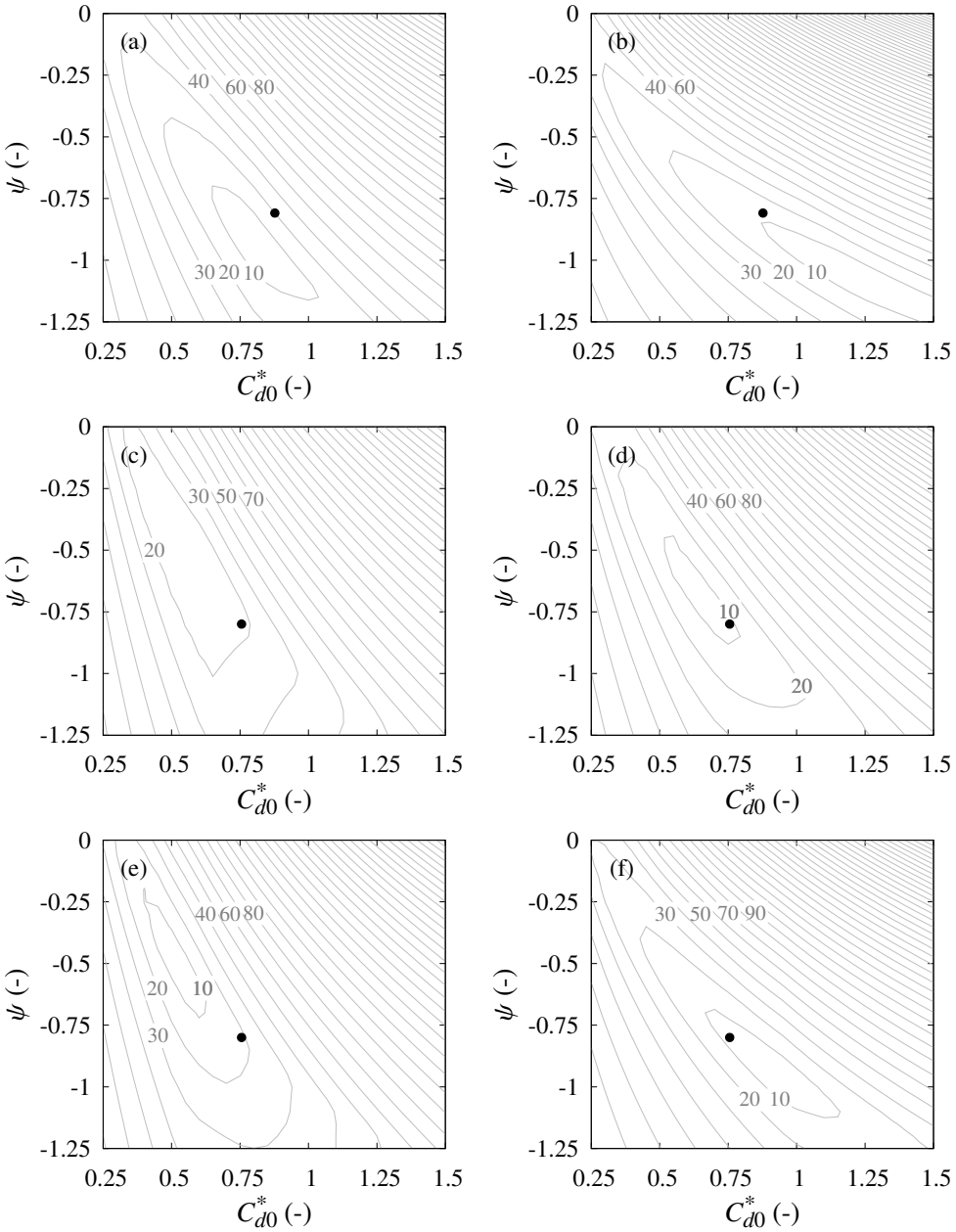

Figure 4.13: Sensitivity analysis for the Cauchy reconfiguration model parameters C^*_{d0} and ψ. Contour isolines show average percentage errors in the predicted drag force (obtained from Eq. 4.8) for the: (a,b) natural willow (WN); (c,d) natural poplar (PN); and (e,f) artificial poplar (PA) LWI branches. The partially and fully submerged branches are in the left and right columns, respectively. The black dot indicates the values used in the model validation (§ 4.3.2).

From Figs. 4.12 and 4.13 it can be seen that, for both the Hydralab trees and the LWI branches, there is a relatively large 'parameter space' for which the Cauchy reconfiguration model's average error is less than 30%. However, outside those regions, the average errors quickly increase, as can be seen by the steep 'gradient' of the contour lines towards the upper right and lower left of each sub-plot.

Considering the impact of foliage on the average errors for the Hydralab trees, the parameter space for which the model is reasonably accurate appears to shift towards the upper right corner (Fig. 4.12). This is consistent with the analyses in the previous chapter (§ 3), where the defoliated drag coefficients (Fig 3.21) and Vogel exponents (Table 3.8) were found to be greater than those of the foliated trees.

For the partially and fully submerged LWI branches, the parameter spaces for which the model is accurate are relatively similar (Fig. 4.13). This thus suggests that the Cauchy reconfiguration model is indeed independent of the relative level of submergence as the values for C^*_{d0} and ψ do not need to be altered depending on the flow depth.

In absence of experimental data, inspection of Figs. 4.12 and 4.13 indicates that values of $C^*_{d0} \approx 0.8$ and $\psi \approx -0.75$ would be reasonable estimates for foliated trees, while values of $C^*_{d0} \approx 1$ and $\psi \approx -0.7$ would be more suitable for defoliated trees. It is interesting to note that this would appear to contradict the species-specific assumption, since reasonably accurate predictions can be made using the same parameter values across species. However, species-specific values still result in more accurate predictions, at least for the sample sizes presented here.

4.4 Summary

The parameterization of the complex system of fluid-body interactions that occur for a flexible object in a fluid flow has often proved problematic when attempting to model such interactions. In this chapter, therefore, two drag force models have been developed and applied to two data sets consisting of submerged full-scale trees and partially and fully submerged branches.

The first model utilized empirical relationships to determine the vegetation's drag coefficient based on an area Reynolds number defined using the projected area in still air as the characteristic length scale (see § 4.2.1). While the model performed well when calibrated for the foliated and defoliated Hydralab trees, it was unable to accurately predict the drag forces for the independent LWI branches (see § 4.2.2). This indicates that such empirical relationships are not suitable for general purpose modelling as the parameters would have to be calibrated against experimental data for each type of vegetation and flow depth under consideration.

The second model was derived from theoretical consideration and employed a vegetative Cauchy number to parameterize the vegetation's reconfiguration due to hydrodynamic loading (see § 4.3.1). The model was first applied to the Hydralab trees using the previously derived drag coefficients and Vogel exponents, with good agreement found between the measured and predicted drag forces for both the foliated and defoliated trees (§ 4.3.2). The approach was then found to be independent of scale and flow depth as the model accurately predicted the drag forces for the partially and fully submerged LWI branches (§ 4.3.2).

When compared to two existing drag force models (Järvelä 2004, Whittaker *et al.* 2013; see § 4.3.3), the Cauchy reconfiguration model developed in this thesis was found to better predict the vegetation's drag force, particularly for the branch-scale LWI data. This is most likely due to the fact that the model proposed here has the ability to correctly model the vegetation's transition from a 'rigid' to a 'flexible' force-velocity response, without the need for empirical or subjective threshold velocities.

In addition, and compared to the Cauchy reconfiguration approach of Whittaker *et al.* (2013), the new model better parameterizes the Cauchy number and removes the need for the lumped empirical coefficient K and its accompanying relationships with the vegetation's physical properties. However, future work could perhaps focus on replacing the projected area in still air A_{p0} with a reference area that can be measured remotely, such as the total one-sided area A_T or one-sided leaf area A_L. This would also be consistent with the observations in the previous chapter (§ 3), where the foliage was found to contribute a large portion of the total drag (see § 3.3.1).

A sensitivity analysis was also performed for the two Cauchy reconfiguration

model parameters that cannot be directly measured: the rigid drag coefficient C^*_{d0} and the Vogel exponent ψ. This showed that reasonably accurate drag force predictions can be made in the absence of experimental calibration data if the parameter values are constricted to certain ranges.

Chapter 5

Numerical Modelling of Riparian Woodland

5.1 Introduction

The accurate treatment of riparian vegetation and woodland in hydrodynamic simulations is important due to their effect on velocities, shear stresses and water levels (e.g. Järvelä 2002b, James *et al.* 2004, 2008). The resistance of such vegetation is typically accounted for by using a bulk roughness coefficient such as Manning's n or the Darcy-Weisbach friction factor f. However, these terms are not derived from the physical properties or processes of the vegetation under flow action and can thus require a large amount of calibration or experience to set correctly. Further, purely representing the hydraulic impact of the vegetation via a bed roughness term negates the blockage effect due to the volume of the vegetation. In the case of dense vegetation, this blockage effect can be significant.

A more physical approach used in previous studies (e.g. Wu *et al.* 2001, Stoesser *et al.* 2003), is to directly include the vegetative drag force and blockage effect in the mass and momentum equations governing the motion of the fluid. In this chapter, therefore, the previously derived Cauchy reconfiguration drag force model (Eq. 4.5; see § 4.3.1) is incorporated into an existing two-dimensional hydrodynamic modelling code. The model is then applied to a river in Somerset so that the impact of riparian woodland on flood flows can be analysed.

The primary aim of this chapter is to investigate how the introduction of woodland impacts the flood characteristics of a mid-catchment river. Firstly, the underlying equations governing the motion of a fluid are introduced. The discretization of the governing equations using a finite differencing scheme is then discussed. A subsequent optimization of the computational code utilizing both CPU and GPU based techniques is then performed. The topographical and input data for the case study site are then used to create and calibrate a 2D model. Finally, the new Cauchy drag force model is parameterized for a range of scenarios, including non-forested and partially forested states, using both current and short-rotation coppice planting regimes and a floodplain storage method.

5.2 Governing Equations

5.2.1 Navier-Stokes Equations

The velocity field of a fluid can generally be described by the Navier-Stokes equations, which can be derived by applying Newton's second law to the fluid, along with pressure gradients and assumptions about the viscous stresses. In most practical engineering problems, the fluid flow can be assumed to be incompressible and is usually characterized by turbulent fluctuations. As a result, the instantaneous Navier-Stokes equations are often time-averaged to provide the Reynolds-averaged Navier-Stokes equations (e.g. Massey 2006):

$$\frac{\partial u}{\partial t} + u\frac{\partial u}{\partial x} + v\frac{\partial u}{\partial y} + w\frac{\partial u}{\partial z} = X - \frac{1}{\rho}\frac{\partial P}{\partial x} + \frac{1}{\rho}\left(\frac{\partial \sigma_{xx}}{\partial x} + \frac{\partial \tau_{yx}}{\partial y} + \frac{\partial \tau_{zx}}{\partial z}\right) \tag{5.1a}$$

$$\frac{\partial v}{\partial t} + u\frac{\partial v}{\partial x} + v\frac{\partial v}{\partial y} + w\frac{\partial v}{\partial z} = Y - \frac{1}{\rho}\frac{\partial P}{\partial y} + \frac{1}{\rho}\left(\frac{\partial \tau_{xy}}{\partial x} + \frac{\partial \sigma_{yy}}{\partial y} + \frac{\partial \tau_{zy}}{\partial z}\right) \tag{5.1b}$$

$$\frac{\partial w}{\partial t} + u\frac{\partial w}{\partial x} + v\frac{\partial w}{\partial y} + w\frac{\partial w}{\partial z} = Z - \frac{1}{\rho}\frac{\partial P}{\partial z} + \frac{1}{\rho}\left(\frac{\partial \tau_{xz}}{\partial x} + \frac{\partial \tau_{yz}}{\partial y} + \frac{\partial \sigma_{zz}}{\partial z}\right) \tag{5.1c}$$

where t is time; u, v, and w are the velocity components in each of the principal Cartesian axes x, y, and z respectively; ρ is the fluid density; P is the pressure; and the normal σ and shear τ stresses can be described using Einstein notation:

$$\sigma_{ii} = \mu\frac{\partial u_i}{\partial x_i} - \rho\overline{u_i'u_i'}; \qquad \tau_{ij} = \mu\frac{\partial u_j}{\partial x_i} - \rho\overline{u_i'u_j'} \tag{5.2}$$

where μ is the dynamic viscosity.

The variables X, Y, and Z represent external body forces and typically take the following values when considering gravity and the Coriolis effect:

$$X = 2\omega v \sin\phi \tag{5.3a}$$

$$Y = -2\omega u \sin\phi \tag{5.3b}$$

$$Z = -g \tag{5.3c}$$

where ω is the angular frequency of Earth (7.27×10^{-5} rad s^{-1}); ϕ is the latitude; and g is the acceleration due to gravity (9.81 m s^{-2}).

While the equations of (5.1) describe the motion or momentum of a fluid, a fourth relationship is required to maintain the conservation of mass within a control volume (Douglas *et al.* 2005). This is known as the continuity equation:

$$\frac{\partial u}{\partial x} + \frac{\partial v}{\partial y} + \frac{\partial w}{\partial z} = 0 \tag{5.4}$$

Turbulence Closure

When supplied with sufficient boundary and initial conditions, the combined momentum and continuity equations (Eqs. 5.1 and 5.4) can be used in a wide variety of modelling applications, including aeronautics, oceanography, physics and hydraulics. However, before being of use, the turbulent or Reynolds stresses $-\rho\overline{u_i'u_j'}$ (Eq. 5.2) must be modelled. This is because the Reynolds stresses are non-linear due to their fluctuating nature and therefore further assumptions and modelling are required in order to close the RANS equations (Rodi 1993).

This has led to the creation of a number of different 'turbulence-closure' models. These models introduce relationships between the mean motion of the fluid and the Reynolds stresses and thus provide the equations needed to solve for the extra unknowns (i.e. the time-averaged product of the fluctuating velocities $\overline{u_i'u_j'}$).

The first step towards such a model was proposed by Boussinesq in 1877. In an analogy with the kinematic viscosity of a fluid and the molecular viscosity

of a gas, he defined an eddy viscosity in order to relate the Reynolds stresses to the local mean velocity gradients. For incompressible flow, the Boussinesq hypothesis can be written using Einstein notation as (e.g. Massey 2006):

$$-\overline{u_i' u_j'} = \nu_t \left(\frac{\partial \overline{u_i}}{\partial x_j} + \frac{\partial \overline{u_j}}{\partial x_i} \right) - \frac{2}{3} k \delta_{ij} \tag{5.5}$$

where ν_t is the turbulent eddy viscosity; $k = \frac{1}{2}\overline{u_i' u_i'}$ is the turbulent kinetic energy (TKE); and δ_{ij} is the Kronecker delta.

In early applications, the eddy viscosity had to be determined empirically and had a constant value. To address these issues Prandtl introduced the mixing length hypothesis in 1925, which assumes that the eddy viscosity is proportional to the turbulent velocity fluctuations and a 'mixing length' (e.g. Shames 2003).

For wall-bounded flows, the eddy viscosity must vary with the distance from the wall so that:

$$\nu_t = l_m^2 \left| \frac{\partial u}{\partial y} \right| \tag{5.6}$$

where y is the distance normal to the wall; and l_m is the mixing length.

The mixing length depends on the nature of the flow and is a function of space. For example:

At a wall, i.e. $y = 0$	$l_m = 0$
Near a wall	$l_m = \kappa y$
Unbounded flow	$l_m = C\delta$

where κ is von Karman's constant (≈ 0.41); C is a constant; and δ is the boundary layer thickness.

Prandtl's mixing length hypothesis is still in common use today. This is because calculations based on the model are easy to undertake, since no additional differential equations need to be solved. However, there are a number of limitations. For instance, where the flow is bounded by non-planar walls it is impossible to estimate the distribution of mixing lengths with acceptable accuracy (Rodi 1993).

To overcome these problems many more turbulence closure models have been developed. These include the so called 'zero-equation' or algebraic models, such as a depth-averaged or mixing length model, that do not solve any additional

differential equations in order to predict the contributions of the turbulence (e.g. Beffa and Goring 1995, Wu *et al.* 2004, Defina and Bixio 2005). Slightly more advanced are the 'one-equation' models, such as Spalart-Allmaras (SA) and Goldberg, which calculate the eddy viscosity based on mean flow characteristics and empirical constants (e.g. Spalart and Allmaras 1994, Li and Yan 2007, Li and Zhang 2010). Similarly, there are a number of 'two-equation' models (e.g. k-ϵ and k-ω) that solve a further differential equation for the transport of turbulent kinetic energy (e.g. Lopez and Garcia 2001, Katul *et al.* 2004, Wu *et al.* 2004, King *et al.* 2012).

Another popular closure model is that of large eddy simulation (LES), where the large-scale eddies within the flow are resolved numerically, while only the small-scale turbulent eddies are modelled (e.g. Finnigan *et al.* 2009, Stoesser *et al.* 2009). Also of note is direct numerical simulation (DNS), whereby the spatial and temporal resolutions of the computational domain are increased to such an extent that all the turbulent processes can be resolved (e.g. Zhou *et al.* 1999, Breugem *et al.* 2006).

5.2.2 Shallow Water Equations

Often in fluid dynamics the horizontal scale of the area under consideration is much greater than the vertical scale. For example, this occurs in harbours, estuaries and even oceans, where the ocean depth is negligible when compared to the horizontal lengths. Under these conditions, the continuity equation implies that the vertical velocity component w is small in comparison to the horizontal components.

Integrating the Reynolds-averaged Navier-Stokes and continuity equations (Eqs. 5.1 and 5.4) over the flow depth removes the vertical velocity component. The resulting two-dimensional (2D) equations are known as the shallow water equations (SWE) and, once numerically solved, provide the depth averaged velocity field. The depth-averaged continuity and momentum components of the SWEs can be written in general form as:

$$\frac{\partial \eta}{\partial t} + \frac{\partial q_x}{\partial x} + \frac{\partial q_y}{\partial y} = 0 \tag{5.7a}$$

$$\frac{\partial q_x}{\partial t} + \frac{\partial \left(\beta q_x^2/\zeta\right)}{\partial x} + \frac{\partial \left(\beta q_x q_y/\zeta\right)}{\partial y} = X - \frac{\zeta}{\rho}\frac{\partial P_a}{\partial x} - g\zeta\frac{\partial \eta}{\partial x} - \frac{\tau_{bx}}{\rho} + \frac{\tau_{wx}}{\rho} + \nu_t\left(2\frac{\partial^2 q_x}{\partial x^2} + \frac{\partial^2 q_x}{\partial y^2} + \frac{\partial^2 q_y}{\partial x \partial y}\right) \tag{5.7b}$$

$$\frac{\partial q_y}{\partial t} + \frac{\partial \left(\beta q_x q_y/\zeta\right)}{\partial x} + \frac{\partial \left(\beta q_y^2/\zeta\right)}{\partial y} = Y - \frac{\zeta}{\rho}\frac{\partial P_a}{\partial y} - g\zeta\frac{\partial \eta}{\partial y} - \frac{\tau_{by}}{\rho} + \frac{\tau_{wy}}{\rho} + \nu_t\left(\frac{\partial^2 q_y}{\partial x^2} + 2\frac{\partial^2 q_y}{\partial y^2} + \frac{\partial^2 q_x}{\partial x \partial y}\right) \tag{5.7c}$$

where t is time; η is the water surface elevation; $\zeta = h + \eta$ is the total water depth; q_x and q_y are the discharges per unit width in the x and y directions, respectively; β is the correction factor for non-uniform vertical velocity profiles, where $\beta = 1.016$ for a seventh power-law velocity distribution (e.g. Shames 2003); X and Y are the depth-averaged body forces, such as the Coriolis force (see Eqs. 5.3a and 5.3b); P_a is the atmospheric pressure; g is the acceleration due to gravity; τ_b and τ_w are the bed and wind shear stresses, respectively; and ν_t is the kinematic eddy viscosity (assuming that the kinematic viscosity of water is negligible in comparison).

It should be noted that although a vertical velocity term is not explicitly included in the shallow water equations, the vertical velocity is not necessarily zero. Once the horizontal velocities and free surface level have been solved for, the vertical velocity can be recovered via the continuity equation. This is important since the vertical velocity cannot be zero where there is a change in the bed depth (Liang *et al.* 2007).

5.3 Numerical Model

Since the shallow water equations are a set of hyperbolic partial differential equations, there is often no analytical solution, except for the most trivial of cases. Therefore, solutions have to be obtained via numerical approximation methods. For computational fluid dynamics there are two main approaches: finite difference and finite volume.

The finite difference method utilizes a grid system, usually of equally spacing Δx and Δy, to divide the domain into cells. The variables are then represented at the intersections or mid points of these cells and are defined as a function of the variables in other cells so that when $\Delta x, \Delta y \rightarrow 0$, the finite difference approximation is consistent with the original differential equation. The solution is progressed by Δt after each complete computational step.

The finite volume method is similar in that it also calculates variables at discrete points on a grid. However, the grid is not limited to being regular in shape and can take the form of an unstructured mesh. The variables are typically located at the centroids of the mesh cells and are integrated over the cell volume. A set of linear simultaneous equations then defines the fluxes between each cell.

One of the main advantages of the finite difference method is that it requires less computational time compared to the finite volume method, as shown by Weare (1976), even though the finite volume discretization generally requires fewer grid points. Another advantage is that it is relatively straightforward to transfer differential equations into finite difference form. However, since the method must be carried out on a regular grid, irregular boundary conditions such as those found in alluvial river systems can be hard to represent.

On the other hand, the unstructured nature of the finite volume approach means that is capable of handling any form of boundary condition. The finite volume method is also inherently mass conservative since the flux entering a given volume is identical to the flux leaving the adjacent volume.

In this chapter, an existing finite differencing scheme is employed as the basis for the numerical modelling. The choice of a finite differencing scheme over a finite volume scheme was motivated by the ease of grid generation, computational efficiency and amenability to additional numerical developments. While an unstructured finite volume mesh may have provided more resolution in critical areas, such as the main river channel, the time required to create such a mesh would have been significant. Further, the domain could easily be enclosed within a rectangular area and there was no need for irregular boundary conditions in the case study modelled herein.

5.3.1 DIVAST-TVD

An existing in-house hydrodynamic modelling code was chosen as the basis for further development. The Depth-Integrated Velocity and Solute Transport Total Variation Decreasing (DIVAST-TVD) model solves the SWEs (5.7) using a second-order accurate explicit scheme on a cell-centered grid (Liang *et al.* 2006).

The model first applies the operator-splitting technique to the SWEs (5.7):

$$\frac{\partial \mathbf{X}}{\partial t} + \frac{\partial \mathbf{F}}{\partial x} = \mathbf{S} \tag{5.8a}$$

$$\frac{\partial \mathbf{X}}{\partial t} + \frac{\partial \mathbf{G}}{\partial x} = \mathbf{T} \tag{5.8b}$$

where $\mathbf{X}$ represents the independent variables η, q_x, and q_y; $\mathbf{F}$ and $\mathbf{G}$ represent the flux terms; and $\mathbf{S}$ and $\mathbf{T}$ represent the source terms.

The MacCormack 'predictor-corrector' scheme (e.g. Wendt 2009) is then used to solve the two one-dimensional hyperbolic equations, i.e. for Eq. (5.8a):

$$\mathbf{X}_i^p = \mathbf{X}_i - (\mathbf{F}_i - \mathbf{F}_{i-1}) \cdot \Delta t/\Delta x + \mathbf{S} \cdot \Delta t \tag{5.9a}$$

$$\mathbf{X}_i^c = \mathbf{X}_i - \left(\mathbf{F}_{i+1}^p - \mathbf{F}^p\right) \cdot \Delta t/\Delta x + \mathbf{S}^p \cdot \Delta t \tag{5.9b}$$

where the superscripts p and c indicate the predictor and corrector steps, respectively; the subscripts denote the spatial grid cell; and Δt and Δx are the temporal and spatial intervals, respectively.

An additional TVD step is then performed at the corrector stage so that spurious numerical oscillations are avoided in regions of sharp-gradients, or shocks. This allows the model to accurately capture trans- and super-critical flow conditions. The full details of the numerical solution scheme can be found in Liang *et al.* (2006).

In this study, the barometric pressure and wind shear stress terms in Eq. (5.7) are neglected. The vegetative drag force term requires no special treatment, while the second-order turbulent diffusion terms are discretized using a standard central differencing scheme. The cross-derivative turbulent diffusion terms are assumed to be negligible. The drag force and turbulent eddy viscosity models are detailed below.

The choice of a TVD scheme over a more traditional solution scheme, such as the Alternating Direction Implicit (ADI) method, was originally motivated by the need for a shock-capturing model in order to model steep, upper-river catchments where super-critical flows are likely to occur during large flood events. While the final site chosen for modelling in this study is situated towards the upper-catchment, the surrounding floodplain is relatively flat. This suggests that a shock-capturing scheme is less crucial and that a side-centered, ADI approach may also be suitable; however, considerable program development had been undertaken on DIVAST-TVD prior to the finalization of the site location.

5.3.2 Bed Shear Stress

The bed shear stress within DIVAST-TVD is represented in the form of a quadratic friction law. In the x direction it is given by:

$$\tau_{bx} = \frac{\rho g q_x \sqrt{q_x^2 + q_y^2}}{\zeta^2 C^2} \tag{5.10}$$

where C is the Chezy coefficient, which typically varies between 20 $\mathrm{m}^{1/2}\,\mathrm{s}^{-1}$ and 70 $\mathrm{m}^{1/2}\,\mathrm{s}^{-1}$ in rivers and floodplains (Weiyan 1992).

The Chezy coefficient can be calculated in a number of different ways within DIVAST-TVD. The simplest is to specify a constant value for each grid point at the start of the simulation. However, this approach obviously prevents any variation with flow depth or Reynolds number. A more common approach relates the Chezy coefficient to the local flow depth and Manning's n via:

$$C = \frac{R_h^{1/6}}{n} \tag{5.11}$$

where R_h is the hydraulic radius and is taken as the flow depth ζ in wide, open channel flow.

For fully rough, turbulent flows (i.e. $Re \gg 1000$), the Chezy coefficient can also be related to the local bed roughness using a modified version of the Colebrook-White equation:

$$C = -2\sqrt{8g}\log_{10}\left(\frac{k_s}{12\zeta}\right) \tag{5.12}$$

where k_s is the equivalent sand grain size, or roughness length (Chow 1973).

The advantage of using Eq. (5.12) is that the Chezy coefficient can be more closely related to the physical properties of the bed surface, such as dunes, ripples or boulders. However, for transitional flows ($500 < Re < 2000$) the Chezy coefficient is also dependent on the Reynolds number, i.e.:

$$C = -2\sqrt{8g}\log_{10}\left(\frac{k_s}{12\zeta} + \frac{2.5}{\sqrt{8g}Re}C\right) \tag{5.13}$$

where C is solved for in an iterative process.

In this study, the high grid resolution of the computational domain (made possible via the optimizations detailed in the next section) enables local differences in water levels, velocities and bed shear stresses due to inclusion or exclusion or Reynolds number effects to be investigated.

5.3.3 Vegetative Drag Force

Decoupling the bed friction and drag force, instead of artificially increasing the surface roughness, ensures that the bed shear stress remains physically correct. Therefore, the vegetation in the following case study is incorporated into the SWEs via a drag force term in the momentum equations (Eqs. 5.7b and 5.7c) and a porosity term in the continuity equation (Eq. 5.7a). The drag force terms in the x and y directions, respectively, are:

$$F_x = \frac{1}{2}NC_dA_p\frac{q_x\sqrt{q_x^2 + q_y^2}}{\zeta^2} \tag{5.14a}$$

$$F_y = \frac{1}{2}NC_dA_p\frac{q_y\sqrt{q_x^2 + q_y^2}}{\zeta^2} \tag{5.14b}$$

where N is the number of trees per m^2.

In the new Cauchy drag force model (Eq. 4.8; see § 4.3.1), the characteristic drag coefficient C_dA_p varies with velocity to mimic the effects of flexible vegetation's reconfiguration (Eq. 4.7) and is determined as a function of the vegetative Cauchy number (Eq. 4.5).

The implementation within DIVAST-TVD allows the user to specify a relationship between the flow depth ζ and projected area A_{p0} for each vegetation type, thus allowing the model to be applied to vegetation in both submerged and non-submerged conditions.

The blockage effect of the vegetation is accounted for via a porosity term:

$$\phi = 1 - N\frac{\pi D^2}{4} \tag{5.15}$$

where D is the equivalent cylinder diameter of the submerged portion of the vegetation.

Considering the blockage effect in the SWEs, the conservation of mass equation (Eq. 5.7a) then becomes:

$$\phi\frac{\partial \eta}{\partial t} + \frac{\partial q_x}{\partial x} + \frac{\partial q_y}{\partial y} = 0 \tag{5.16}$$

while the bed shear stress equation (Eq. 5.10) is similarly modified to account for the bed area occupied by the vegetation, i.e. in the x direction:

$$\tau_{bx} = \phi\frac{\rho g q_x\sqrt{q_x^2 + q_y^2}}{\zeta^2 C^2} \tag{5.17}$$

5.3.4 Turbulence Model

In order to include the turbulent diffusion terms within DIVAST-TVD, a model for the eddy viscosity is developed as these terms were originally neglected. Assuming that the turbulent shear stress is dominated by the bottom friction, Fischer *et al.* (1979) proposed the following model for the depth-averaged eddy viscosity:

$$\nu_t = C_e u_* \zeta \tag{5.18}$$

where C_e is an empirical coefficient; $u_* = \sqrt{\tau_b/\rho}$ is the shear velocity; and ζ is the flow depth (Fischer *et al.* 1979).

Theoretically, C_e should be equal to $\kappa/6$, where κ is the von Karman's constant. However, it is commonly accepted that C_e may take values ranging from 0.15 in flumes to 1.5 in coastal and estuarine areas (Elder 1959, Fischer *et al.* 1979). In the absence of calibration data, a value of $C_e = 1.2$ is recommended (Falconer

and Chen 1991). Referring to Eq. (5.10) and rearranging, the final depth-averaged eddy viscosity model can thus be written:

$$\nu_t = \frac{C_e\sqrt{g(q_x^2 + q_y^2)}}{C} \tag{5.19}$$

Although Eq. (5.19) is applicable in regions of open flow, significant errors may be introduced near rigid walls since it cannot account for horizontal velocity gradients. To address this issue, Wu *et al.* (2004) introduced a modified mixing length model by combining the depth-averaged approach with Prandtl's mixing length theory:

$$\nu_t = \sqrt{(\alpha u_* \zeta)^2 + \left(l_h^2|\overline{S}|\right)^2} \tag{5.20}$$

where α is an empirical coefficient, analogous to C_e; l_h is the horizontal mixing length; and $|\overline{S}| = \left[2\left(\partial u/\partial x\right)^2 + 2\left(\partial v/\partial y\right)^2 + \left(\partial u/\partial y + \partial v/\partial x\right)^2\right]^{1/2}$.

The horizontal mixing length is a function of the distance to the nearest surface, i.e.:

$$l_h = \kappa \min\left(c_m\zeta, y\right) \tag{5.21}$$

where c_m is an empirical constant set to 1.2; ζ is the flow depth; and y is the distance to the nearest wall. In the case of river and floodplain modelling, a dry cell is counted as a wall when determining y.

More advanced turbulence models, such as the 'one-equation' SA or 'two-equation' depth-averaged k-ϵ model proposed by Rastogi and Rodi (1978), are not implemented in this study due to their higher computational cost. Furthermore, it has been shown that the velocity distributions predicted by the depth-averaged and mixing length models are very similar to those predicted by the k-ϵ model and its variants for simple river channels (Wu *et al.* 2004).

5.4 Model Optimization

The explicit TVD-MacCormack solution scheme detailed above is particularly computationally efficient, especially when compared to other implicit methods (Liang *et al.* 2006). However, the original version of DIVAST-TVD may be considered as a naive implementation in terms of optimization. Therefore, three

approaches are taken to improve program run time, namely: general serial optimizations on a single central processing unit (CPU); parallel processing on multiple CPU cores using shared memory; and parallel processing on a graphical processing unit (GPU). Combined, these optimizations enable simulations at a high spatial resolution over a large computational domain ($> 2 \times 10^5$ grid points) to be completed in a more manageable time-frame (hours versus days).

In addition to the following CPU and GPU optimizations, a number of improvements were made to the original code. While not strictly optimizations in the sense that they decreased program execution time, they none-the-less enhance the functionality and maintainability of the code.

These 'quality-of-life' improvements include converting the code from a mix of Fortran 77 and 95 with GNU extensions, to strict Fortran 2003. This ensured that the code would be fully portable across different compilers and hardware. It was checked using the `gfortran` compiler option `-std=f2003`. Pointer arithmetic and operations were also used where applicable in order to reduce the number of lines of code required for certain tasks.

The program was also moved from a single, monolithic source file to a more modular, distributed system. In this, each logical part of the program, such as file input and output routines, were assigned to separate modules and files. This results in easier comprehension of program flow and function and faster program compilation since only those files that have changed need to be re-compiled. Such a structure also allows additional modules to be quickly added and incorporated into the program.

Other minor changes include the use of `implicit none` throughout the code to reduce accidental programming errors. This was enforced using the `gfortran` compiler option `-fimplicit-none`. Stronger error checking and more useful error messages and exit codes were also introduced. Finally, the file input routines were modified so that the input data required to run a simulation is now split into multiple files containing various parameters. This results in a smaller overall project size since the larger and more constant data, such as the domain specification or digital elevation data, is no longer duplicated when creating alternate scenarios.

5.4.1 CPU Optimization

Serial Optimizations

When performing optimization of serial Fortran code, gains can easily be obtained by analysing the order in which nested loops are executed. For example, consider the two code snippets:

Listing 5.1: Row-major indexing

```
do i = 1, n
  do j = 1, n
    a(i,j) = b(i,j)
  end do
end do
```

Listing 5.2: Column-major indexing

```
do j = 1, n
  do i = 1, n
    a(i,j) = b(i,j)
  end do
end do
```

Although the two listings are functionally identical, the swapped order of the outer loop in List. 5.2 will enable more efficient use of the cache on the CPU. This is because Fortran stores arrays in linear memory using column-major order. When the program requests the value stored at a particular array location, the CPU will also pre-fetch contiguous memory addresses into the CPU cache. Therefore, accessing array elements by varying the left-most subscript with a stride of one will allow the CPU to reuse data already loaded into the cache and minimize the number of comparatively costly memory fetches.

Cache efficiency must also be considered when selecting the level of precision required for each value or array. For example, an array of 4 byte values will be traversed almost twice as fast as its 8 byte counterpart. This is due to the fact that twice as many 4 byte values can be stored in the CPU cache compared to 8 byte values.

Other miscellaneous improvements made to the code include moving loop counters to the outermost loop possible to reduce unnecessary updating; removing inefficient memory allocation and deallocation by pre-allocating memory during program initialization; and ensuring that the intent of each subroutine and function argument is explicitly declared so that the compiler can make suitable optimizations.

The impact of the aforementioned serial optimizations was determined by benchmarking the modified code against the original code. The hardware and

software used in the benchmarking tests are detailed in Table 5.1, while the model parameters for the test case are listed in Table 5.2.

Table 5.1: Hardware and software used to benchmark DIVAST-TVD code.

CPU model	Intel Core i5-2500
CPU clock frequency	3.3 GHz
CPU cores / threads	4 / 4
CPU cache (L1 / L2 / L3)	64 / 256 / 6,144 kB
Memory	4 GB DDR3
Memory clock frequency	1,333 MHz
Operating system	Linux 3.5.0-36
Compiler	gfortran v4.7.3
Compiler flags	`-O3 -mtune=native`

Table 5.2: Model parameters used to benchmark DIVAST-TVD code.

Grid cells	213,526
Grid size	1 m
Simulation time	48 hrs
Time-step	$0.01 \leq \Delta t \leq 1$ s

The results of the initial benchmarking of the original and optimized serial codes are presented in Table 5.3. It can be seen that even with these relatively modest changes a speed-up of 1.62 is obtained. It should also be noted that the speed gains were achieved even though the optimized serial code performed slightly more computational work due to new features, such as the drag force and eddy viscosity models detailed above, being added.

Table 5.3: Benchmarking results for serial DIVAST-TVD code. Speed-ups are calculated relative to original code.

Code	Duration (hh:mm:ss)	Speed-up
Original	22:41:21	1
Serial	14:00:20	1.62

Parallel Optimizations

The shift in focus from serial to parallel applications has been motivated by the relative stagnation in the raw clock frequency of CPUs since the beginning of the 21st century (Fig. 5.1). This is mainly due to problems with heat dissipation and power consumption at high clock speeds. The number of transistors available per area is still currently following Moore's law, however, and the increase in transistor count has been invested into multiple cores on the same CPU microchip.

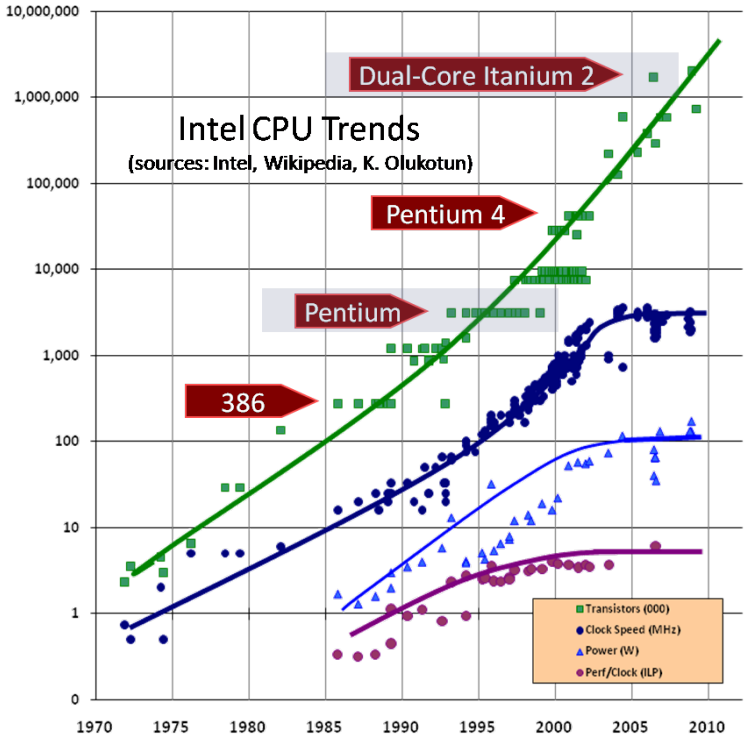

Figure 5.1: Variation in CPU properties over time for the Intel range of CPUs. Reproduced from Sutter (2005).

Modern CPUs typically have 4 to 16 separate cores that can process instructions and data in parallel. In order to access that parallelism, program code must be modified to split up its work into chunks or 'threads' that then execute individually and in parallel. This is usually implemented using a third-party application program interface (API). The two most common shared-memory APIs for Fortran are Pthreads and OpenMP. In the case of distributed systems, where multiple

processing elements are connected by a network, a message passing API, such as MPI, is required.

In this study, the hardware used to benchmark the optimized codes consisted of a single workstation (Table 5.1). Therefore, the system utilized shared memory and the choice of APIs was between Pthreads and OpenMP. The former provides a very low-level API for fine-grained control over individual threads, while the later provides a higher-level API. OpenMP was chosen for this study since it enables rapid development and ease of scalability with regards to thread count. Another advantage of OpenMP is that utilizes comment style pragmas to instruct the compiler and can thus be easily compiled into serial code if required (see List. 5.3). This ensures that the code remains portable across parallel and non-parallel architectures.

Listing 5.3: Example parallelization using OpenMP

```
!$omp parallel do private(i,j)
do j = 1, n
  do i = 1, n
    a(i,j) = b(i,j)
  end do
end do
!$omp end parallel do
```

Although some routines in DIVAST-TVD, such as file input and output, cannot be parallelized, the explicit scheme used to solve the SWEs is particularly amenable to parallelization. However, the maximum speed-up of a program as a result of parallelization is governed by Amdahl's law:

$$S(N_p) = \frac{1}{(1 - P) + \frac{P}{N_p}} \tag{5.22}$$

where S is the speed-up; N_p is the number of processors; and P is the proportion of the program which can be parallelized.

In the benchmarking tests carried out herein, four processors were available (Table 5.1). Referring to Eq. (5.22) and assuming that roughly 90% of the DIVAST-TVD code is suitable for parallelization, the maximum achievable speed-up is 3.08. The speed-up compared to the original code, however, should be

greater since the serial optimizations detailed above have increased the efficiency of the non-parallelizable sections of the code.

Table 5.4: Benchmarking results for CPU parallelized DIVAST-TVD code. Speed-ups are calculated relative to original code.

Code	Duration (hh:mm:ss)	Speed-up
Original	22:41:21	1
Serial	14:00:20	1.62
Parallel (CPU)	06:21:45	3.57

The results of the parallel optimizations are presented in Table 5.4. It can be seen that the OpenMP parallelized model was over three and a half times faster than the original model and was 2.2 times quicker than the optimized serial code. The reason that the maximum theoretical speed-up of 3.08 over the optimized serial code was not obtained is likely due to the overhead of thread creation and work sharing, which can be significant for those loops where the computational effort is low.

5.4.2 GPU Optimization

In conjunction with the shift from serial to parallel processing, there has been a rise in general-purpose computing on graphics processing units (GPGPU). This is because modern GPUs often exceed the computational power of the CPU that instructs them, due to the massively parallel architecture demanded by complex 3D graphics (Fig. 5.2). However, until recently, the power of such graphics cards was obscured by the need to translate generic computational problems into problems that could be rendered by the OpenGL graphics API.

To simplify the process of utilizing a GPU's resources, Nvidia released the Compute Unified Device Architecture (CUDA) API for the C language in the spring of 2007. The CUDA API makes it significantly easier to interact with the GPU and provides the necessary tools to communicate between the CPU host and the GPU device.

While there are Fortran interfaces for the CUDA API, they are currently proprietary and therefore the entire DIVAST-TVD code base (excluding the file

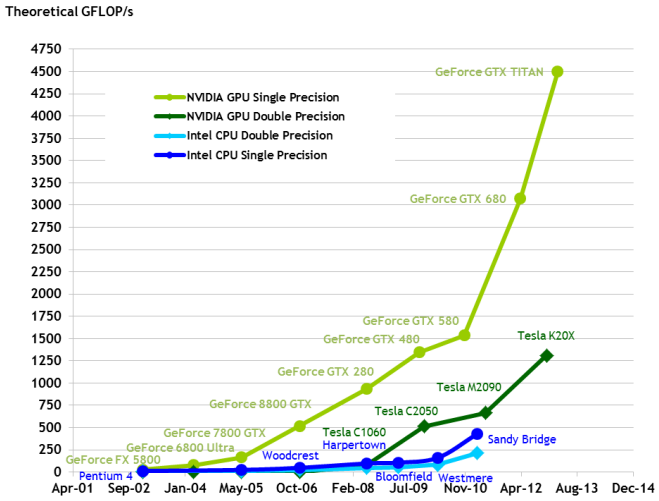

Figure 5.2: Comparison of theoretical floating-point operations (FLOP) per second between modern Intel CPUs and Nvidia GPUs. Reproduced from Nvidia (2013).

input/output routines) was translated into the C language to enable the use of the CUDA API in this study. The use of an open-source API, such as OpenCL, was not considered since the CUDA API is optimized specifically for Nvidia GPUs, whereas OpenCL is designed more towards portability. In CUDA terminology, the CPU is referred to as the host and the GPU is called the device. The layout of a CUDA-enabled GPU is shown schematically in Fig. 5.3.

Each GPU device provides multiple streaming multiprocessors (SMs), that are themselves comprised of individual processors. Once data has been sent from the host to the device, it is stored in the device, or global, memory. Global memory is accessible by all the SMs and has the largest capacity. The SMs can also make use of faster, although smaller, blocks of shared memory that are only visible within each SM. Finally, each processor has a small number of on-board registers that provide rapid access to important variables. The speed at which each processor can access data in the different types of memory is visually represented by the proximity of the memory to the processors in Fig. 5.3. The technical specifications for the Nvidia GPU used herein are presented in Table 5.5.

The processors within each SM can run in parallel by independently executing the same sets of operations on different sets of data (otherwise known as SIMD).

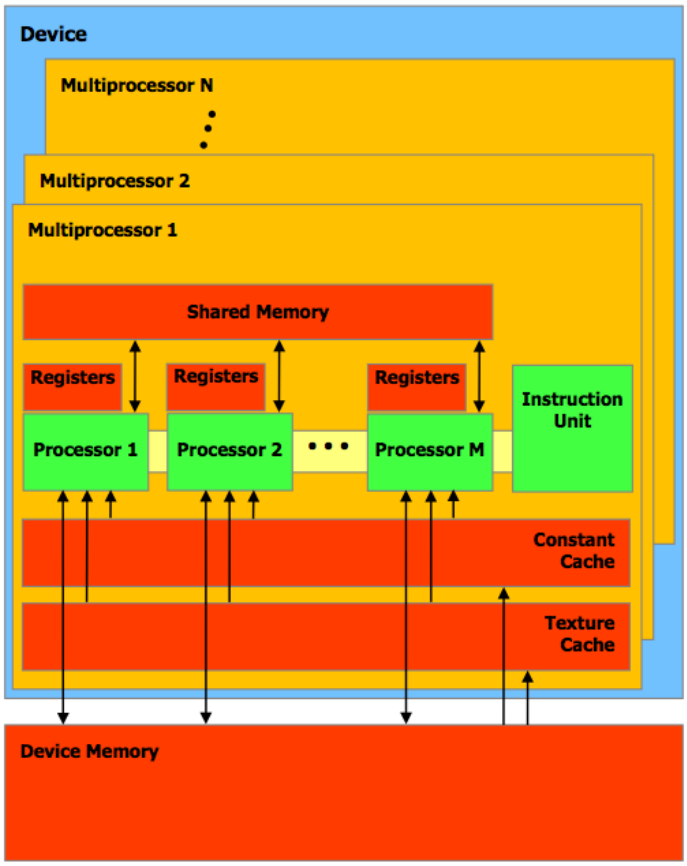

Figure 5.3: Schematic of a CUDA-enabled GPU architecture. Reproduced from Nvidia (2013).

Table 5.5: Technical specifications of the GPU used to benchmark the GPU optimized DIVAST-TVD code.

Model	Nvidia Quadro 4000
Core clock frequency	475 MHz
Memory	2 GB GDDR5
Memory clock frequency	700 MHz
Memory bandwidth	89.6 GB s^{-1}
CUDA cores	256
CUDA compute capability	2.0

In CUDA, these operations are defined in 'kernels', which loosely correlate to loops or subroutines in a serial application. The kernels are launched from the CPU host and are split into grids of 'blocks' on the GPU so that each block is handled by a single SM. The blocks are then also split into 'threads', where each thread is assigned to one of the SM's processors.

In order to minimize costly host-device memory transfers, every subroutine in DIVAST-TVD was rewritten as a device kernel. Combined with the large global memory space (Table 5.5), this enabled the entire computation domain to be kept on the device, without the need for host-device memory transfers at every time-step. The overall program control flow for the GPU optimized version of DIVAST-TVD is shown in Fig. 5.4. During the rewriting process, the efficient use of registers, shared memory and global memory was a high priority.

Table 5.6: Benchmarking results for GPU parallelized DIVAST-TVD code. Speed-ups are calculated relative to original code.

Code	Duration (hh:mm:ss)	Speed-up
Original	22:41:21	1
Serial	14:00:20	1.62
Parallel (CPU)	06:21:45	3.57
Parallel (GPU)	03:41:37	6.14

The execution time and relative speed-up of the GPU optimized code compared to the original code are presented in Table 5.6. It can be seen that the GPU optimized code runs over six times faster than the original code. Referring to Amdahl's law and Table 5.5, the maximum theoretical speed-up achievable with 256 cores is 9.66. The slightly lower observed speed-up of 6.14 suggests that the GPU code is memory bound. Although efficient use of registers and shared memory are already employed, future work to utilize texture memory may alleviate this issue.

It is important to note that a purely CPU-based parallel optimization approach may be faster in cases where computational effort per time-step is low (i.e. small grid domains), due to the overhead involved in launching each kernel and also the low host-device memory bandwidth.

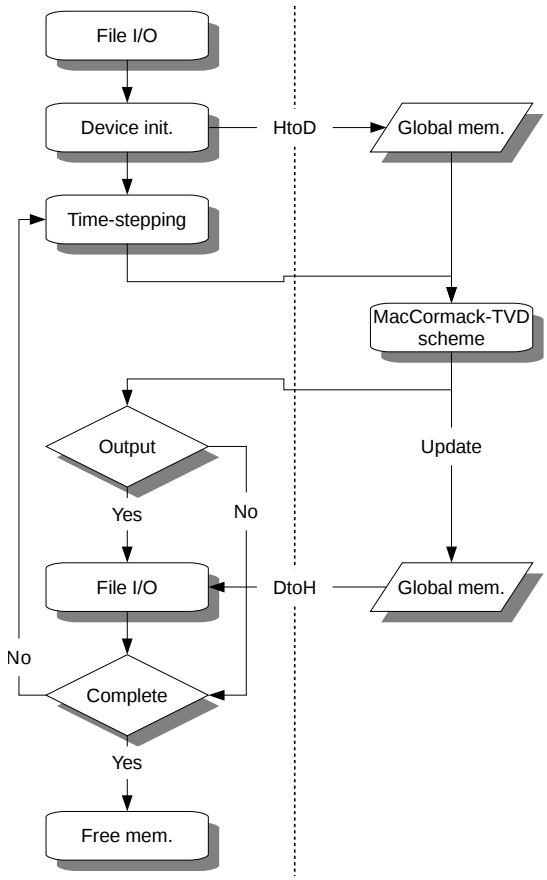

Figure 5.4: Schematic of the program control flow for the GPU optimized version of DIVAST-TVD. Items on the left are run on the host, while items on the right are run on the device. The abbreviations 'HtoD' and 'DtoH' indicate host-device and device-host memory transfers, respectively.

5.5 Case Study: Lopen Brook

The numerical modelling of riparian woodland in this chapter focuses on one case study site near Wigborough in Somerset, UK. In 2005 the Forestry Commission planted a mixture of native woodland (English oak, alder, birch, poplar, willow, etc.) on the floodplain of Lopen Brook in order to restore woodland that had previously been lost due to agriculture. The woodland covers a region of roughly 5 ha at a planting density of 3 m by 2 m (equivalent to 1,666 trees ha^{-1}). The location of the case study site is shown in Fig. 5.5 and the planning document for the plantation is given in Fig. B.1.

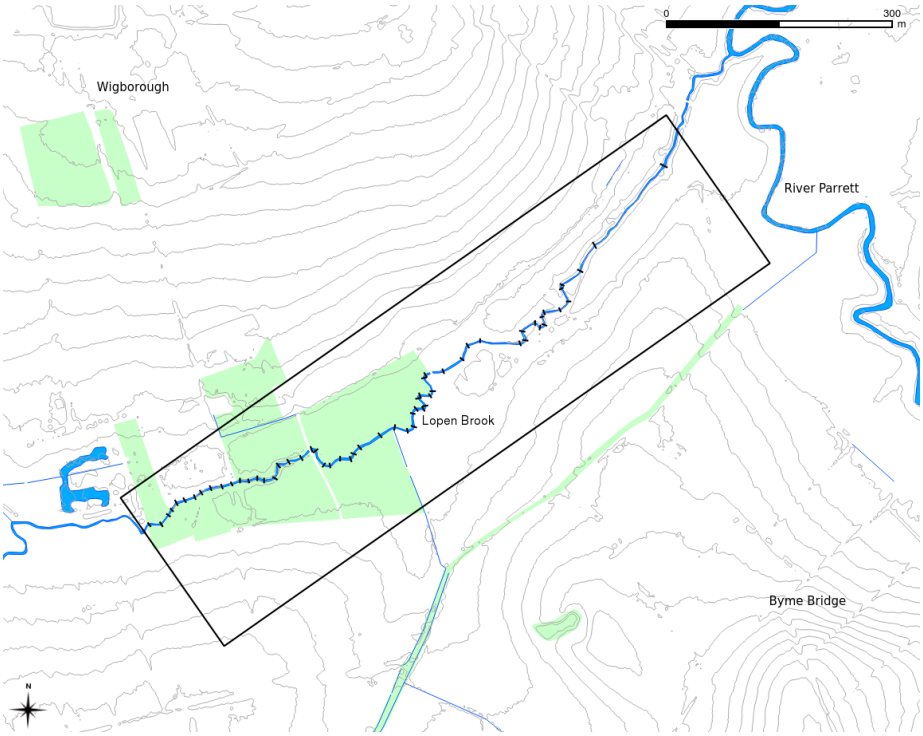

Figure 5.5: Location of the case study site with the modelling domain contained within the rectangle. Green areas indicate woodland and the black lines on Lopen Brook show locations of survey cross-sections.

Lopen Brook flows north-east into the River Parrett, which then flows north-west and eventually discharges into the Severn Estuary at Burnham-on-Sea. The 1D model that the EA has constructed for the River Parrett does not extend as far south as Lopen Brook and therefore the River Parrett is excluded from the modelling domain in this study for lack of suitable flow and bathymetry data. However, the distance between the upstream area of interest (woodland plantation) and the downstream confluence is approximately 500 m and is sufficient to minimize any backwater effects.

The main channel of Lopen Brook varies in width from 1.5 m to 3 m, gradually increasing downstream. The bed is comprised of mud and silt with patches of gravel riffles and in-stream vegetation such as sedges. The banks are relatively steep and covered in grasses and other underbrush. A typical channel cross-section is shown in Fig. 5.6.

During visits to the site in 2012 and 2013 the general characteristics of the trees within the floodplain woodland were assessed. The trees were predominantly singe-stemmed with the height at which they begin to branch typically dependent on their species, but generally ranging from 1 m to 4 m. The range in tree height was similarly dependent on species, with the poplar being approximately 8 m in height and the alder roughly 3 m tall. The average main-stem diameter at chest height ($\approx$ 1 m) was determined from a selection of 20 representative trees and was 64.7 mm (σ = 11.2 mm). The floodplain itself consists mainly of wild and grazed grass, with clusters of denser underbrush such as nettles and brambles. A photograph of the woodland on the left-hand floodplain is provided in Fig. 5.7.

Figure 5.6: Typical channel cross-section for the upper section of Lopen Brook, looking upstream.

Figure 5.7: View of the woodland on the left-hand floodplain of Lopen Brook, looking downstream. Photograph taken on the 5th June 2013.

5.5.1 Digital Elevation Model

The creation of a digital elevation model (DEM) for the Lopen Brook site was split into three parts: collection of channel bathymetry; processing of remotely sensed ground elevation data; and stitching of the channel bathymetry into the ground elevation data.

Channel Bathymetry

The channel bathymetry for Lopen Brook was collected during May and June of 2013, in conjunction with Huw Thomas of Forest Research. A total of 62 cross-sections were surveyed using a digital level and levelling staff. Elevation measurements were taken at intervals of roughly 10 cm along each cross-section, providing good resolution of channel features. The upstream and downstream boundary cross-sections for the modelling domain are presented in Fig. 5.8.

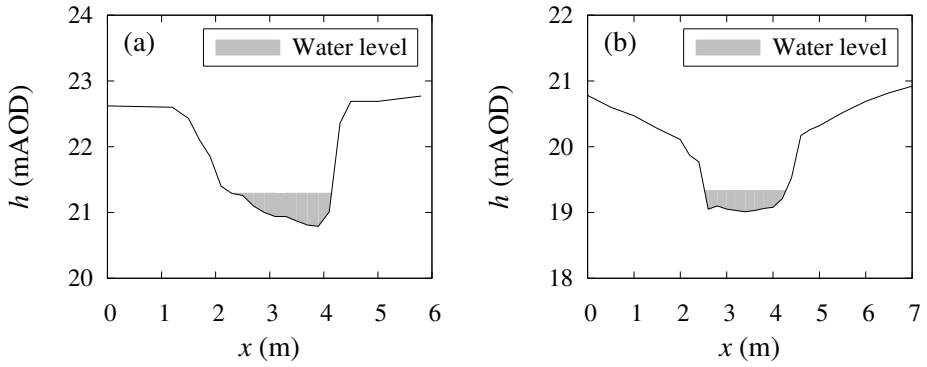

Figure 5.8: Surveyed cross-sections: (a) upstream boundary; (b) downstream boundary. Shaded areas show water levels at time of channel survey.

The cross-sections were surveyed at a denser spacing at the upstream end of the reach where the floodplain woodland plantations are located. Towards the lower-third of the reach, the channel becomes straighter and more uniform in shape. Therefore, the density of cross-sections at the downstream end was reduced accordingly. The streamwise distance between each cross-section varied from 3.9 m to 139 m, with an average of 18.4 m. In addition to the channel bathymetry, the water level at each cross-section was also recorded. The channel

thalweg and water level long profiles are plot in Fig. 5.9 (x_s is the streamwise distance).

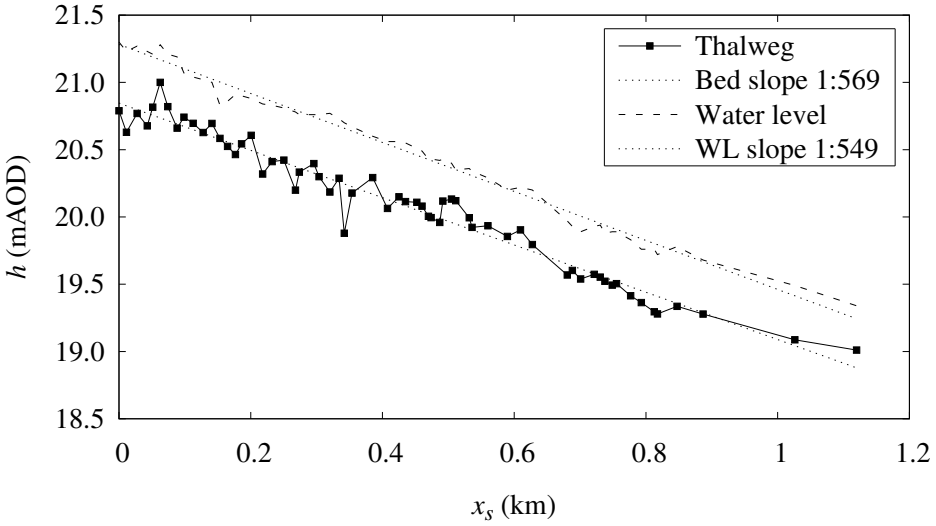

Figure 5.9: Long profile for Lopen Brook survey data. Points show locations of individual cross-sections.

LiDAR Data

Light Detection and Ranging (LiDAR) is an airborne mapping technique, which uses a laser to measure the distance between the aircraft and the ground. Up to 100,000 measurements per second are made of the ground, allowing highly detailed terrain models to be generated at spatial resolutions of between 25 cm and 2 m. The LiDAR data used in this study was provided by the Environment Agency (EA) and covered an area of 2 km by 2 km at a resolution of 2 m, with a vertical accuracy of ±5–15 cm. The data is referenced using the British National Grid OSGB36 and all elevations are given in metres above Ordnance Datum Newlyn.

Both the Digital Surface Model (DSM) and Digital Terrain Model (DTM) were available. The DTM was selected as the basis for the DEM since it represents the true ground elevation, while the DSM represents the surface elevation, including objects such as vegetation and buildings.

Before incorporating the channel bathymetry into the LiDAR data, the DTM was processed to prepare it for use in the hydrodynamic model. Firstly, the DTM was cropped to enclose the area of interest (i.e. Lopen Brook; see Fig. 5.5). A rectangular region roughly 21.5 ha in area and angled at 35° to the horizontal was chosen as the domain extent. This minimized the domain size and thus the computational effort. The DTM was then interpolated onto the angled grid and the resolution of the DTM was increased to 1 m so that the channel bathymetry could be resolved with greater accuracy.

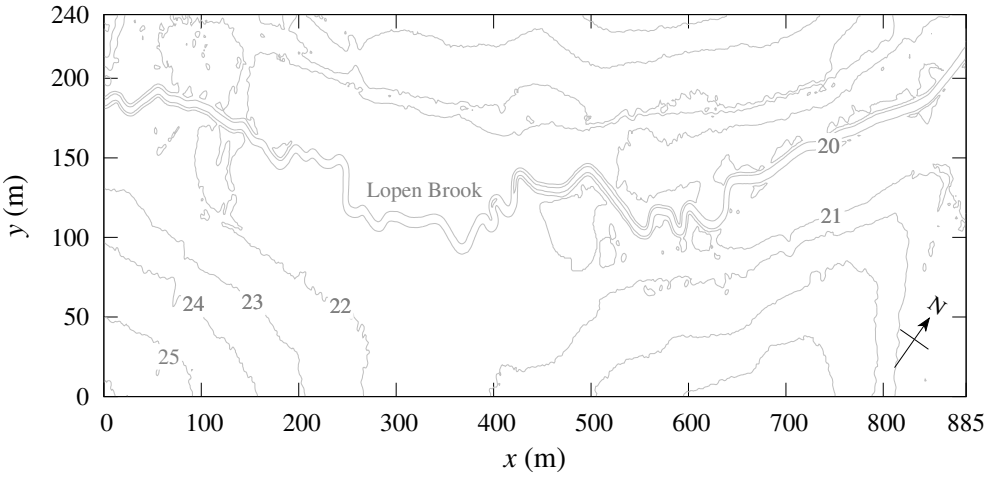

Figure 5.10: Elevation contour map for the Lopen Brook DEM. Heights are given in metres above Ordnance Datum Newlyn.

Once the DTM had been processed, the 1D channel bathymetry data was included into the DTM via a final interpolation. The resulting DEM is represented as an elevation contour map in Fig. 5.10. The total number of grid cells in the domain is 213,526. A radial basis function method was used for the interpolation operations as it provides a more stable and accurate interpolation than an inverse distance weighted approach for large, gradually varying surfaces (Eldrandaly and Abu-Zaid 2011, Forti 2012).

When interpolating cross-section bathymetry data into a grid of lower resolution, it is important to preserve the cross-sectional area of the channel. This was checked for the Lopen Brook DEM by visually inspecting the width of the channel and by comparing the long profile from the survey data (Fig. 5.9) to

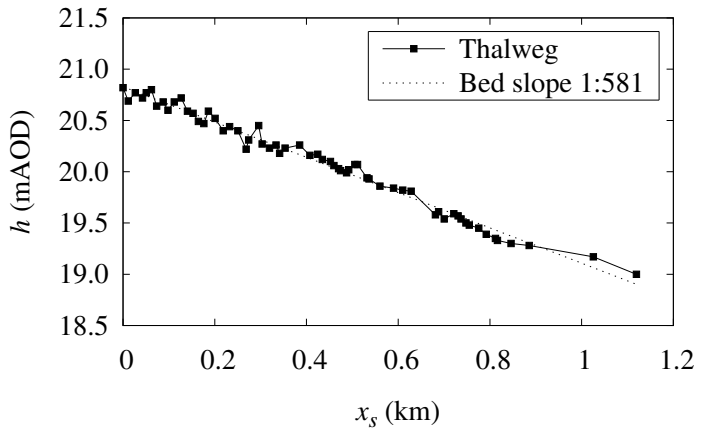

Figure 5.11: Long profile for Lopen Brook DEM. Points refer to original survey cross-section locations.

that of the DEM (Fig. 5.11). It can be seen that the DEM accurately reflects the original channel bathymetry, with only minor variations in bed slope.

5.5.2 Calibration

In order to ensure that the model properly represented the physical site, a calibration of the channel bathymetry and bed roughness was undertaken. Typically, calibration of a river model would be performed against stage-discharge data obtained from fixed gauging stations over a period of months or years. In this case, however, gauging station data was not available due to the small size of the river. Therefore, a number of in-channel flow measurements were taken manually during August 2013.

Flow Data

In total, stage-discharge data for Lopen Brook were collected at five cross-sections. The cross-sections were situated at the upstream and downstream boundaries (A & E), the two water level meter locations (B & D) and immediately upstream of the main footbridge (C). These locations are highlighted in Fig. 5.12.

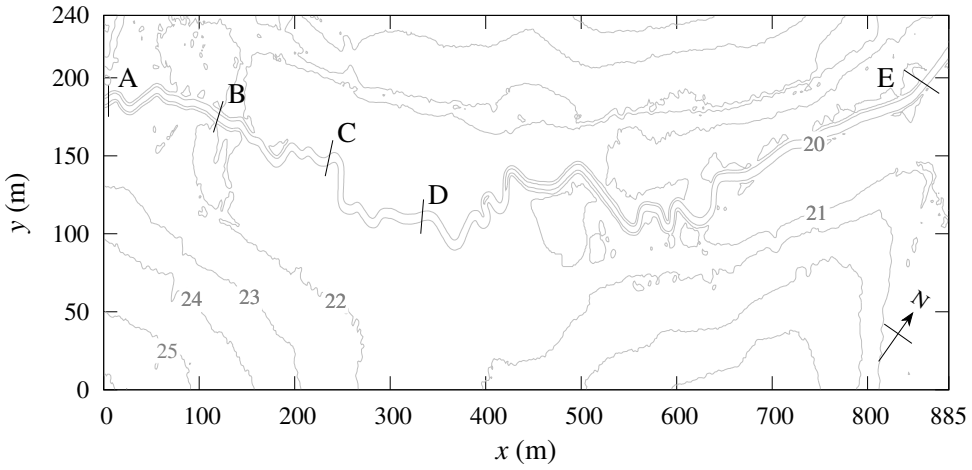

Figure 5.12: Cross-sections A–E on Lopen Brook where stage-discharge data was collected for use in model calibration.

The method to quantify the flow rate was based on the velocity-area method whereby velocities are measured at each vertical. The procedure used is as follows:

1. Stretch a measuring tape perpendicularly across the channel at the desired location.

2. Divide the cross-section into roughly 20 segments of equal width. Note that this may not be possible for smaller streams since the minimum segment width is approximately 15 cm.

3. Starting at the left-hand bank (as looking downstream), measure the depth and velocity using a propeller type velocity meter at the pre-determined widths.

4. Once the entire cross-section has been measured, the total flow rate can be calculated as the sum of the segments' flow rates.

The United States Geological Survey (USGS) velocity-area method assumes that at points where the depth is less than 2.5 ft (0.76 m), the average velocity occurs at six-tenths of the total depth. Where the stream is deeper than 2.5 ft, the velocity is measured at two-tenths and eight-tenths of the total depth, and the

average of the two readings is used as the average velocity at that point (Buchanan and Somers 1976).

The depth-velocity measurements and resulting flow rate calculations are presented in Tables B.1–B.5 for each of the five measurement cross-sections. The total flow rates varied from 0.11 $m^3 s^{-1}$ to 0.129 $m^3 s^{-1}$ with σ = 0.007 $m^3 s^{-1}$. The variation in flow rate between cross-sections is therefore relatively minor and was most likely caused by small deviations from the velocity-area method's assumption of mean velocity depth. For the following calibrations, an average flow rate of 0.12 $m^3 s^{-1}$ was used at the upstream boundary, whilst the bed roughness was modified so that the resulting depths in the model were consistent with those recorded in Tables B.1–B.5.

2D Calibration

The bed friction module within DIVAST-TVD can represent bed roughness using either Manning's n or roughness height k_s (see Eqs. 5.11–5.13). Whilst the use of Manning's n is common in hydrodynamic modelling, the bed roughness height k_s allows a more complex and physically correct analysis of bed friction to be performed (Ferguson 2010).

In order to calibrate the value of k_s for the in-channel bed roughness, the DIVAST-TVD model for Lopen Brook was run multiple times as a steady state analysis. The upstream boundary was specified as a flow rate of 0.12 $m^3 s^{-1}$ and the downstream boundary was set to a normal depth with a slope of 1:549 (i.e. the measured water surface slope; see Fig. 5.9). The channel was initially dry so each model variation was run for 12 hrs before taking water level readings. This gave the model time to achieve a steady flow state.

After each run the water levels at each of the five cross-sections was inspected and compared with the data in Tables B.1–B.5 respectively. The in-channel roughness was then modified accordingly and the model run again as iterative procedure until the depths were in agreement with the measured stage-discharge data.

The results of the 2D calibration are presented in Table 5.7. It can be seen that a roughness length of k_s = 0.025 m resulted in the closest match between

the measured and predicted water levels at each of the five cross-sections and is therefore used in the following modelling. The bed elevation and water level long profiles for the calibration where $k_s = 0.025$ m are shown in Fig. 5.13.

Table 5.7: In-channel bed roughness 2D calibration for Lopen Brook using DIVAST-TVD. The total errors ϵ were calculated as the sum of the errors between the predicted and measured water levels at each of the five cross-sections.

k_s	Cross-section WL (m AOD)					Total error	
(m)	A	B	C	D	E	ϵ_{abs} (m)	$\epsilon_{\%}$ (%)
0.01	21.063	20.842	20.591	20.268	19.25	0.186	0.91
0.025	21.09	20.866	20.601	20.295	19.274	0.076	0.37
0.05	21.122	20.87	20.619	20.323	19.31	0.104	0.51
0.075	21.144	20.873	20.626	20.35	19.339	0.186	0.91
0.1	21.189	20.889	20.633	20.406	19.355	0.294	1.44
Measured	21.1	20.9	20.6	20.3	19.3	-	-

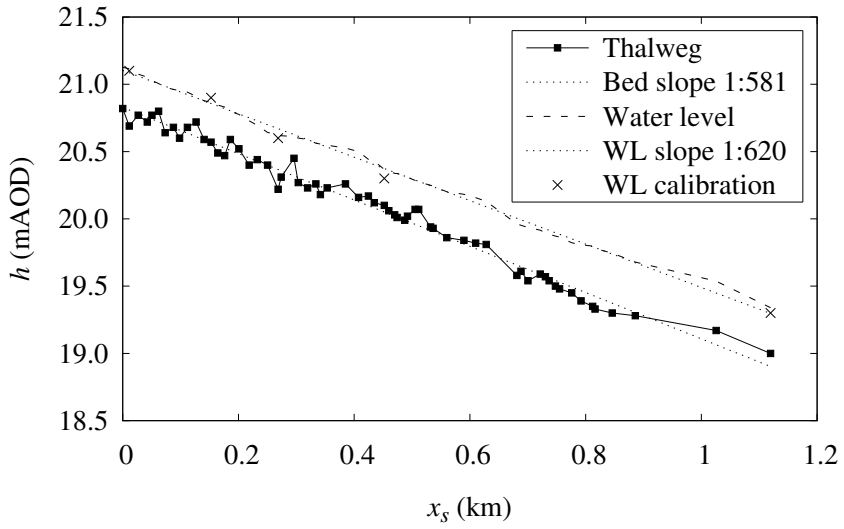

Figure 5.13: Long profile for Lopen Brook during calibration with $k_s = 0.025$ m. Points refer to original survey cross-section locations.

Unfortunately there is no data available to calibrate the roughness length of the floodplain. However, a value of $k_s = 0.075$ m is assumed to be applicable given the long grass and occasional underbrush at the site (Chow 1973; see

Figs. 5.6 and 5.7). This is consistent with field measurements of the roughness lengths for similar land cover types (Medeiros *et al.* 2012).

The maximum value for k_s is constrained by the Colebrook-White equation (5.12) and is limited to $k_s < 12\zeta_{\min}$, where $\zeta_{\min}$ is the minimum depth allowed during the simulation. In this study, $\zeta_{\min} = 0.01$ m and thus both the in-channel and floodplain roughness lengths satisfy the restriction of $k_s \leq 0.12$ m.

5.5.3 Boundary Conditions

Upstream

In the absence of gauging station data for Lopen Brook, a Revitalized Flood Hydrograph (ReFH) model was run for the catchment to generate flood hydrographs with return periods of 5 to 500 years (Fig. 5.14). The ReFH model is based on robust hydrological modelling techniques and is considered to be an improvement over the standard Flood Estimation Handbook (FEH) model (Kjeldsen *et al.* 2005).

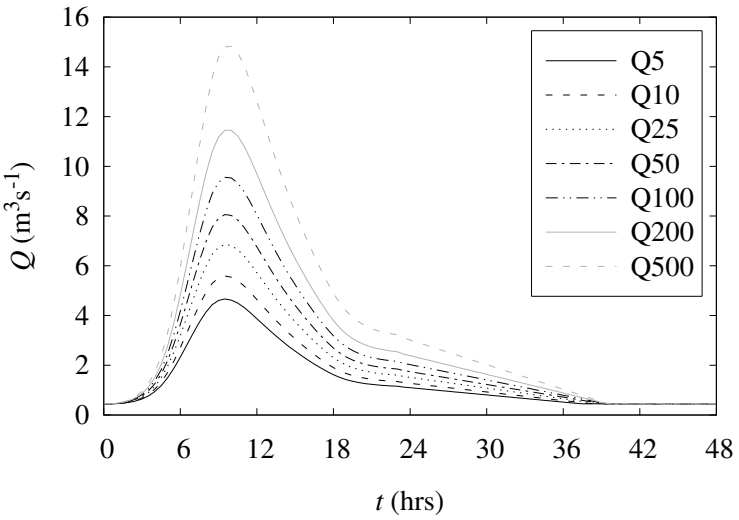

Figure 5.14: Flood hydrographs for Lopen Brook.

The catchment area used in the ReFH analysis was 18 km^2, while the rainfall duration was 9.5 hrs. The time to peak was 3.76 hrs and the base discharge was 0.45 m^3 s^{-1}. The model was run with the upstream boundary set to the base

discharge as a steady state analysis for 12 hrs so that initial water levels and flow rates could be determined for use in the following simulation scenarios.

Downstream

No special treatment of the downstream boundary was required and it was therefore set to an open type boundary where the fluid can flow freely in and out of the domain. This was achieved by setting a zero gradient for the water elevation and flow rates (i.e. $\partial\eta/\partial m = \partial q/\partial m = 0$ where m is the direction normal to the outlet plane).

5.6 Results & Discussion

The data from the previous section are now used to perform a number of modelling scenarios to investigate the hydraulic impact of the floodplain woodland at Lopen Brook. Initially, the flood is allowed to propagate across an empty floodplain without woodland so that baseline flood properties can be determined. This also allows the impact of the choice of bed roughness parameterization (i.e. with or without Reynolds number effects) to be discussed. The model is then run for an additional four different scenarios: the existing woodland; replacing the existing woodland with short rotation coppice; expanding the woodland areas to cover the whole floodplain; and a mix of woodland and floodplain storage.

5.6.1 Scenario 1: No Woodland

To run the first scenario, the woodland areas are removed and the cells set to open floodplain. The model is then run twice for each input flood hydrograph (Q1 to Q100), with the Chezy coefficient switching from including (Eq. 5.13) or excluding (Eq. 5.12) Reynolds number effects. Each model is run for a total simulated time of 48 hrs, which allows the whole domain to reach a steady state after the flood peak has passed. Hereafter, the models utilizing Chezy numbers that include or exclude Reynolds number effects shall be denoted C_{Re} and C_{ζ}, respectively.

Before discussing the differences between the C_{Re} and C_{ζ} cases, the general flood propagation properties are first described. Taking the flood with the lowest modelled return period (Q5), it can be seen from Fig. 5.15 that the water initially spills over from the main channel onto the downstream floodplain ($t \approx 6$ hrs). After eight hours, patches of the upstream reach also begin to become inundated on both the left and right floodplains. The maximum overland flow depths occur just after the flood peak has passed ($t \approx 12$ hrs). The inundation extent at the downstream reach is limited by the comparatively steep valley walls that run parallel to the main channel. The upstream reach, however, is not fully flooded for the Q5 return period, indicating that there is significant additional flood storage capacity given the relatively flat gradient of the floodplain at this point.

The mode of flood propagation for the Q100 return period (Fig. 5.16) is similar to that of the Q5 flood. The main differences are that the water overflows onto the downstream floodplain earlier ($t \approx 5$ hrs) and that the depths on the floodplain are greater. The flood also extends to cover a much larger area of the upstream floodplain. It should be noted that in all of the modelled flood return periods (Q5–Q100) standing water remains on both the upstream and downstream floodplains due to the slightly raised banks of the main channel.

The effect of the flow over-topping from the main channel onto the floodplain can be seen in Fig. 5.17. The hydrographs at the downstream boundary show that the flood peak is delayed by 1 hr and reduced by 17.3% to 23.2%. The greatest reduction in peak flood flow at the downstream boundary occurred during the Q100 flood, while the least reduction was observed for the Q5 flood. This is to be expected since the main channel will be able to carry proportionally less of the flow during a larger flood, thus forcing more water out onto the floodplains.

The total inundation area A_i for each modelled flood return period is presented in Fig. 5.18. It can be seen that the difference in inundation area between the lower return periods (Q5–Q10) is greater than that at the higher return periods (Q50–Q100). This is due to the upper-reach floodplain, which remains relatively dry during the Q5 flood (see Fig. 5.15), becoming increasingly inundated during the Q10 and Q25 floods. For the Q50 and Q100 return periods, the floodplain flows become deeper rather than expanding since they are constrained by the valley sides.

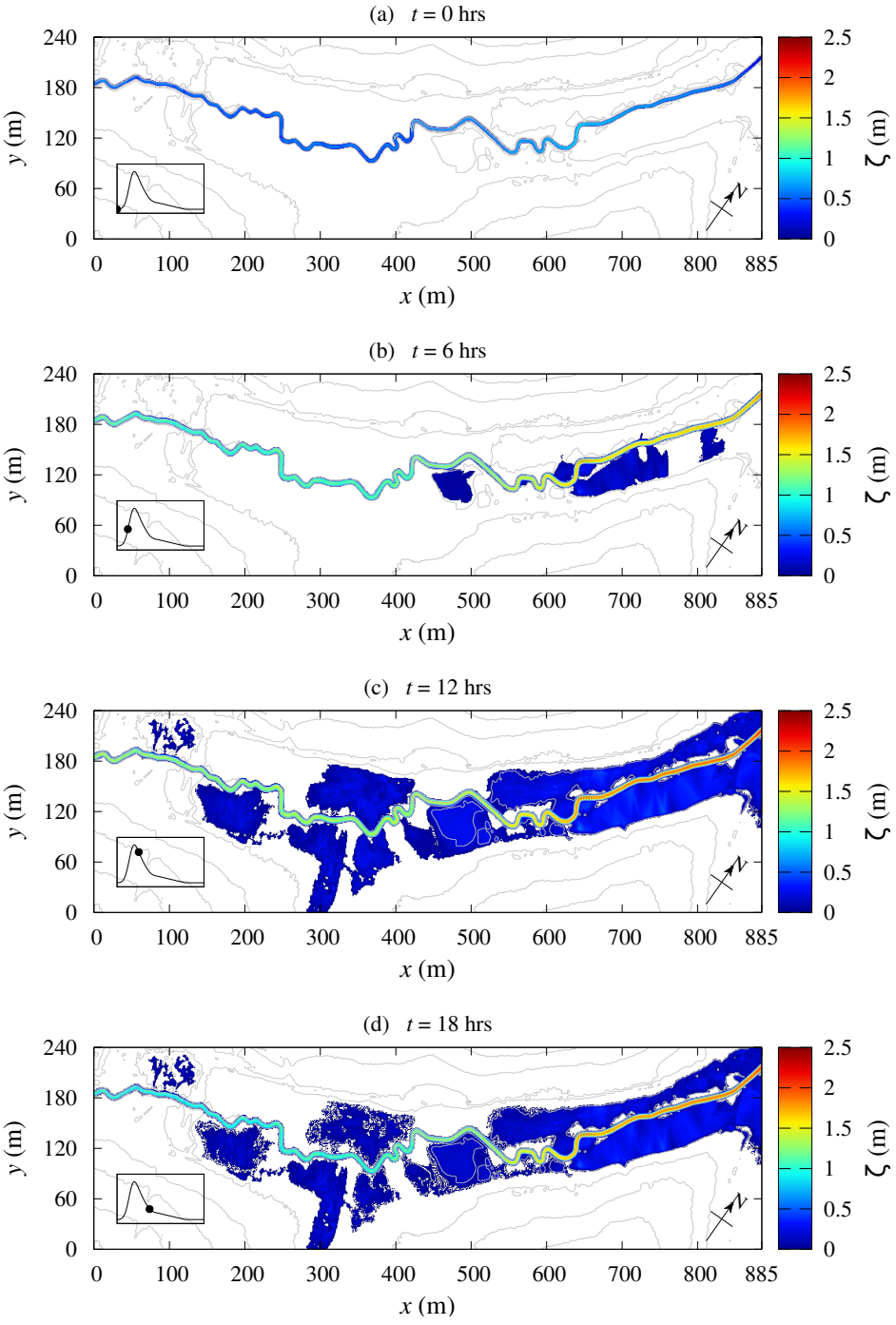

Figure 5.15: Flood propagation at Lopen Brook for a Q5 flood. Flow depths shown at: (a) $t = 0$ hrs; (b) $t = 6$ hrs; (c) $t = 12$ hrs; and (d) $t = 18$ hrs.

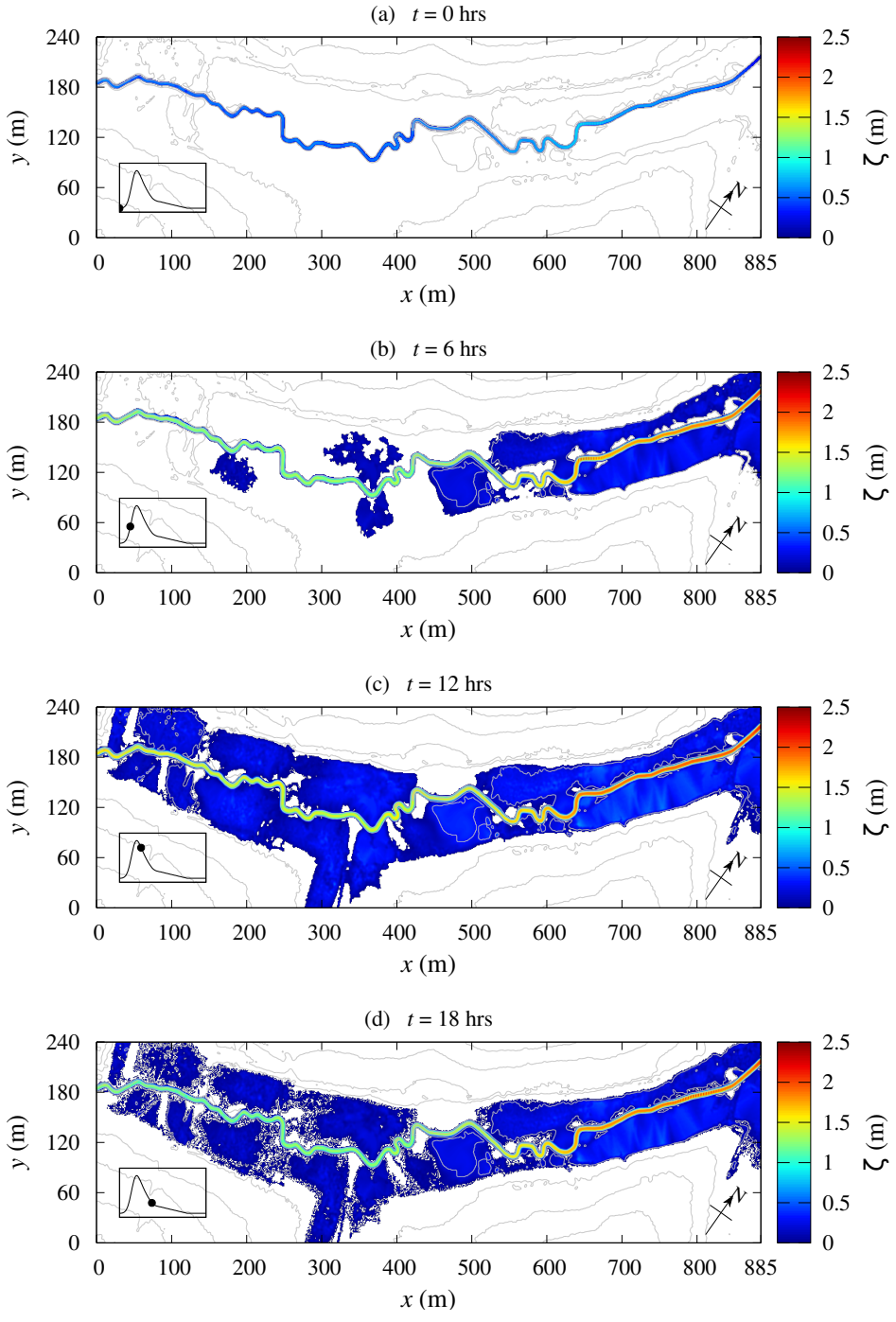

Figure 5.16: Flood propagation at Lopen Brook for a Q100 flood. Flow depths shown at: (a) $t = 0$ hrs; (b) $t = 6$ hrs; (c) $t = 12$ hrs; and (d) $t = 18$ hrs.

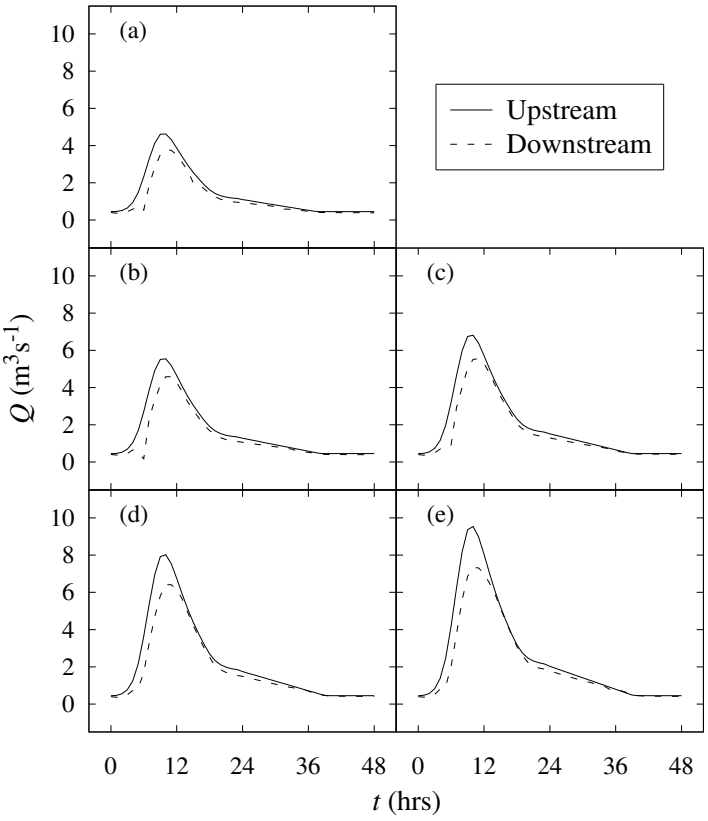

Figure 5.17: Upstream and downstream flood hydrographs for Lopen Brook in Scenario 1: (a) Q5; (b) Q10; (c) Q25; (d) Q50; and (e) Q100.

The differences in inundation area between the C_{Re} and C_{ζ} cases for each return period are also labelled in Fig. 5.18. There appears to be no correlation with return period, but the magnitudes of the differences indicate that the inundation areas are virtually identical between the two cases at each return period. Comparing the flood velocities and bed shear stress from the C_{Re} and C_{ζ} cases results in a similar lack of differentiation.

To illustrate the relative impact of including or excluding Reynolds number effects in the bed friction calculation, the variation in bed shear stress with flow Reynolds number is plot in Fig. 5.19. As expected, the bed shear stresses become independent of Reynolds number effects at the onset of fully developed turbulent flow ($2000 < Re < 4000$). Below this limit the bed shear stresses diverge slightly,

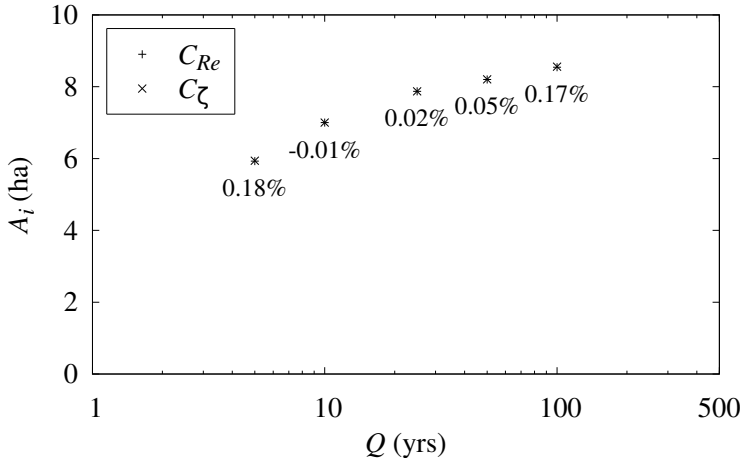

Figure 5.18: Total inundation area at each return period for the C_{Re} and C_ζ cases in Scenario 1. The percentage difference between the C_{Re} and C_ζ cases is also labelled.

with those calculated using a Chezy value incorporating Reynolds number effects being marginally greater than those without. However, this variation is essentially negligible since while the percentage difference may be large, the magnitude of the deviation is minor. For example, at the most reasonable extreme case of $\zeta = 0.5$ m and $Re = 10^3$ ($U = 6.5 \times 10^{-4}$ m s^{-1}), the bed shear stresses with and without Reynolds number effects are $\tau_b = 4.52 \times 10^{-6}$ N m^{-2} and $\tau_b = 3.53 \times 10^{-6}$ N m^{-2}, respectively.

Therefore, it is recommended that Reynolds number effects be neglected in the determination of the bed friction on a vegetated floodplain due to the higher computational cost and negligible impact on flood characteristics. Reynolds number effects may play a larger role in determining the bed friction in models where the flow depth is greater and the bed is smoother, e.g. tidal estuaries or lagoons.

5.6.2 Scenario 2: Existing Woodland

The second scenario introduces the woodland planted by the Forestry Commission in 2005, which is modelled using the vegetative drag force and porosity terms described in Eqs. (5.14) and (5.15) respectively. The woodland area is shown in

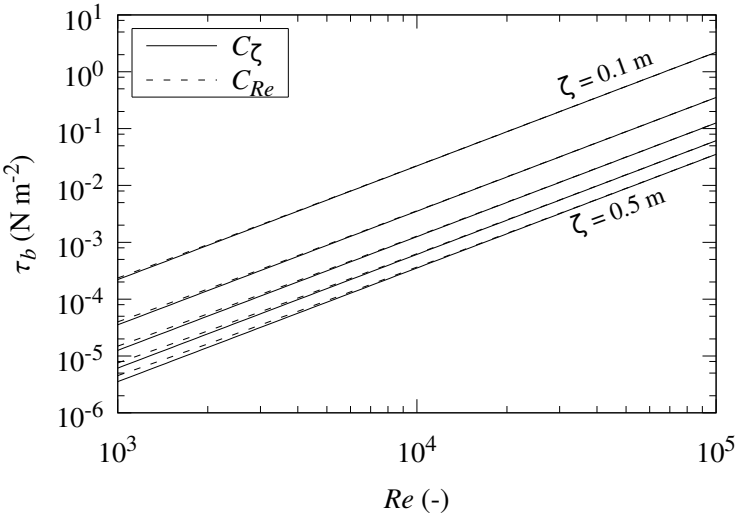

Figure 5.19: Bed shear stress calculated using Chezy values derived with and without Reynolds number effects for a range of typical flow depths on Lopen Brook floodplain. The floodplain roughness was set to $k_s = 0.075$ m.

Fig. 5.20 and covers a region of roughly 5 ha at a planting density of 3 m by 2 m (equivalent to 1,666 trees ha^{-1} or $N = 0.1667$ m^{-2}).

The woodland at Lopen Brook is comprised of native species, such as English oak, poplar, willow, birch and alder. A mix of the three species from this study (common alder, black poplar and white willow; see § 3.2.1) is therefore used in the model. This was done by randomly assigning one of the three species to each domain cell within the woodland area.

The drag forces were modelled using the Cauchy reconfiguration model (Eqs. 4.5 and 4.8), which required the trees' heights H (Table 3.2), main-stem flexural rigidities EI (Table 3.3), rigid drag coefficients C^*_{d0} (Table 4.1), and Vogel exponents ψ (Table 3.8). The variation in projected area A_{p0} with depth for each species is discretized using the species-averaged sigmoid functions in Table 3.16. The trees' average mid-stem diameter ($d = 64.7$ mm), as measured from the site survey (see § 5.5), was used as the equivalent cylinder diameter in the porosity calculation (Eq. 5.15).

The model was run with the same topography and boundary conditions as for Scenario 1, with the addition of the drag force and blockage effect within

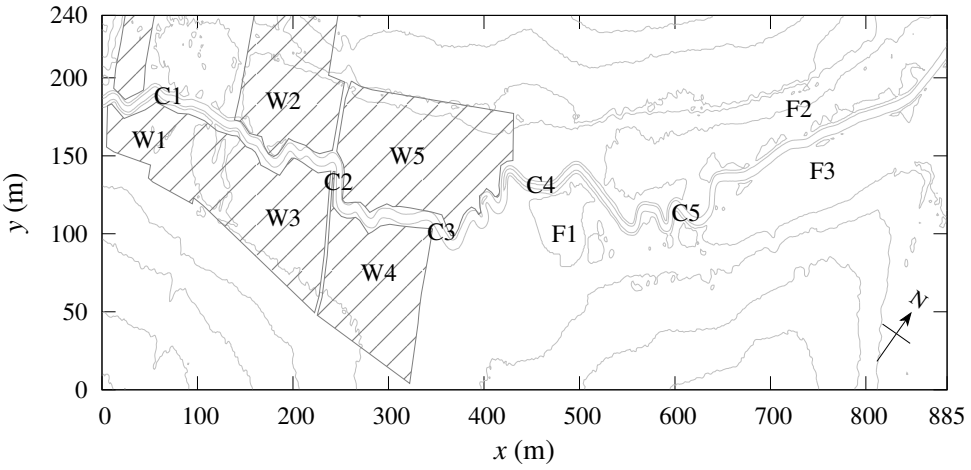

Figure 5.20: Model monitoring points, split into: in-channel (C); woodland (W); and downstream floodplain (F) locations. The woodland extent is marked by the shaded areas.

the woodland areas. The inundation areas for each of the flood return periods (Q5–Q100) are compared to those from Scenario 1 in Fig. 5.21. It is evident that while the woodland does reduce total inundation area for each of the return periods, the overall effect is very minor (0.03% to 0.44%).

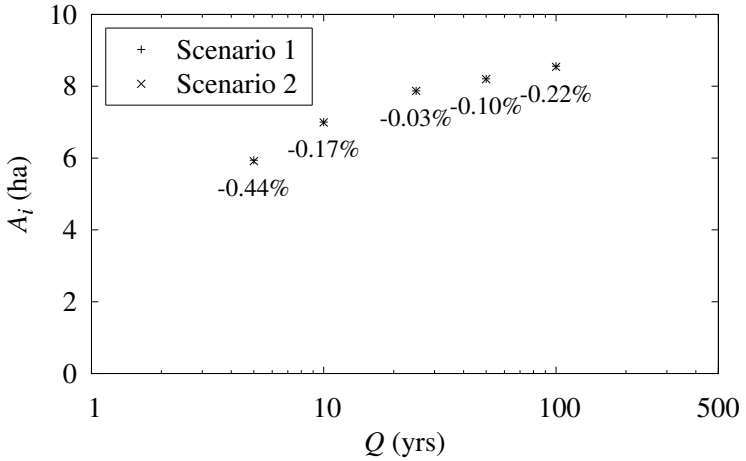

Figure 5.21: Total inundation area at each return period for Scenarios 1 and 2. The percentage difference between the scenarios is also labelled.

Similarly, the woodland had a negligible impact on the downstream flood

hydrograph. This is due to a combination of the low planting density and the topography of the case study site. The Lopen Brook floodplain can be split into upstream ($x < 400$ m) and downstream ($x > 400$ m) sections, where only the main channel conveys flow between the two (see Fig. 5.15c). As previously discussed, the main channel banks are slightly raised and the flood water does not fully drain from the floodplains. Therefore, the increased resistance provided by the woodland on the upper reach does not translate to a reduction or delay in peak flood flows at the downstream boundary.

While the introduction of floodplain woodland in the current configuration may not result in a noticeable change to the flood hydrograph, it is expected that there will be a reduction in flow velocities within the vegetated areas. In order to capture the effects of the woodland on the flow properties, a number of monitoring points are chosen for further inspection. The exact locations of the points are shown in Fig. 5.20 and they can be split into three groups: five points within the main channel (C1–C5); five points within the woodland area (W1–W5); and three points on the downstream floodplain (F1–F3).

For brevity, the data for the Q5–Q50 floods are not discussed herein since they are similar in pattern to the Q100 flood. The variation in flow properties at each of the monitoring points over the duration of a Q100 flood is presented in Fig. 5.22. It can be seen that around 5 cm to 20 cm of water is left standing on the upstream floodplain, while the downstream floodplain is more inundated with 10 cm to 30 cm of water remaining once the flood peak passes.

The velocities within the main channel rise and fall in a similar manner to the flood hydrograph, as might be predicted. On the other hand, the velocities at the woodland monitoring locations show that the water on the upstream floodplains is only flowing during the initial over-topping and expansion period. The monitoring points on the downstream floodplains show a mixture of the two behaviours, with the flow on the right floodplain (F3) travelling at approximately the same velocity as the main channel for $t > 24$ hrs.

A comparison of the flow properties at each of the monitoring points for a Q100 flood between the current scenario and Scenario 1 is provided in Table 5.8. Both the differences between the simulation-average and maximum values are calculated, with negative values indicating a reduction from Scenario 1. Overall

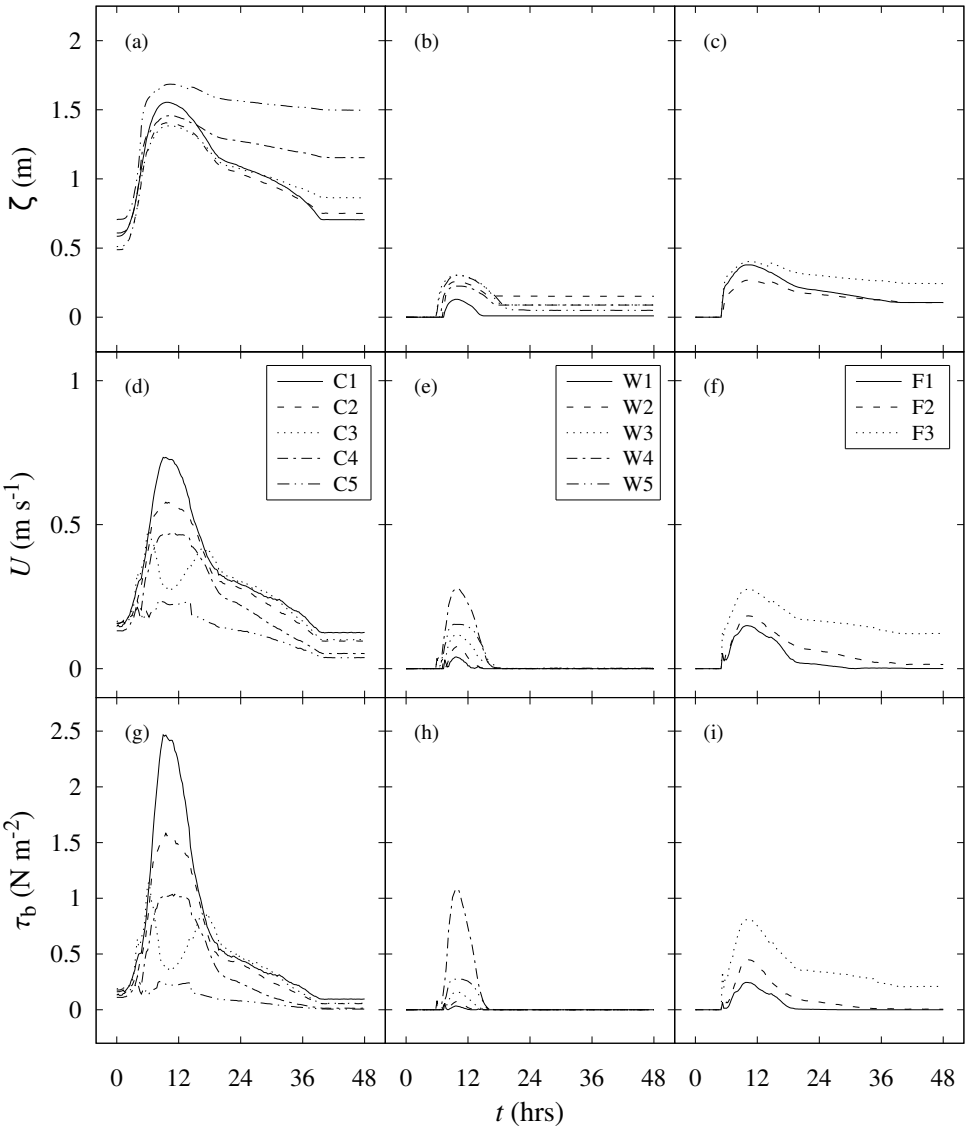

Figure 5.22: Flow depths, velocities and bed shear stresses for Scenario 2 during a Q100 flood at each of the model monitoring points: in-channel C1–C5 (a,d,g); woodland W1–W5 (b,e,h); and downstream floodplain F1–F3 (c,f,i).

there is a decrease in nearly every flow property at each of the monitoring sites. However, the magnitude of the reductions for the in-channel and downstream floodplain locations are essentially negligible, with all but two reductions being less than 1%.

The reduction in velocities and bed shear stresses within the woodland areas is more significant. For example, the peak velocities at points W1–W5 are decreased by up to 4.02%, with similar reductions for the average velocities. The peak bed shear stresses at the same points are reduced by up to 13.8% and the average stresses are reduced by up to 12.3%. The flow depths within the woodland areas are much less sensitive, only decreasing by a maximum of 0.77%. The bed shear stress is more strongly affected by the vegetation since it is dependent on the flow velocity and wetted bed area, both of which are modified by its presence.

Table 5.8: Differences in average and maximum flow properties between Scenarios 1 and 2 for a Q100 flood. Monitoring point locations are split into in-channel (C), woodland (W) and downstream floodplain (F) areas.

Location	$\Delta\zeta_{\text{avrg}}$ (%)	$\Delta\zeta_{\text{max}}$ (%)	ΔU_{avrg} (%)	ΔU_{max} (%)	$\Delta\tau_{b_{\text{avrg}}}$ (%)	$\Delta\tau_{b_{\text{max}}}$ (%)
C1	0.01	−0.06	0.02	0.24	0.02	0.5
C2	−0.02	0	−0.04	−0.05	−0.19	−0.04
C3	−0.04	−0.07	−0.06	−0.99	−0.27	−2.04
C4	−0.01	−0.07	−0.03	0	−0.06	−0.03
C5	0	0	−0.05	−0.35	−0.07	−0.97
W1	−0.28	−0.77	0.35	−1.7	−0.44	−2.88
W2	−0.19	−0.77	−2.73	−4.02	−12.26	−13.76
W3	−0.67	−0.33	−4.89	−1.42	−12.04	−9.25
W4	−0.06	−0.44	−0.09	−0.29	−5.79	−5.36
W5	−0.17	−0.66	−1.25	−2.21	−10.06	−10.15
F1	−0.04	−0.26	−0.44	−0.65	−0.64	−1.36
F2	−0.06	−0.37	0.02	−0.29	−0.02	−0.73
F3	−0.02	0	−0.02	−0.24	−0.04	−0.36

5.6.3 Scenario 3: Short Rotation Coppice

Although the results from the second scenario suggest that increasing the resistance of the upstream floodplain has little effect on the downstream flood hydrograph, the woodland none-the-less reduced local flow velocities and bed

shear stresses. To further investigate this phenomenon, the native woodland is replaced by short rotation coppice (SRC), which is typically planted at much greater densities and therefore imposes more resistance to the flood flow.

The establishment of willow and poplar SRC plantations has more in common with agriculture than forestry. The land is initially ploughed and prepared before planting and, in the UK, the first season's growth is cut back to encourage production of more shoots the following year. The trees are then harvested at periods of 2 to 4 years using specialized machinery. Several of these 2 to 4 year cycles can take place before the crop needs to be replaced due to declining yields.

The wood from SRC is generally used as a low carbon energy source, with the main benefits being a reduced demand for chemical inputs and maintenance when compared to conventional arable crops and an enhancement to local biodiversity (Tubby and Armstrong 2002). Further, it has been shown that SRC may play an important hydrological role in reducing flood risk by reducing water yields up to 50% when planted in place of grass or arable crops (Hall *et al.* 1996). As a result of the high water uptake, SRC can also help tackle nitrate and other diffuse pollution (Elowson and Christersson 1994).

The optimal planting density and harvesting frequency of SRC was examined by Bullard *et al.* (2002). The authors considered the yield from planting densities of 8,625 to 111,000 trees ha^{-1} and found that a density of 15,625 trees ha^{-1} provided the best economic return over the SRC's lifetime. Defra (2004) state that the current best practice for commercial willow SRC crops is a planting pattern consisting of rectangular grids with 0.75 m by 0.59 m spacing and 1.5 m between each twin row for access. This equates to 15,000 trees ha^{-1} ($N = 1.5$ m^{-2}) and, therefore, the same density will be used in this scenario. The SRC are modelled using the same parameters as for the willow trees in the previous scenario, with the exception that the species-specific drag coefficient is raised slightly to $C_{d\chi} = 1.5$ to account for the multi-stem nature of coppiced trees.

The model is run again using the same topography and boundary conditions as for the first scenario. For brevity, only the Q100 flood is discussed herein since the lower flood return periods follow a similar pattern. As predicted, the increased upstream floodplain resistance has a negligible impact on the hydrograph compared to the first scenario. The total inundation area also remains

relatively constant, with the inundation area for the Q100 flood being only 0.06% less than Scenario 1.

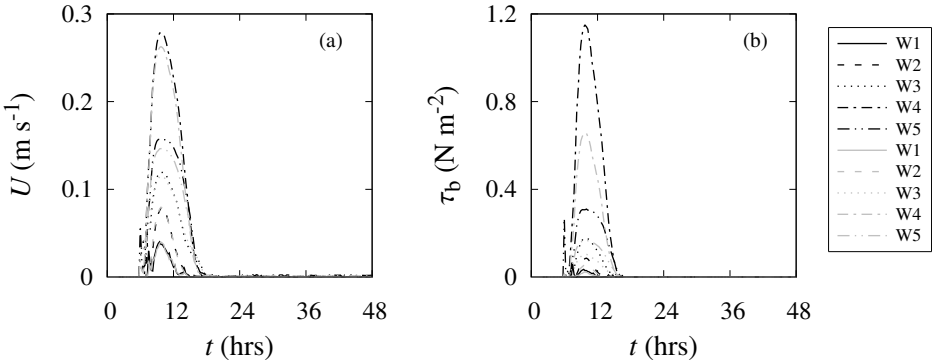

Figure 5.23: Comparison of velocities (a) and bed shear stresses (b) for a Q100 flood between Scenarios 1 (black) and 3 (grey) at each of the woodland monitoring points.

The dense planting pattern for the SRC does, however, have a significant impact on the velocities and bed shear stresses within the woodland areas (Fig. 5.23). From Table 5.9 it can be seen that the average and maximum velocities are reduced by up to 10.9% and 7.1%, respectively. The in-channel and downstream floodplain values are omitted from Table 5.9 as there are very similar to those from the second scenario (Table 5.8).

Table 5.9: Differences in average and maximum flow properties between Scenarios 1 and 3 for a Q100 flood at each of the woodland monitoring points.

Location	$\Delta\zeta_{\text{avrg}}$ (%)	$\Delta\zeta_{\text{max}}$ (%)	ΔU_{avrg} (%)	ΔU_{max} (%)	$\Delta\tau_{b_{\text{avrg}}}$ (%)	$\Delta\tau_{b_{\text{max}}}$ (%)
W1	0.18	0.77	−6.72	−1.08	−46.08	−60.77
W2	−0.62	0.77	−2.88	−0.08	−37.5	−36.13
W3	−1.57	0.33	−0.15	−3.68	−38.14	−41.68
W4	0.43	0.88	−7.28	−5.68	−43.27	−42.73
W5	0.5	0.98	−10.99	−7.1	−49.29	−46.16

The lower velocities in the floodplain woodland areas result in greatly reduced bed shear stresses, with the average and maximum bed shear stresses decreasing by up to 53.6% and 64.1%, respectively. The reduction is particularly

visible at point W4 in Fig. 5.23, where the peak bed shear stress is reduced from approximately 1.15 $\mathrm{N\,m^{-2}}$ to 0.65 $\mathrm{N\,m^{-2}}$.

5.6.4 Scenario 4: Woodland Expansion

The previous scenarios have shown that the addition of riparian woodland at Lopen Brook can have a significant impact on local flow properties, namely velocity and bed shear stress. However, these effects remain localized and the downstream flow is essentially unaffected. Therefore, the current scenario expands the SRC from the previous scenario so that the entire floodplain is covered (Fig. 5.24). This assumes that the full area is suitable for planting, but will none-the-less provide a model for the maximum impact that SRC can achieve at this site.

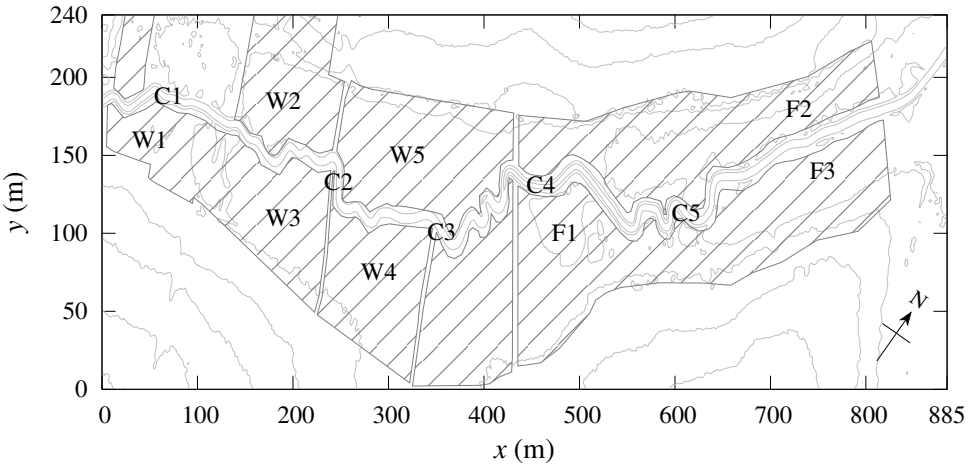

Figure 5.24: Expansion of the SRC (shaded areas) to cover the entire floodplain at Lopen Brook. Model monitoring points are split into: in-channel (C); original woodland (W); and downstream floodplain (F) locations.

The model is run again using the same topography and boundary conditions as for the previous scenarios. For brevity, only the Q100 flood is discussed herein since the lower flood return periods follow a similar pattern. The addition of the SRC onto the downstream floodplain has a negligible impact on the downstream flood hydrograph for the Q100 case when compared to the first scenario (Fig. 5.25). The total inundation area is similarly insensitive and is only 0.06%

greater than for Scenario 1. The minor increase in total inundation area is most likely a result of raised water levels due to the blockage effect of the SRC.

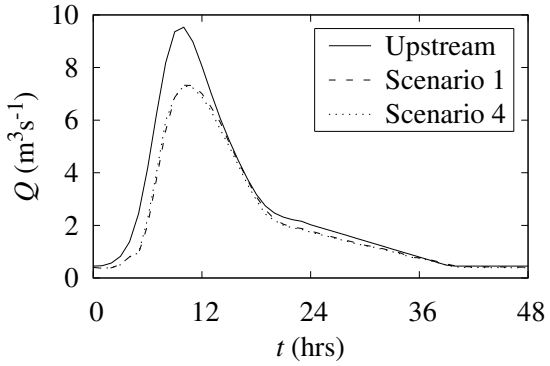

Figure 5.25: Downstream flood hydrographs during a Q100 flood for Scenarios 1 and 4.

Indeed, when comparing the flow depths at each of the monitoring points to those of the first scenario, it can be seen that the average and maximum flow depths at the upstream and downstream woodland locations are around 1% to 2% greater (Table 5.10). As might be expected, the most notable effect of the additional SRC is a reduction in the flow velocities and bed shear stresses on the downstream floodplain. For these points, Table 5.10 reports that the average and maximum velocities are reduced by 13.6% and 10.5%, respectively, while the average and maximum bed shear stresses are decreased by up to 51.5% and 49.4%, respectively.

The evolution of the flow velocities and bed shear stresses at the downstream floodplain monitoring locations is presented in Fig. 5.26. The reduction in values compared to the first scenario is particularly evident at points F2 and F3 (see Fig. 5.24). This is because these points are located towards the end of the downstream reach, where the flood water has been significantly retarded by the SRC as it flows parallel to the main channel.

It can also be seen from Table 5.10 that the expansion of the SRC to cover the entire floodplain has reduced the velocities and bed shear stresses within the main channel, especially towards the downstream boundary (points C3 to C5). This is in contrast with the previous scenario where the SRC was confined to the extent

Table 5.10: Differences in average and maximum flow properties between Scenarios 1 and 4 for a Q100 flood. Monitoring point locations are split into in-channel (C), woodland (W) and downstream floodplain (F) areas.

Location	$\Delta\zeta_{\text{avrg}}$ (%)	$\Delta\zeta_{\text{max}}$ (%)	ΔU_{avrg} (%)	ΔU_{max} (%)	$\Delta\tau_{b_{\text{avrg}}}$ (%)	$\Delta\tau_{b_{\text{max}}}$ (%)
C1	−0.3	0	−0.7	−0.56	−0.69	−1.08
C2	−0.21	0.07	−0.66	−0.6	−0.65	−1.27
C3	−0.08	0.07	−1.25	−3.11	−2.17	−5.66
C4	0.14	0.14	−1.76	−1.89	−3.28	−3.81
C5	0.3	0.36	−2.5	−3.41	−4.26	−7.16
W1	0.03	0.77	−7.43	−7.06	−48.51	−65.1
W2	0.67	0.77	−2.77	−0.28	−37.23	−36.89
W3	0.98	0.33	−0.03	−2.69	−37.38	−40.67
W4	0.51	0.88	−7.22	−5.61	−43.12	−42.75
W5	0.72	0.98	−10.7	−6.89	−49.18	−46.04
F1	0.71	0.53	−1.91	−3.25	−35.42	−33.35
F2	2.34	1.12	−13.65	−10.53	−51.49	−49.42
F3	1.02	0.75	−10.14	−7.98	−48.92	−47.36

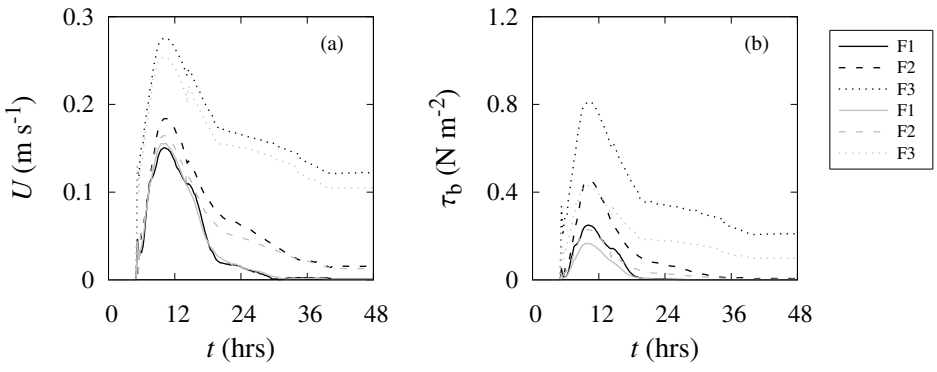

Figure 5.26: Comparison of flow velocities (a) and bed shear stresses (b) for a Q100 flood between Scenarios 1 (black) and 4 (grey) at each of the downstream floodplain monitoring points.

of the original woodland and had a relatively negligible impact on in-channel flow. The 7% reduction in peak bed shear stress at point C5 indicates that the expansion of the SRC may decrease the amount of bed erosion and sediment transport within the main channel, thus helping to minimize sediment deposition further downstream.

5.6.5 Scenario 5: Floodplain Storage

In the final scenario, the potential of floodplain storage to reduce the flood peak at Lopen Brook is investigated. This is achieved by restoring two floodplain bunds that were created by the Forestry Commission in 2005. Originally, the bunds ran perpendicular to the main channel near the downstream boundary and were approximately 0.5 m high (see Fig. 5.27). However, they have since subsided somewhat, which has been further exacerbated by the movement of livestock (cattle, horses, etc.) and are now barely visible.

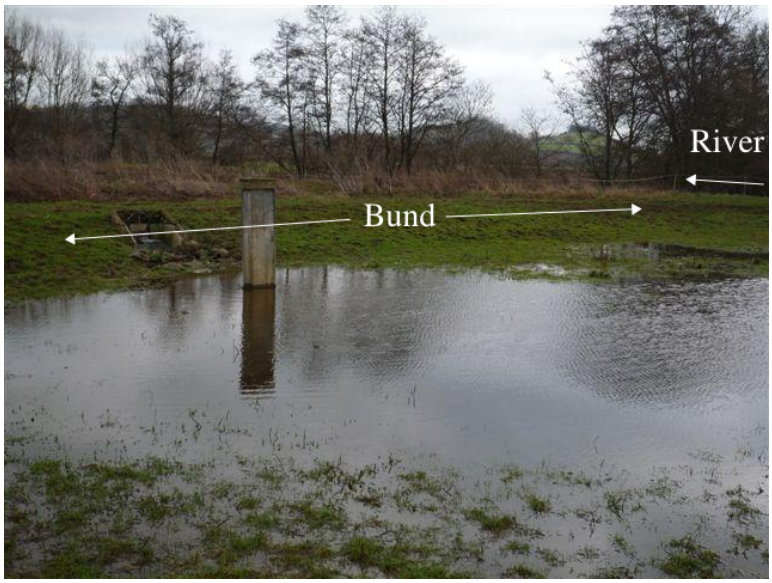

Figure 5.27: View of the previous floodplain bund at the downstream reach of Lopen Brook.

The bunds were introduced back into the DEM as close as possible to their original positions. Each bund is 0.5 m high by 1 m wide and extends for roughly

30 m on either side of the main channel until they reach the valley side slopes. The elevation and locations of the restored floodplain bunds are shown in Fig. 5.28.

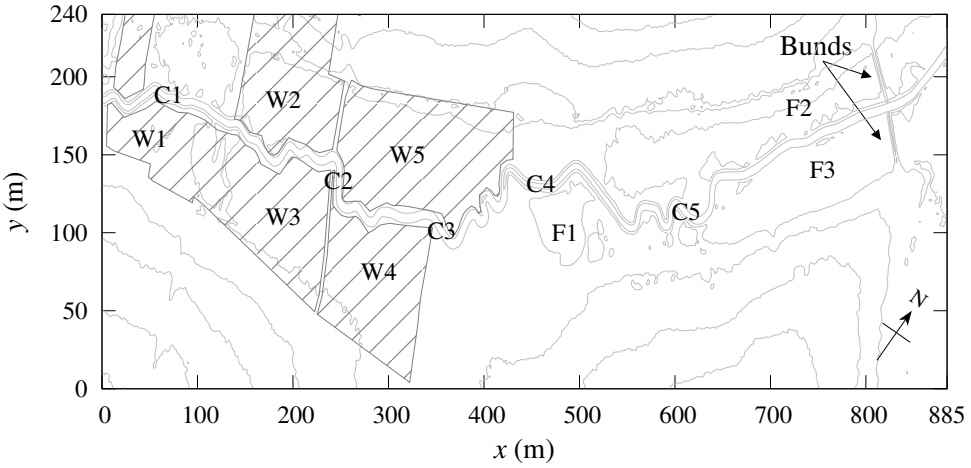

Figure 5.28: Location of the bunds on the downstream floodplain at Lopen Brook. Shaded areas indicate woodland extent. Model monitoring points are split into: in-channel (C); original woodland (W); and downstream floodplain (F) locations.

The SRC from the previous two scenarios is replaced with the existing woodland (Scenario 2) so that the impact of the bunds can be examined with respect to the current conditions at Lopen Brook. The model is run again using the same boundary conditions as the previous scenarios. For brevity, only the Q100 flood is discussed herein since the lower flood return periods follow a similar pattern.

The downstream flood hydrograph for the Q100 flood is presented in Fig. 5.29. The introduction of the bunds reduce and delay the downstream flood peak by 32.5% and 2 hrs, respectively, when compared to the upstream boundary and by 12.1% and 1 hr, respectively, when compared to the second scenario. The reduction and delay in peak flow is due to the increased storage capacity of the downstream floodplain where, in previous scenarios, water could flow freely towards the downstream boundary. It can also be seen that the tail of the hydrograph is slightly delayed, which is caused by the water on the downstream floodplain draining back into the main channel once the water level in the main channel begins to drop.

The increase in floodplain storage due to the bunds is clearly visible in

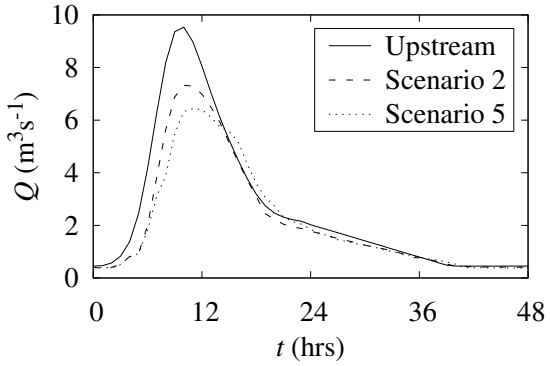

Figure 5.29: Downstream flood hydrographs during a Q100 flood for Scenarios 2 and 5.

Fig. 5.30, which compares the water surface elevations between Scenarios 2 and 5 for a cross-section located at $x = 700$ m. The data were taken at the time of maximum flow depths on the downstream floodplain ($t = 12$ hrs), just after the peak on the upstream flood hydrograph. The cross-section location is chosen to be representative of the downstream floodplain overall. It can be seen that the water level rises so that the left hand floodplain is no longer disconnected from the main channel at the highest flow rates.

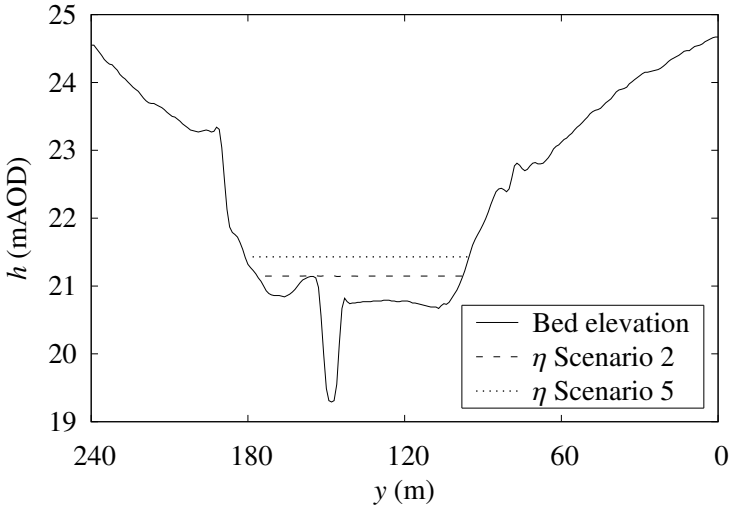

Figure 5.30: Cross-section of Lopen Brook at $x = 700$ m showing water surface elevation at $t = 12$ hrs during a Q100 flood for Scenarios 2 and 5.

The magnitudes of the bunds' effects are summarized in Table 5.11 for the in-channel and downstream floodplain locations. The woodland points (W) are omitted since the backwater effects of the bunds do not extend to these points and hence the differences in flow properties are very minor. The main change is the increase in flow depths, both on the downstream floodplain (as seen in Fig. 5.30) and also in the main channel, with the effects tailing off at around point C3. On the downstream floodplain, the average and maximum flow depths are raised by up to 60.7% and 102.6%, respectively.

As a result of the increased flow depths, the inundation area for the current scenario is 5.48% greater than for the second scenario. While the inundation area would typically be kept to a minimum during flood risk management, the current case study is confined to a rural valley, where the additional inundation area will cause relatively little damage as opposed to a more developed area. Therefore, it is assumed that the modest increase in inundation area in this scenario is acceptable given the reduction and delay to peak flow at the downstream boundary.

Table 5.11: Differences in average and maximum flow properties between Scenarios 2 and 5 for a Q100 flood. Monitoring point locations are split into in-channel (C) and downstream floodplain (F) areas.

Location	$\Delta\zeta_{\text{avrg}}$ (%)	$\Delta\zeta_{\text{max}}$ (%)	ΔU_{avrg} (%)	ΔU_{max} (%)	$\Delta\tau_{b_{\text{avrg}}}$ (%)	$\Delta\tau_{b_{\text{max}}}$ (%)
C1	0.75	0.06	−1.3	−0.23	−2.29	−0.44
C2	1.67	−0.07	−2.52	−0.45	−4.49	−0.78
C3	2.37	0.14	−7.61	−0.36	−16.11	−0.7
C4	3.95	7.68	−15.72	−7.73	−29.41	−15.11
C5	5.51	14.71	−40.26	−7.67	−55.78	0.04
F1	25.92	32.19	−18.34	−1.56	−20.6	−6.43
F2	60.69	102.61	−54.26	−6.22	−54.98	−26.61
F3	33.35	68.66	−13.29	−4.32	−34.54	−28.76

In conjunction with the raised water levels of the floodplain flows, the velocities and bed shear stresses are correspondingly lower than those in the second scenario. From Table 5.11, the average and maximum velocities are found to be decreased by up to 54.3% and 6.22%, respectively. The greater reduction in the average velocities compared to the maximum velocities is due to maximum velocities occurring during the initial wetting period when the presence of the

bunds have minimal impact. On the other hand, once the floodplains become inundated, the bunds restrict the flow and thus the average velocities are reduced.

Chapter 6

Conclusions and Future Research

6.1 Conclusions

The research contained within this thesis was motivated by the continuing effort to improve the understanding of the complex interactions that occur between flexible riparian vegetation and fluid flows. In particular, this thesis focused on providing simple, yet effective, tools for predicting the drag force of flexible vegetation under hydrodynamic loading. The main research outcomes from each chapter are highlighted in the following text.

6.1.1 Experimental Data and Analysis

In this chapter (§ 3), the two experimental data sets utilized in this thesis were introduced. The testing of foliated and defoliated trees in the first data set allowed the impact of foliage on the total drag force to be investigated (§ 3.3.1). This showed that the foliage is responsible for a large portion ($\approx 75\%$) of the total drag at low velocities ($U < 0.25\ \mathrm{m\,s^{-1}}$) before reducing to around 20%–50% and becoming relatively constant with velocity. Although discussed here for the first time with respect to full-scale trees, the findings are consistent with previous drag force studies involving flexible tree branches and smaller specimens (e.g. Wilson *et al.* 2008, Schoneboom and Aberle 2009, Västilä *et al.* 2013).

Investigation of the drag forces for both the full-scale tree and branch-scale data sets highlighted the non-quadratic force-velocity response of flexible veg-

etation (§ 3.3.2). Indeed, some of the force-velocity relationships were found to be almost linear, with the Vogel exponents for the specimens ranging from -0.46 to -1.05. Statistical analysis of the Vogel exponents suggested that they can be taken as species-specific. There was found to be no significant correlation between the Vogel exponent values and the trees' physical properties.

Analysis of photographs of the twenty-one full-scale trees from the first data set revealed that the distribution of the trees' projected area (and by association, their one-sided leaf area) over their height followed a sigmoid curve, rather than a linear relationship (§ 3.4.1), as has been assumed in previous studies (e.g. Järvelä 2004, Aberle and Järvelä 2013).

Video footage of the trees during drag force testing was also obtained during the experimental procedure and was analysed here using sophisticated image processing techniques to provide the variation in projected area with towing velocity for a number of the trees (§ 3.4.2). For the majority of trees studied here, the reduction in projected area was found to be roughly 50% at a towing velocity of 1 $\mathrm{m\,s^{-1}}$. However, the lack of key information, such as a reference scale or the focal length of the underwater camera, highlighted the need for careful consideration when designing similar experimental setups in the future.

6.1.2 Drag Force Models for Flexible Vegetation

Two drag force models for flexible riparian vegetation were proposed and tested in this chapter (§ 4). The first utilized the vegetation's projected areas in still air to define a 'rigid' drag coefficient (§ 4.2.1). An empirical relationship was then employed between the drag coefficient and an area Reynolds number. The model was shown to be accurate for the full-scale trees, from which the empirical model parameters were originally derived (§ 4.2.2). However, significant errors were observed when the model was applied to the natural and artificial branches from the independent experimental data set. This suggests that an empirical model such as this may not be suitable for general purpose modelling, at least not without proper prior calibration.

The second model was based on a dimensional analysis of the physical processes responsible for the deviation of the drag force away from a squared

relationship with velocity. A 'vegetative' Cauchy number, in conjunction with the Vogel exponent, was used to parameterize the vegetation's reconfiguration due to hydrodynamic loading (§ 4.3.1). The model was able to predict the drag forces of both the foliated and defoliated trees and the partially and fully submerged branches with good accuracy (§ 4.3.2), thus suggesting that the model is independent of both vegetation scale and relative level of submergence. The use of the projected area in still air was also confirmed to be a suitable reference area.

The Cauchy model was compared to two existing drag force modelling approaches: a semi-empirical model using the one-sided leaf area as the reference area (Järvelä 2004); and a previous version of the Cauchy reconfiguration approach (Whittaker *et al.* 2013). In all but one case, the Cauchy model developed in this thesis was found to be more accurate than the existing models (§ 4.3.3). However, it is acknowledged that the projected area in still air may be more difficult to measure in practice than the one-sided leaf area, which can be determined remotely.

A sensitivity analysis for the two Cauchy model parameters (a drag coefficient and Vogel exponent) was also performed (§ 4.3.4). A relatively large 'parameter space' was observed for which the model's drag force predictions have an average error of less than 30%. However, the model's predictions quickly become inaccurate for parameter values outside of this range. The analysis also showed that similar parameter values could be employed across species without significantly adversely affecting the model's predictions, contradicting the assumption that the drag coefficient and Vogel exponent are species-specific. It remains to be seen whether these parameters are more heavily influenced by vegetation's natural growth conditions or their species.

6.1.3 Numerical Modelling of Riparian Woodland

In this chapter (§ 5), an existing finite difference solution scheme for the shallow water equations (DIVAST-TVD) was optimized to take advantage of recent advances in heterogeneous computing (§ 5.4). Serial optimizations of the code resulted in a relative speed-up of over one-and-a-half times compared to the

original code. Parallel optimizations, using the OpenMP API, further increased this speed-up to over three-and-a-half times. The code was also ported to the C++ language so that the massively-parallel resources on modern graphics cards could be accessed. This resulted in a final speed-up of over six times compared to the original code, thus allowing large simulations to be run on a time-scale of days rather than weeks.

The Cauchy drag force model from the previous chapter (§ 4.3.1) was incorporated into the numerical solution scheme via a sink term in the momentum equations. A porosity term was also included in the continuity equation in order to account for the blockage effect of the vegetation (§ 5.3.3). This enabled the impact of riparian woodland on the flooding characteristics of a mid-catchment river to be investigated. The site chosen as the case study for the hydrodynamic modelling was a stretch of partially wooded floodplain adjacent to Lopen Brook in Somerset, UK (see § 5.5).

A number of scenarios were then modelled, with the flow depths, velocities and bed shear stresses monitored within the model. The floodplains were left clear of woodland in the first scenario so that the baseline flood characteristics could be established for the site (§ 5.6.1). A key conclusion from this scenario was that Reynolds number effects can safely be neglected when considering the bed friction for typical river and riparian floodplain flows.

In the second scenario (§ 5.6.2), the existing woodland at the site was introduced into the model. The woodland consisted of a mix of native deciduous species at a relatively sparse planting density. The modelling showed that the woodland had a negligible impact on the total flood inundation extents and downstream hydrographs; however, slight reductions in the flow velocities and bed shear stresses were observed within the forested areas.

The third and fourth scenarios investigated the impact of replacing the natural woodland with short rotation coppice (§ 5.6.3 and § 5.6.4). The results were similar to that of the previous scenario in that there was again no reduction in the downstream flood hydrographs. The reductions in flow velocity and bed shear stress within the forested areas were, however, more pronounced due to the increased planting density and blockage ratio of the short rotation coppice.

Finally, the last scenario combined the existing natural woodland with flood-

plain storage, created by two earthen bunds located towards the downstream boundary and running perpendicular to the main channel (§ 5.6.5). The model results showed that the bunds were the most effective way of reducing both the floodplain flow velocities and the downstream flood hydrographs at this particular site.

Although both the natural woodland and short rotation coppice had somewhat minimal impacts on the flooding characteristics of the site studied here, it is expected that the impact may be greater when considering reach-scale models. Furthermore, hydrological processes that act to reduce flood risk by reducing run-off, such as increased rates of infiltration and evapotranspiration, were not modelled in this study.

6.2 Future Research

During the course of this thesis, it was not possible to investigate all potential areas of interest, either due to data availability or time constraints. Therefore, a number of topics and items are recommended for future research.

Experimental Data Analysis

It would also be interesting to develop relationships between the leaf area index of the trees and their projected area in still air. Combined with recent advances in the remote sensing of leaf area index (Rautiainen *et al.* 2003, Zheng and Moskal 2009, Antonarakis *et al.* 2010, Forzieri *et al.* 2011), this would provide a useful tool for remotely estimating the projected area in still air for individual trees within forested regions.

Further experimental studies are also encouraged to expand the number of hydrodynamic drag force measurements for full-scale flexible vegetation. Currently, there are only a limited number of such data sets available for which both the vegetation's drag forces and physical properties have been recorded. Additional data sets may reveal that there is indeed a way of predicting the vegetation's Vogel exponents *a priori*.

Drag Force Models for Flexible Vegetation

Although the Cauchy reconfiguration model developed in this thesis was shown to be an improvement over existing drag force models for flexible riparian vegetation, it may be beneficial to combine the approaches. For instance, replacing the projected area in still air with the one-sided stem or leaf areas, which can be remotely sensed, might make the model easier to apply in practice. The wider adoption of the such drag force models could also be aided by expanding the number of species for which drag coefficients and Vogel exponents are available.

Numerical Modelling of Riparian Woodland

The optimization of an existing two-dimensional hydrodynamic numerical modelling software resulted in significant speed-ups. Even greater reductions in model run times could be achieved by optimizing the serial (i.e. non-graphics card) sections of the C++ code using the OpenMP parallel processing API. To create a modern modelling suite, the optimized software could easily be integrated with an open-source data visualization package, such as Paraview. A graphical user interface could also be generated using an open-source and platform-independent framework, such as Qt or GTK.

Considerable effort was made during the flood modelling of the Lopen Brook case study to ensure that the in-channel bathymetry and LiDAR data were correctly meshed together and that the resulting digital elevation model was well formed. However, while calibration data was available for the main channel, it was not possible to calibrate the bed roughness values chosen for the floodplain. Future modelling of the Lopen Brook site would benefit from detailed surveys enabling these values to be properly calibrated. Furthermore, it is hoped that velocity meters placed on the floodplain of Lopen Brook during the summer of 2013 will capture velocity data during a flood event so that the numerical model can be validated.

References

Aberle, J., Dittrich, A. (2012). An experimental study of drag forces acting on flexible plants. Proc. Int. Conf. *River Flow 2012*, San José, Costa Rica, R. Murillo Muñoz, ed. Taylor & Francis, London, UK, 193–200.

Aberle, J., Järvelä, J. (2013). Flow resistance of emergent rigid and flexible floodplain vegetation. *J. Hydraulic Res.* 51(1), 33–45.

Albayrak, I., Nikora, V., Miller, O., O'Hare, M. (2012). Flow-plant interactions at a leaf scale: Effects of leaf shape, serration, roughness and flexural rigidity. *Aquat. Sci.* 74(2), 267–286.

Alben, S., Shelley, M., Zhang, J. (2002). Drag reduction through self-similar bending of a flexible body. *Nature* 420(6915), 479–481.

Alongi, D. (2008). Mangrove forests: Resilience, protection from tsunamis, and responses to global climate change. *Estuar. Coast. Shelf Sci.* 76(1), 1–13.

Antonarakis, A., Richards, K., Brasington, J., Muller, E. (2010). Determining leaf area index and leafy tree roughness using terrestrial laser scanning. *Water Resour. Res.* 46(6), W06510.

Arcement, G., Schneider, V. (1989). Guide for selecting Manning's roughness coefficients for natural channels and flood plains. *Technical Report*, Water Supply Paper 2339, United States Geological Survey, Washington DC, USA.

Armanini, A., Righetti, M., Grisenti, P. (2005). Direct measurement of vegetation resistance in prototype scale. *J. Hydraulic Res.* 43(5), 481–487.

Barois, T., de Langre, E. (2013). Flexible body with drag independent of the flow velocity. *J. Fluid Mech.* 735(1), R2.

Beffa, C., Goring, D. (1995). Evaluation of depth-integrated turbulence models for unidirectional open-channel flow. Proc. Int. Conf. *12th Australasian Fluid Mechanics Conference*, University of Sydney, Australia. 183–186.

Blevins, R. (1990). *Flow induced vibrations*. 2nd ed. Van Nostrand Reinhold, New York, USA.

Boller, M., Carrington, E. (2006). The hydrodynamic effects of shape and size change during reconfiguration of flexible macroalga. *J. Exp. Biol.* 209(10), 1894–1903.

Breugem, W., Boersma, B., Uittenbogaard, R. (2006). The influence of wall permeability on turbulent channel flow. *J. Fluid Mech.* 562(1), 35–72.

Broadmeadow, S., Jones, J., Langford, T., Shaw, P., Nisbet, T. (2011). The influence of riparian shade on lowland stream water temperatures in southern England and their viability for brown trout. *River Res. Appl.* 27(2), 226–237.

Buchanan, T., Somers, W. (1976). Tecniques of water-resources investigations of the United States Geological Survey: Discharge measurements at gauging stations. *Technical Report*, United States Geological Survey, Washington D.C., USA.

Buckingham, E. (1914). On physically similar systems: Illustrations of the use of dimensional equations. *Phys. Rev.* 4(4), 345–376.

Bullard, M., Mustill, S., McMillan, S., Nixon, P., Carver, P., Britt, C. (2002). Yield improvements through modification of planting density and harvest frequency in short rotation coppice Salix spp. *Biomass Bioenerg.* 22(1), 15–25.

Cermak, J., Isyumov, N. (1998). *Wind tunnel studies of buildings and structures*. 2nd ed. ASCE, Reston, USA.

Chakrabarti, S. (2002). *The theory and practice of hydrodynamics and vibration*. 1st ed. World Scientific, Singapore.

Chen, L., Stone, M., Acharya, K., Steinhaus, K. (2011). Mechanical analysis for emergent vegetation in flowing fluids. *J. Hydraulic Res.* 49(6), 766–774.

Chow, V.T. (1973). *Open channel hydraulics*. Int'l ed. McGraw-Hill, New York, USA.

Clauset, A., Shaliz, C., Newman, M. (2009). Power-law distributions in empirical data. *SIAM Review* 51(4), 661–703.

Coates, R., Coutie, M., Kong, F. (1990). *Structural Analysis*. 3rd ed. Chapman & Hall, London, UK.

Cowan, W. (1956). Estimating hydraulic roughness coefficients. *Agric. Eng.* 37(7), 473–475.

CRT (2014). Is re-wilding our rivers a solution to flooding? *Technical Report*, The Countryside Restoration Trust, Cambridge, UK.

Cullen, S. (2005). Trees and wind: A practical consideration of the drag equation velocity exponent for urban tree risk management. *J. Arboric.* 31(3), 101–113.

Defina, A., Bixio, A. (2005). Mean flow and turbulence in vegetated open channel flow. *Water Resour. Res.* 41(7), W07006.

Defra (2004). Best practice guidelines: Growing short rotation coppice. *Technical Report*, Derpartment for Environment Food and Rural Affairs, London, UK.

Defra (2006). Flood and coastal defence appraisal guidance. *Technical Report*, Department for Environment, Food and Rural Affairs, London, UK.

Dittrich, A., Aberle, J., Schoneboom, T. (2012). Drag forces and flow resistance of flexible riparian vegetation. In *Environmental Fluid Mechanics: Memorial colloquium on environmental fluid mechanics in honour of Professor Gerhard H. Jirka*. W. Rodi, M. Uhlmann, eds. CRC Press, London, UK, 195–215.

Douglas, J., Gasiorek, J., Swaffield, J., Jack, L. (2005). *Fluid mechanics*. 5th ed. Pearson, Harlow, UK.

EA (2009). Flood and coastal risk management in England. *Technical Report*, Environment Agency, Bristol, UK.

Elder, J. (1959). The dispersion of marked fluid in turbulent shear flow. *J. Fluid Mech.* 5(4), 544–560.

Eldrandaly, K., Abu-Zaid, M. (2011). Comparison of six GIS-based spatial interpolation methods for estimating air temperature in western Saudi Arabia. *J. Environ. Inform.* 18(1), 38–45.

Elowson, S., Christersson, L. (1994). Purification of groundwater using biological filters. In *Willow vegetation filters for municipal wastewaters and sludges: A biological purification system*. P. Aronsson, K. Pertthu, eds. Swedish University of Agricultural Sciences, Uppsala, Sweden, 219–223.

Falconer, R., Chen, Y. (1991). An improved representation of flooding and drying and wind stress effects in a two-dimensional tidal numerical model. *Proc. Inst. Civil Eng. Pt. 2* 91(4), 659–678.

Fathi-Maghadam, M., Kouwen, N. (1997). Non-rigid, non-submerged, vegetative roughness on floodplains. *J. Hydraulic Eng.* 123(1), 51–57.

Fathi-Moghadam, M. (2007). Physical properties of tall vegetation for resistance to flow. *J. Agron.* 6(1), 194–198.

Ferguson, R. (2010). Time to abandon the Manning equation? *Earth Surf. Proc. Land.* 35(15), 1873–1876.

Finnigan, J., Shaw, R., Patton, E. (2009). Turbulence structure above a vegetation canopy. *J. Fluid Mech.* 637(1), 387–424.

Fischer, H., List, E., Koh, R., Imberger, J., Brooks, N. (1979). *Mixing in inland and coastal waters*. 1st ed. Academic Press, New York, USA.

Fischer-Antze, T., Stoesser, T., Bates, P., Olsen, N.R. (2001). 3D numerical modelling of open-channel flow with submerged vegetation. *J. Hydraulic Res.* 39(3), 303–310.

Folkard, A. (2011). Vegetated flows in their environmental context: A review. *Eng. Comput. Mech.* 164(1), 3–24.

Forti, D. (2012). Comparison of shape parametrization techniques for fluid-structure interaction problems. *Master's Thesis*, Facoltà di Ingeneria Industriale, Politecnio di Milano, Italy.

Forzieri, G., Degetto, M., Righetti, M., Castelli, F., Preti, F. (2011). Satellite multispectral data for improved floodplain roughness modelling. *J. Hydrol.* 407(1-4), 41–57.

Freeman, G., Rahmeyer, W., Copeland, R. (2000). Determination of resistance due to shrubs and woody vegetation. *Technical Report*, US Army Corps of Engineers, Washington DC, USA.

Fuller, R., Warren, M. (1993). *Coppiced woodlands: Their management for wildlife*. 2nd ed. Joint Nature Conservation Committee, Peterborough, UK.

Gaylord, B., Blanchette, C., Denny, M. (1994). Mechanical consequences of size in wave-swept algae. *Ecol. Monogr.* 64(3), 287–313.

Gosselin, F., de Langre, E. (2011). Drag reduction by reconfiguration of a poroelastic system. *J. Fluid. Struct.* 27(7), 1111–1123.

Gosselin, F., de Langre, E., Machado-Almeida, B. (2010). Drag reduction of flexible plates by reconfiguration. *J. Fluid Mech.* 650(1), 319–341.

Green, D., Winandy, J., Kretschmann, D. (1999). Mechanical properties of wood. *Technical Report*, Forest Products Laboratory Rep. FPL-GTR-113, U.S. Department of Agriculture, Madison, USA.

Hall, R., Allen, S., Rosier, P., Smith, D., Hodnett, M., Roberts, J., Hopkins, R., Davies, H., Kinniburgh, D., Gooddy, D. (1996). Hydrological effects of short rotation coppice. *Technical Report*, Institute of Hydrology, Wallingford, UK.

Harder, D., Speck, O., Hurd, C., Speck, T. (2004). Reconfiguration as a prerequisite for survival in highly unstable flow-dominated habitats. *J. Plant Growth Regul.* 23(2), 98–107.

Hirata, T. (1951). Fundamental studies on the formation of cutting series on the protection of a stand against storm damages. *Bull. of Tokyo University* 39(1), 1–11.

Huai, W., Wu, Z., Qian, Z., Geng, C. (2011). Large Eddy Simulation of open channel flows with non-submerged vegetation. *J. Hydrodyn. Ser. B* 23(2), 258–264.

Hughes, F. (2003). Guidance for policy makers and river managers in Europe on the restoration of floodplain forests. *Technical Report*, Department of Geography, University of Cambridge, UK.

Huthoff, F., Augustijn, D., Hulscher, S. (2007). Analytical solution of the depth-averaged flow velocity in case of submerged rigid cylindrical vegetation. *Water Resour. Res.* 43(6), W06413.

ICE (2001). Learning to live with rivers. In *Final report of the Institution of Civil Engineers' Presidential Commission to review the technical aspects of flood risk management in England and Wales*. G. Fleming, L. Frost, S. Huntington, D. Knight, F. Law, eds. Institution of Civil Engineers, London, UK.

ICE (2011). Flood risk management: A local issue of national importance. *Technical Report*, Institution of Civil Engineers, London, UK.

IPCC (2007). Contribution of Working Group II: Impacts, adaptation and vulnerability. In *Fourth Assessment Report of the Intergovernmental Panel on Climate Change*. M. Parry, O. Canziani, J. Palutikof, P. van der Linden, C. Hanson, eds. Cambridge University Press, Cambridge, UK.

IPCC (2012). Managing the risks of extreme events and disasters to advance climate change adaptation. In *Special Report of the Intergovernmental Panel on Climate Change*. C. Field, V. Barros, T. Stocker, D. Qin, eds. Cambridge University Press, Cambridge, UK.

Ishikawa, Y., , Mizuhara, K., Ashida, S. (2000). Effect of density of trees on drag exerted on trees in river channels. *J. Forest Res.* 5(4), 271–279.

Jalonen, J., Järvelä, J., Aberle, J. (2013). Leaf area index as vegetation density measure for hydraulic analyses. *J. Hydraulic Eng.* 139(5), 461–469.

James, C., Birkhead, A., Jordanova, A., O'Sullivan, J. (2004). Flow resistance of emergent vegetation. *J. Hydraulic Res.* 42(4), 390–398.

James, C., Goldbeck, U., Patini, A., Jordanova, A. (2008). Influence of foliage on flow resistance of emergent vegetation. *J. Hydraulic Res.* 46(4), 536–542.

Järvelä, J. (2002a). Determination of flow resistance of vegetated channel banks and floodplains. Proc. Int. Conf. *River Flow 2002*, Louvain-La-Neuve, D. Bousmar, Y. Zech, eds. Swets & Zeitlinger, Lisse, The Netherlands, 311–318.

Järvelä, J. (2002b). Flow resistance of flexible and stiff vegetation: A flume study with natural plants. *J. Hydrol.* 269(1), 44–54.

Järvelä, J. (2004). Determination of flow resistance caused by non-submerged woody vegetation. *Int. J. River Basin Manage.* 2(1), 61–70.

Järvelä, J. (2006). Vegetative flow resistance: Characterization of woody plants for modelling applications. Proc. Int. Conf. *World Water and Environmental Resources Congress*, Omaha, R. Graham, ed. ASCE, New York, USA, 1–10.

Katul, G., Mahrt, L., Poggi, D., Sanz, C. (2004). One- and two-equation models for canopy turbulence. *Bound.-Layer Meteor.* 113(1), 81–109.

Kim, S., Stoesser, T. (2011). Closure modeling and direct simulation of vegetation drag in flow through emergent vegetation. *Water Resour. Res.* 47(10), W10511.

King, A., Tinoco, R., Cowen, E. (2012). A k-ϵ turbulence model based on the scales of vertical shear and stem wakes valid for emergent and submerged vegetated flows. *J. Fluid Mech.* 701(1), 1–39.

King, S.D. (2004). Foresight: Future flooding. *Technical Report*, Office of Science and Technology, London, UK.

Kjeldsen, T., Stewart, E., Packman, J., Folwell, S., Bayliss, A. (2005). Revitalisation of the FEH rainfall runoff method (FD1913). *Technical Report*, Derpartment for Environment Food and Rural Affairs, London, UK.

Koizumi, A., Motoyama, J., Sawata, K., Sasaki, Y., Hirai, T. (2010). Evaluation of drag coefficients of poplar-tree crowns by a field test method. *J. Wood Sci.* 56(3), 189–193.

Kothyari, U., Hayashi, K., Hashimoto, H. (2009). Drag coefficient of unsubmerged rigid vegetation stems in open channel flows. *J. Hydraulic Res.* 47(6), 691–699.

Kouwen, N., Fathi-Moghadam, M. (2000). Friction factors for coniferous trees along rivers. *J. Hydraulic Eng.* 126(10), 732–740.

de Langre, E. (2008). Effects of wind on plants. *Annu. Rev. Fluid Mech.* 40(1), 141–168.

de Langre, E., Gutierrez, A., Cossé, J. (2012). On the scaling of drag reduction by reconfiguration in plants. *C. R. Mec.* 340(1-2), 35–40.

Li, C.W., Yan, K. (2007). Numerical investigation of wave–current–vegetation interaction. *J. Hydraulic Eng.* 133(7), 794–803.

Li, C.W., Zhang, M. (2010). 3D modelling of hydrodynamics and mixing in a vegetation field under waves. *Comput. Fluids* 39(4), 604–614.

Li, R.M., Shen, H. (1973). Effect of tall vegetations on flow and sediment. *J. Hydraul. Div.* 99(5), 793–814.

Liang, D., Falconer, R., Lin, B. (2006). Comparison between TVD-MacCormack and ADI-type solvers of the shallow water equations. *Adv. Water Resour.* 29(12), 1833–1845.

Liang, D., Lin, B., Falconer, R. (2007). Simulation of rapidly varying flow using an efficient TVD-MacCormack scheme. *Int. J. Numer. Meth. Fl.* 58(5), 811–826.

Lindner, K. (1982). Der Strömungswiderstand von Pflanzenbeständen. *PhD Thesis*, Leichtweiß-Institut für Wasserbau No.75, Technische Universität Braunschweig, Germany.

Liu, D., Diplas, P., Fairbanks, J., Hodges, C. (2008). An experimental study of flow through rigid vegetation. *J. Geophys. Res.* 113(4), F04015.

Lopez, F., Garcia, M. (2001). Mean flow and turbulence structure of open-channel flow through non-emergent vegetation. *J. Hydraulic Eng.* 127(5), 392–402.

Luhar, M., Nepf, H. (2011). Flow-induced reconfiguration of buoyant and flexible aquatic vegetation. *Limnol. Oceanogr.* 56(6), 2003–2017.

MAFF (2001). Flood and coastal defence project appraisal guidance: Overview. *Technical Report*, Ministry of Agriculture, Fisheries and Food, London, UK.

Mansfield, C., Pattanayak, S., McDow, W., McDonald, R., Halpin, P. (2005). Shades of green: Measuring the value of urban forests in the housing market. *J. Forest Econ.* 11(3), 177–199.

Marshall, M., Ballard, C., Frogbrook, Z., Solloway, I., McIntyre, N., Reynolds, B., Wheater, H. (2014). The impact of rural land management changes on soil hydraulic properties and runoff processes: Results from experimental plots in upland UK. *Hydrol. Processes* 28(4), 2617–2629.

Massey, B. (2006). *Mechanics of fluids*. 8th ed. Taylor & Francis, Abingdon, UK.

Mattis, S., Dawson, C., Kees, C., Farthing, M. (2012). Numerical modeling of drag for flow through vegetated domains and porous structures. *Adv. Water Resour.* 39(1), 44–59.

Mayhead, G. (1973). Some drag coefficients for British forest trees derived from wind tunnel studies. *Agric. Meteorol.* 12(1), 123–130.

McKay, H. (2011). Short rotation forestry: Review of growth and environmental impacts (Forest Research Monograph 2). *Technical Report*, Forest Research, Surrey, UK.

Medeiros, S., Hagen, S., Weishampel, J. (2012). Comparison of floodplain surface roughness parameters derived from land cover data and field measurements. *J. Hydrol.* 452(1), 139–149.

Nepf, H. (1999). Drag, turbulence, and diffusion in flow through emergent vegetation. *Water Resour. Res.* 35(2), 479–489.

Nikora, V. (2010). Hydrodynamics of aquatic ecosystems: An interface between ecology, biomechanics and environmental fluid mechanics. *River Res. Appl.* 26(4), 367–384.

Nisbet, T., Marrington, S., Thomas, H., Broadmeadow, S., Valatin, G. (2011). Slowing the flow at Pickering. *Technical Report*, Forest Research, Surrey, UK.

Nvidia (2013). CUDA C programming guide. *Technical Report*, Nvidia, California, USA.

O'Hare, M., Hutchinson, K., Clarke, R. (2007). The drag and reconfiguration experienced by five macrophytes from a lowland river. *Aquat. Bot.* 86(3), 253–259.

Oplatka, M. (1998). Stabilität von Weidenverbauungen an Flussufern. *PhD Thesis*, Eidgenössische Technische Hochschule Zürich, Switzerland.

Papesch, A. (1977). A field study to determine the drag coefficient and the associated centre of pressure of a forest front. Proc. Int. Conf. *6th Australasian Hydraulics and Fluid Mechanics Conference*, Adelaide. Institution of Engineers, Australia, 451–454.

Petryk, S., Bosmajian, G. (1975). Analysis of flow through vegetation. *J. Hydraul. Div.* 101(7), 871–884.

Pitt, S.M. (2008). Learning lessons from the 2007 floods. *Technical Report*, Cabinet Office, London, UK.

Rastogi, A., Rodi, W. (1978). Predictions of heat and mass transfer in open channels. *J. Hydraul. Div.* 104(3), 397–420.

Rautiainen, M., Stenberg, P., Nilson, T., Kuusk, A., Smolander, H. (2003). Application of a forest reflectance model in estimating leaf area index of Scots pine stands using Landsat-7 ETM reflectance data. *Can. J. Remote Sens.* 29(3), 314–323.

Reynard, N., Crooks, S., Wilby, R., Kay, A. (2004). Climate change and flood frequency in the UK. Proc. Int. Conf. *39th Defra Flood and Coastal Flood Management Conference*, 11, York. Defra, London, UK, 1–12.

Rodi, W. (1993). *Turbulence models and their application in hydraulics*. 1st ed. Taylor & Francis, Abingdon, UK.

Sand-Jensen, K. (2003). Drag and reconfiguration of freshwater macrophytes. *Freshwater Biol.* 48(2), 271–283.

Sand-Jensen, K. (2008). Drag forces on common plant species in temperate streams: Consequences of morphology, velocity and biomass. *Hydrobiologia* 601(1), 307–319.

Sand-Jensen, K., Pedersen, M. (2008). Streamlining of plant patches in streams. *Freshwater Biol.* 53(4), 714–726.

Schoneboom, T. (2011). Widerstand flexibler Vegetation und Sohlenwiderstand in durchströmten Bewuchsfeldern. *PhD Thesis*, Leichtweiß-Institut für Wasserbau No.157, Technische Universität Braunschweig, Germany.

Schoneboom, T., Aberle, Wilson, C., Dittrich, A. (2008). Drag force measurements of vegetation elements. Proc. Int. Conf. *8th International Conference on Hydro-Science and Engineering*, Nagoya, Japan.

Schoneboom, T., Aberle, J. (2009). Influence of foliage on drag force of flexible vegetation. Proc. Int. Conf. *33rd IAHR World Congress*, 1, Vancouver. Taylor & Francis, London, UK, 6585–6592.

Schoneboom, T., Aberle, J., Dittrich, A. (2010). Hydraulic resistance of vegetated flows: Contribution of bed shear stress and vegetative drag to total hydraulic resistance. Proc. Int. Conf. *River Flow 2010*, Braunschweig, A. Dittrich, K. Koll, J. Aberle, P. Geisenhainer, eds. Bundesanstalt für Wasserbau, Karlsruhe, Germany, 269–276.

SEPA (2009). Engineering in the water environment: Riparian vegetation management. *Technical Report*, Scottish Environment Protection Agency, Stirling, UK.

Shames, I. (2003). *Mechanics of fluids*. 4th ed. McGraw-Hill, New York, USA.

Siniscalchi, F., Nikora, V. (2013). Dynamic reconfiguration of aquatic plants and its interrelations with upstream turbulence and drag forces. *J. Hydraulic Res.* 51(1), 46–55.

Spalart, P., Allmaras, S. (1994). A one-equation turbulence model for aerodynamic flows. *Recherche Aerospatiale* 1(1), 5–21.

Starr, C. (2013). *Woodland management: A practical guide*. 2nd ed. The Crowood Press, Marlborough, UK.

Stoesser, T. (2002). Development and validation of a CFD code for open-channel flows. *PhD Thesis*, Department of Civil Engineering, University of Bristol, UK.

Stoesser, T., Kim, S., Diplas, P. (2010). Turbulent flow through idealized emergent vegetation. *J. Hydraulic Eng.* 136(12), 1003–1017.

Stoesser, T., Salvador, G., Rodi, W., Diplas, P. (2009). Large Eddy Simulation of turbulent flow through submerged vegetation. *Transport Porous Med.* 78(3), 347–365.

Stoesser, T., Wilson, C., Bates, P., Dittrich, A. (2003). Application of a 3D numerical model to a river with vegetated floodplains. *J. Hydroinf.* 5(2), 99–112.

Stone, B., Shen, H. (2002). Hydraulic resistance of flow in channels with cylindrical roughness. *J. Hydraulic Eng.* 128(5), 500–506.

Stone, M., Chen, L., McKay, S., Goreham, J., Acharya, K., Fischenich, C., Stone, A. (2011). Bending of submerged woody riparian vegetation as a function of hydraulic flow conditions. *River Res. Appl.* 29(2), 195–205.

Sutter, H. (2005). The concurrency revolution. *C/C++ User. J.* 23(2), 21–36.

Tabacchi, E., Planty-Tabacchi, A.M., Salinas, J., Décamps, H. (1996). Landscape structure and diversity in riparian plant communities: A longitudinal comparative study. *Regul. Rivers Res. Manage.* 12(4), 367–390.

Tang, H., Tian, Z., Yan, J., Liang, D., Xiao, Y. (2012). Bulk and local drag coefficients of the submerged rigid vegetation. *J. Hydraulic Res.* In press, 1–26.

Tanino, Y., Nepf, H. (2008). Laboratory investigation of mean drag in a random array of rigid emergent cylinders. *J. Hydraulic Eng.* 134(1), 34–41.

Teo, F. (2011). Study of the hydrodynamic processes of rivers and floodplains with obstructions. *PhD Thesis*, Hydro-environmental Research Centre, Cardiff University, UK.

Thorne, C., Henshaw, A., Bates, P., Brown, D., Coulthard, T., Gurnell, A., Lewin, J., Longfield, S., Maas, G., Macklin, M., Nicholas, A., Parker, C., Rees, J., Sear, D., Surendan, S., Walker, J., Warburton, J. (2010). Applied fluvial geomorphology for sustainable flood risk management. Proc. Int. Conf. *45th Defra Flood and Coastal Flood Management Conference*, 1, Telford. Defra, London, UK, 1–10.

Tubby, I., Armstrong, A. (2002). Establishment and management of short rotation coppice. *Technical Report*, Forest Research, Edinburgh, UK.

UKCIP (2009). The climate of the UK and recent trends. *Technical Report*, UK Climate Impacts Programme, Exeter, UK.

UN (2006). Report on the sixth session. Proc. Int. Conf. *United Nations Forum on Forests*, 1, New York. United Nations, New York, USA, 1–48.

UNEP (2000). European forests and protected areas: Gap analysis. *Technical Report*, World Conservation Monitoring Centre, Cambridge, UK.

UNU-EHS (2004). Two billion vulnerable to floods by 2050; number expected to double or more in two generations. *Technical Report*, Institute for Environment and Human Security, United Nations University.

Västilä, K., Järvelä, J. (2014). Modeling the flow resistance of woody vegetation using physically based properties of the foliage and stem. *Water Resour. Res.* 50(1), 229–245.

Västilä, K., Järvelä, J., Aberle, J. (2013). Characteristic reference areas for estimating flow resistance of natural foliated vegetation. *J. Hydrol.* 492(1), 49–60.

Västilä, K., Järvelä, J., Aberle, J., Schoneboom, T. (2011). Vegetative drag in natural, foliated plant stands. Proc. Int. Conf. *34th IAHR World Congress*, 5, Brisbane. Taylor & Francis, London, UK, 2978–2985.

Vischer, D., Oplatka, M. (1998). Der Strömungswiderstand eines flexiblen Ufer- und Vorlandbewuchses. *Wasserwirtschaft* 88(6), 284–288.

Vogel, S. (1984). Drag and flexibility in sessile organisms. *Am. Zool.* 24(1), 37–44.

Vogel, S. (1989). Drag and reconfiguration of broad leaves in high winds. *J. Exp. Bot.* 40(8), 941–948.

Vollsinger, S., Mitchell, S., Byrne, K., Novak, M., Rudnicki, M. (2005). Wind tunnel measurements of crown streamlining and drag relationships for several hardwood species. *Can. J. Forest Res.* 35(5), 1238–1249.

Wang, P., Wang, C. (2011). Numerical model for flow through submerged vegetation regions in a shallow lake. *J. Hydrodyn. Ser. B* 23(2), 170–178.

Weare, T. (1976). Finite element or finite difference methods for the two-dimensional shallow water equations? *Comput. Methods Appl. Mech. Engin.* 7(3), 351–357.

Weissteiner, C. (2009). Biomechanical behaviour of plants under hydraulic load. *Technical Report*, University of Natural Resources and Applied Life Sciences, Vienna, Austria.

Weiyan, T. (1992). *Shallow water hydrodynamics: Mathematical theory and numerical solution for a two-dimensional system of shallow water equations*. 1st ed. Elsevier, Amsterdam, The Netherlands.

Wendt, J. (2009). *Computational Fluid Dynamics: An introduction*. 3rd ed. Springer-Verlag, Berlin, Germany.

Wetherald, R., Manabe, S. (2002). Simulation of hydrologic changes associated with global warming. *J. Geophys. Res.* 107(1), 4379–4394.

Whittaker, P., Wilson, C., Aberle, J., Rauch, H.P., Xavier, P. (2013). A drag force model to incorporate the reconfiguration of full-scale riparian trees under hydrodynamic loading. *J. Hydraulic Res.* 51(5), 569–580.

Wilson, C., Hoyt, J., Schnauder, I. (2008). Impact of foliage on the drag force of vegetation in aquatic flows. *J. Hydraulic Eng.* 134(7), 885–891.

Wilson, C., Yagci, O., Rauch, H.P., Olsen, N. (2006a). 3D numerical modelling of a willow vegetated river floodplain system. *J. Hydrol.* 327(2), 13–21.

Wilson, C., Yagci, O., Rauch, H.P., Stoesser, T. (2006b). Application of the drag force approach to model the flow-interaction of natural vegetation. *Int. J. River Basin Manage.* 4(2), 137–146.

Wu, F., Shen, H., Chou, Y. (1999). Variation of roughness coefficients for unsubmerged and submerged vegetation. *J. Hydraulic Eng.* 125(9), 934–942.

Wu, W., Wang, P., Chiba, N. (2004). Comparison of five depth-averaged 2D turbulence models for river flows. *Arch. Hydroengin. Environ. Mech.* 51(2), 183–200.

Wu, Y., Falconer, R., Struve, J. (2001). Mathematical modeling of tidal currents in mangrove fields. *Environ. Modell. Softw.* 19(1), 19–29.

Wunder, S., Lehmann, B., Nestmann, F. (2009). Measuring drag force of flexible vegetation directly: Development of an experimental methodology. Proc. Int. Conf. *33rd IAHR World Congress*, 1, Vancouver. Taylor & Francis, London, UK, 1483–1489.

Wunder, S., Lehmann, B., Nestmann, F. (2011). Determination of the drag coefficients of emergent and just submerged willows. *Int. J. River Basin Manage.* 9(9), 231–236.

Xavier, P. (2009). Floodplain woodland hydrodynamics. *PhD Thesis*, Hydro-environmental Research Centre, Cardiff University, UK.

Xavier, P., Wilson, C., Aberle, J., Rauch, H.P., Schoneboom, T., Lammeranner, W., Thomas, H. (2010). Drag force of flexible submerged trees. Proc. Int. Conf. *Hydralab III Joint User Meeting*, Hannover.

Yen, B. (2002). Open channel flow resistance. *J. Hydraulic Eng.* 128(1), 20–39.

Zheng, G., Moskal, M. (2009). Retrieving leaf area index (LAI) using remote sensing: Theories, methods and sensors. *Sensors* 9(4), 2719–2745.

Zhou, J., Adrian, R., Balachandar, S., Kendall, T. (1999). Mechanisms for generating coherent packets of hairpin vortices in channel flow. *J. Fluid Mech.* 387(1), 353–396.

Appendix A

Vegetation Data

Table A.1: Wood mass and density as measured for the *A. glutinosa* (A), *P. nigra* (P) and *S. alba* (S) Hydralab trees. A dash (-) indicates data not recorded. The suffix 'B' denotes a branch cut from the tree with the same prefix.

Specimen	Wet mass $M_{S,w}$ (g)	Dry mass $M_{S,d}$ (g)	Volume V_S (cm^3)	Wet density $\rho_{S,w}$ ($kg\,m^{-3}$)	Dry density $\rho_{S,d}$ ($kg\,m^{-3}$)
A1	2,110	-	1,394	1,514	-
A2	2,772	1,289	2,866	967	450
A3	-	-	-	-	-
A4	1,168	529	1,194	978	443
A5	1,228	-	1,331	923	-
Average	1,820	909	1,696	1,095	446
P1	1,210	560	1,218	993	460
P2	2,082	933	-	-	-
P2B1	1,364	611	-	-	-
P2B2	718	317	417	1,722	760
P3	840	378	945	889	400
P4	2,416	1,009	2,344	1,031	430
P4B1	2,076	867	1,964	1,057	441
P4B2	340	142	380	895	374
Average	1,381	602	1,211	1,098	478
S1	2,892	378	2,271	1,273	166
S2	1,450	-	1,561	929	-
S3	5,450	-	5,250	1,038	-
S4	714	-	-	-	-
S5	2,416	973	3,051	792	319
S5B1	1,286	583	1,594	807	366
S5B2	1,130	512	1,457	776	351
S6	1,538	655	1,788	860	366
S6B1	920	392	1,039	885	377
S6B2	618	263	749	825	351
S7	2,070	856	2,359	877	363
S7B1	554	244	604	917	404
S7B2	796	351	907	878	387
S7B3	720	262	848	849	309
S8	744	316	765	973	413
S9	1,524	770	1,540	990	500
S10	2,486	1,115	2,388	1,041	467
S11	706	353	1,039	679	340
S12	954	529	1,346	709	393
Average	1,525	535	1,698	894	367

Table A.2: Leaf mass and density as measured for the *A. glutinosa* (A), *P. nigra* (P) and *S. alba* (S) Hydralab trees. A dash (-) indicates data not recorded. The suffix 'B' denotes a branch cut from the tree with the same prefix.

Specimen	Wet mass $M_{L,w}$ (g)	Dry mass $M_{L,d}$ (g)	Volume V_L (cm^3)	Wet density $\rho_{L,w}$ ($kg\,m^{-3}$)	Dry density $\rho_{L,d}$ ($kg\,m^{-3}$)
A1	148	32	222	667	144
A2	220	48	290	759	166
A3	120	28	-	-	-
A4	144	30	200	720	150
A5	102	22	130	785	169
Average	147	32	211	732	157
P1	-	-	-	-	-
P2	182	36	240	758	150
P2B1	122	24	150	813	161
P2B2	60	12	90	667	132
P3	78	16	100	780	160
P4	218	67	-	-	-
P4B1	78	24	100	780	240
P4B2	140	43	-	-	-
Average	125	32	136	760	169
S1	190	44	99	1,919	444
S2	72	18	120	600	150
S3	324	66	490	661	135
S4	132	32	-	-	-
S5	612	-	720	850	-
S5B1	298	74	350	851	211
S5B2	314	-	370	849	-
S6	558	140	840	664	167
S6B1	296	74	490	604	151
S6B2	262	66	350	749	187
S7	179	40	315	568	127
S7B1	60	-	115	522	-
S7B2	72	-	130	554	-
S7B3	47	-	70	671	-
S8	230	84	-	-	-
S9	466	-	510	914	-
S10	352	84	470	749	179
S11	116	52	170	682	306
S12	84	50	120	700	417
Average	245	63	337	771	225

Table A.3: Total combined wood and leaf mass as measured for the *A. glutinosa* (A), *P. nigra* (P) and *S. alba* (S) Hydralab trees. A dash (-) indicates data not recorded. The suffix 'B' denotes a branch cut from the tree with the same prefix.

Specimen	Wet mass M_w (g)	Dry mass M_d (g)	Volume V (cm^3)	Wet density ρ_w ($kg\,m^{-3}$)	Dry density ρ_d ($kg\,m^{-3}$)
A1	2,258	-	1,616	1,397	-
A2	2,992	1,337	3,156	948	424
A3	-	-	-	-	-
A4	1,312	559	1,394	941	401
A5	1,330	-	1,461	910	-
Average	1,973	948	1,907	1,049	412
P1	-	-	-	-	-
P2	2,264	969	-	-	-
P2B1	1,486	635	-	-	-
P2B2	778	329	507	1,535	649
P3	918	394	1,045	878	377
P4	2,634	1,076	-	-	-
P4B1	2,154	891	2,064	1,044	432
P4B2	480	185	-	-	-
Average	1,531	640	1,205	1,152	486
S1	3,082	422	2,370	1,300	178
S2	1,522	-	1,681	905	-
S3	5,774	-	5,740	1,006	-
S4	846	-	-	-	-
S5	3,028	-	3,771	803	-
S5B1	1,584	657	1,944	815	338
S5B2	1,444	-	1,827	790	-
S6	2,096	795	2,628	798	303
S6B1	1,216	466	1,529	795	305
S6B2	880	329	1,099	801	299
S7	2,249	896	2,674	841	335
S7B1	614	-	719	854	-
S7B2	868	-	1,037	837	-
S7B3	767	-	918	836	-
S8	974	400	-	-	-
S9	1,990	-	2,050	971	-
S10	2,838	1,199	2,858	993	420
S11	822	405	1,209	680	335
S12	1,038	579	1,466	708	395
Average	1,770	615	2,089	867	323

Appendix B

Lopen Brook

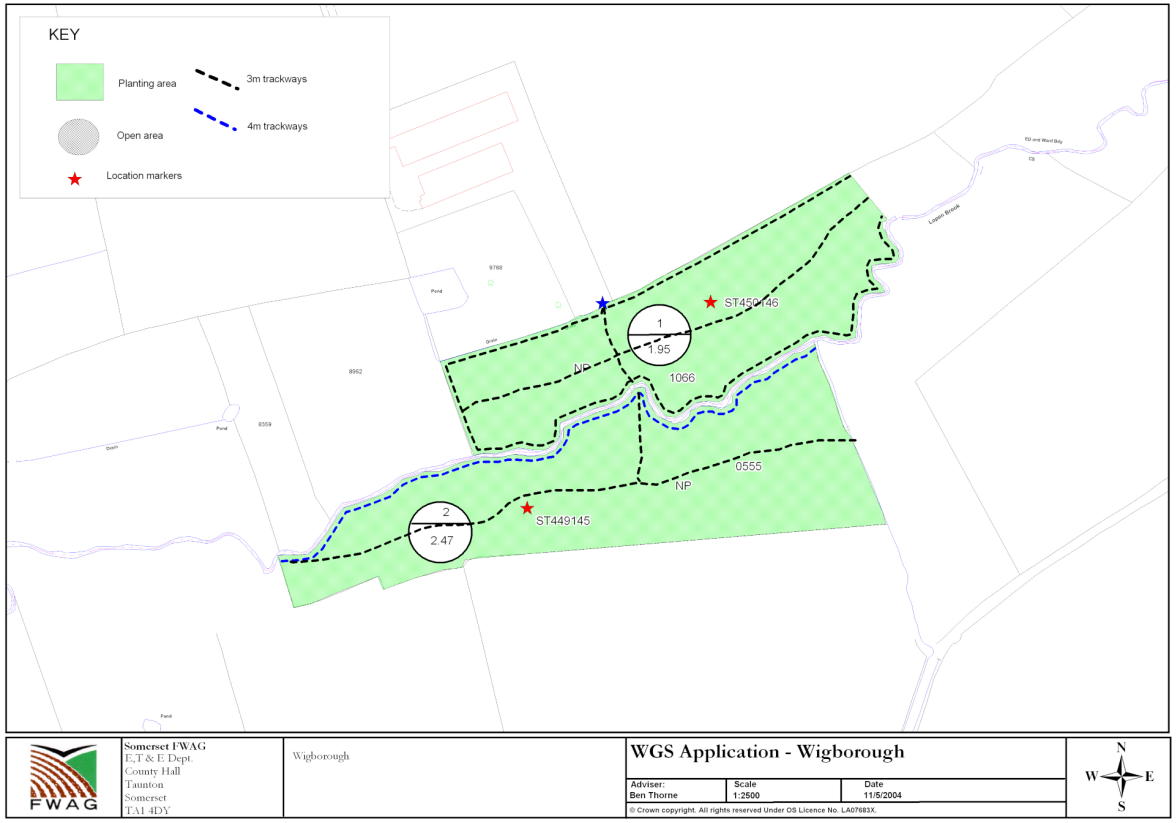

Figure B.1: Planning document for the planting of restoration woodland at Lopen Brook, Wigborough.

Table B.1: Stage-discharge data for Lopen Brook, collected at the upstream boundary (A) during August 2013.

Dist. from LB (m)	Depth (m)	Velocity ($m\,s^{-1}$)	Flow rate ($m^3\,s^{-1}$)
0	0	0	0
0.2	0.21	0.461	0.029
0.6	0.21	0.295	0.019
0.8	0.31	0.221	0.014
1	0.32	0.275	0.018
1.2	0.34	0.238	0.016
1.4	0.29	0.138	0.008
1.6	0.36	0.063	0.007
2	0.2	0	0
2.4	0.1	0	0
2.6	0	0	0
		Total	0.11

Table B.2: Stage-discharge data for Lopen Brook, collected at the upstream water level meter (B) during August 2013.

Dist. from LB (m)	Depth (m)	Velocity ($m\,s^{-1}$)	Flow rate ($m^3\,s^{-1}$)
0	0	0	0
0.2	0.12	0.221	0.005
0.4	0.18	0.115	0.004
0.6	0.22	0.038	0.002
0.8	0.26	0.408	0.021
1	0.25	0.648	0.032
1.2	0.25	0.795	0.04
1.4	0.2	0.408	0.016
1.6	0.15	0.141	0.003
1.7	0.09	0	0
		Total	0.124

Table B.3: Stage-discharge data for Lopen Brook, collected immediately upstream of the footbridge (C) during August 2013.

Dist. from LB (m)	Depth (m)	Velocity ($m\,s^{-1}$)	Flow rate ($m^3\,s^{-1}$)
0	0	0	0
0.3	0.16	0.641	0.026
0.5	0.2	0.761	0.03
0.7	0.24	0.468	0.022
0.9	0.3	0.468	0.028
1.1	0.27	0.167	0.009
1.3	0.15	0.063	0.003
1.8	0	0	0
		Total	0.119

Table B.4: Stage-discharge data for Lopen Brook, collected at the downstream water level meter (D) during August 2013.

Dist. from LB (m)	Depth (m)	Velocity ($m\,s^{-1}$)	Flow rate ($m^3\,s^{-1}$)
0	0	0	0
0.2	0.12	0.195	0.005
0.4	0.19	0.401	0.015
0.6	0.26	0.555	0.029
0.8	0.24	0.581	0.028
1	0.19	0.621	0.024
1.2	0.15	0.448	0.013
1.4	0.1	0.448	0.016
1.9	0	0	0
		Total	0.129

Table B.5: Stage-discharge data for Lopen Brook, collected at the downstream boundary (E) during August 2013.

Dist. from LB (m)	Depth (m)	Velocity ($m\,s^{-1}$)	Flow rate ($m^3\,s^{-1}$)
0	0	0	0
0.2	0.16	0.275	0.009
0.4	0.25	0.261	0.013
0.6	0.26	0.235	0.012
0.8	0.23	0.275	0.013
1	0.24	0.341	0.016
1.2	0.25	0.368	0.018
1.4	0.18	0.555	0.020
1.6	0.11	0.528	0.015
1.9	0	0	0
		Total	0.116